



Title	CP Asymmetry in the Decay $KL \rightarrow \pi + \pi^- e^+ e^-$
Author(s)	Senyo, Katsumi
Citation	大阪大学, 1999, 博士論文
Version Type	VoR
URL	https://doi.org/10.11501/3169041
rights	
Note	

The University of Osaka Institutional Knowledge Archive : OUKA

<https://ir.library.osaka-u.ac.jp/>

The University of Osaka

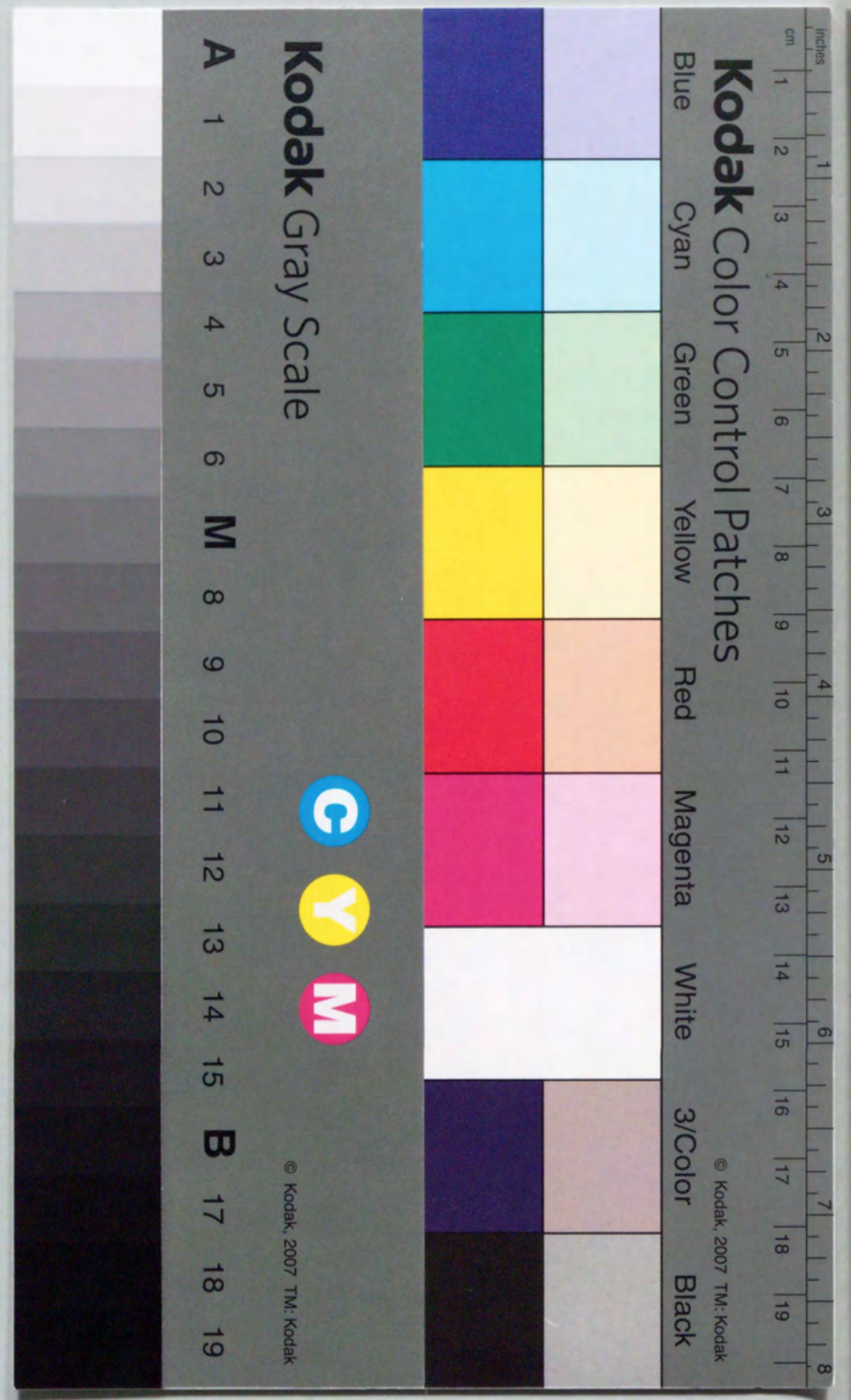
Acknowledgments

CP Asymmetry in the Decay $K_L \rightarrow \pi^+ \pi^- e^+ e^-$

DISSERTATION SUBMITTED TO
THE GRADUATE SCHOOL OF OSAKA UNIVERSITY
IN CANDIDACY FOR THE DEGREE OF
DOCTOR OF SCIENCE

By
Katsumi Senyo

1999



Acknowledgments

CP Asymmetry in the Decay $K_L \rightarrow \pi^+ \pi^- e^+ e^-$

DISSERTATION SUBMITTED TO
THE GRADUATE SCHOOL OF OSAKA UNIVERSITY
IN CANDIDACY FOR THE DEGREE OF
DOCTOR OF SCIENCE

By
Katsumi Senyo

1999

Acknowledgments

I first appreciate Prof. Yorikiyo Nagashima, for all research opportunity in HEP field. I was really enlightened by his expertise. T. Yamanaka gave me a chance to work on indirect CP violation in a *rare* K decay experiment, instead of a *B* physics experiment. I thank him for his supervision of my study, and really enjoy a chat with him about experimental and theoretical science. Also, I remember the trans-pacific midnight proofreading of the thesis, especially in the last one week before the defense.

Other stuffs in Osaka University, J. Haba, M. Takita, M. Hazumi and I. Suzuki gave me very useful advises and suggestions, in and out of physics. Their humor and wit always relaxed me. Thankfully, S. Tsuzuki supported my study from Osaka.

My works done at Fermilab, especially the physics analysis, were mostly supported by V. O'Dell. The discussion with her was really fun. I enjoyed the life on the crossover with L. Bellantoni, P. Shanahan, M. Pang, and R. B. David. I thank their kindness. I also appreciate KTeV people on the thirteen floor and new muon lab. Of course, I thank all of people working at the KTeV experiment. Without their efforts, I could not successfully finish my thesis like this.

I feel relaxed with T. Nakaya and K. Hanagaki, and previous generation of graduate students in Osaka University. Their friendship and useful suggestion encouraged me in any phases of my analysis. I studied much from them. I thank graduate students in Osaka University for their cooperation for years.

My parents, Sakae and Kotaro Senyo, patiently waited for my graduation. Their supports greatly heartened me. I hope they proud of me.

Finally, I thank my wife, Sachiko, and her tenderness. Actually, I enjoyed the life with her in Chicago. It was very tough time in my life, but we will long for our precious time and good friends in Fermilab.

Contents

1 Introduction	1
1.1 C, P, and CP Violation	1
1.2 CP violation in Neutral Kaon System	2
1.2.1 Indirect CP Violation	4
1.2.2 Direct CP Violation	4
1.2.3 Experimental Results of Indirect CP Violation	5
1.3 $K_L \rightarrow \pi^+ \pi^- e^+ e^-$ Decay	8
1.3.1 Decay Processes	8
1.3.2 Indirect CP violation	9
1.3.3 Direct CP violation	11
1.3.4 $gM1$ Form Factor	11
1.3.5 Experimental Status of $K_L \rightarrow \pi^+ \pi^- e^+ e^-$	12
1.4 Summary	12
1.4.1 Purpose of This Study	12
1.4.2 Overview of This Thesis	13
2 Experiment	14
2.1 K_L Beam Production	15
2.1.1 Beam Production	15
2.1.2 Sweeper and Collimeter	15
2.1.3 Vacuum System	17
2.2 Detector	17
2.2.1 Charged Spectrometer	17
2.2.2 Trigger hodoscopes	21
2.2.3 Electromagnetic Calorimeter	22
2.2.4 Photon Vetoes	24
2.2.5 Hadron/Muon vetoes	26
2.3 Trigger	29
2.3.1 Level 1 Trigger	29
2.3.2 Level 2 Trigger	31

2.3.3 Trigger Rate	32
2.3.4 Calibration Trigger	32
2.4 Data Acquisition System	32
2.4.1 Frontend and DAQ	33
2.4.2 Level 3 filtering	33
2.5 Physics Run	34
3 Monte Carlo Simulation	35
3.1 Kaon production	35
3.2 The Decays	36
3.2.1 $K_L \rightarrow \pi^+ \pi^- e^+ e^-$	37
3.2.2 $K_L \rightarrow \pi^+ \pi^- \pi^0$	37
3.2.3 Particle Tracing	38
3.3 Detector	38
3.3.1 Photon Veto	38
3.3.2 Drift Chamber	38
3.3.3 CsI calorimeter	39
3.4 Accidentals	42
3.4.1 Accidental Effect	42
3.4.2 Accidental Overlay	42
4 Event Reconstruction	43
4.1 Track Candidate Finding	43
4.1.1 Hit Pairing	43
4.1.2 Finding Y track candidates	44
4.1.3 Finding X track candidates	44
4.2 Cluster Finding	45
4.3 Track-Cluster Matching and Vertex Finding	45
4.4 Particle Identification	46
5 Event Selection	48
5.1 Background	48
5.2 Basic Constraints	50
5.2.1 Fiducial Volume Cut	50
5.2.2 Trigger Verification	51
5.2.3 Consistency Check	51
5.3 Event Selection	52
5.3.1 M_K Invariant Mass Cut	53
5.3.2 Total Momentum Cut	53
5.3.3 Vertex χ^2 Cut	53

5.3.4	M_{ee} Cut	53
5.3.5	p_t^2 Cut	56
5.3.6	Pp0kine Cut	57
5.3.7	Optimization of p_t^2 and Pp0kine Cuts	58
5.4	Acceptance and Data After Final Cuts	60
5.5	Background Estimation	62
5.5.1	Background Level from Each Source	62
5.5.2	Background estimation with sideband fit	63
5.5.3	Summary of Background Level	63
5.6	K_L Flux Calculation	63
5.6.1	Acceptance and Flux Calculation	64
5.6.2	Systematic Uncertainty	66
5.6.3	Summary	68
6	Form Factor Measurement	70
6.1	Formulation	70
6.2	Maximum Likelihood Fit	73
6.3	Data and Monte Carlo Comparison	74
6.4	Error on the Form Factor	74
6.4.1	Fitting Procedure	77
6.4.2	Smearing by Detector Resolution	79
6.4.3	Vertexing Quality	81
6.4.4	Drift Chamber Inefficiency	82
6.4.5	Momentum Scale	82
6.4.6	Physics Input Parameter	82
6.4.7	Background Uncertainty	85
6.4.8	Analysis Dependencies	86
6.4.9	Systematic Uncertainty: Summary	86
6.5	Form Factor Measurement: Summary	86
7	Asymmetry Measurement	88
7.1	Raw Asymmetry	89
7.1.1	Raw Asymmetry Calculation	89
7.1.2	Bias from Detector and Event Selection	89
7.1.3	Origin of Raw Asymmetry	93
7.2	Acceptance Corrected Asymmetry	95
7.3	Systematic Uncertainty	98
7.3.1	Smearing by Detector Resolution	98
7.3.2	$gM1$ Form Factor	99
7.3.3	Vertexing Quality	101

7.3.4	Drift Chamber Inefficiency	101
7.3.5	Other Physics Parameters	103
7.3.6	Background Subtraction	103
7.3.7	Analysis Dependency	103
7.3.8	Systematic Uncertainty: Summary	104
7.4	Asymmetry Measurement: Summary	104
8	Branching Ratio Measurement	105
8.1	Event Selection and Background Estimation	105
8.2	Systematic Uncertainty	109
8.2.1	Drift Chamber Inefficiency	109
8.2.2	Vertexing Quality	109
8.2.3	Normalization Ambiguity	110
8.2.4	$K_L \rightarrow \pi^+\pi^-e^+e^-$ Monte Carlo Generation	110
8.2.5	Background Subtraction	110
8.2.6	Analysis Dependency	113
8.2.7	External Systematic Sources	113
8.2.8	Systematic Uncertainty: Summary	113
8.3	Branching Ratio Measurement: Summary	113
9	Discussion	115
9.1	Form Factor Measurement	115
9.2	Asymmetry Measurement	117
9.3	Branching Ratio Measurement	117
9.4	Remarks and Future Prospects	118
10	Conclusion	119
A	Maximum Likelihood Method	121
A.1	Definition	121
A.2	Use of Monte Carlo	122
A.3	Reduction of Monte Carlo Generation	123
A.4	Fit Example	124
B	Pp0kine: Kinematics with a Missing Particle	125

List of Figures

1.1	$K_L \rightarrow \pi^+\pi^-\gamma$ decay process.	7
1.2	The photon spectrum in $K_L \rightarrow \pi^+\pi^-\gamma$	7
1.3	$K_L \rightarrow \pi^+\pi^-e^+e^-$ decay process.	9
1.4	Critical angles in $K_L \rightarrow \pi^+\pi^-e^+e^-$	10
1.5	E_γ^* distribution of $K_L \rightarrow \pi^+\pi^-\gamma$ in the kaon center-of-mass frame.	12
2.1	KTeV beamline and detector layout.	16
2.2	KTeV E799-II Detector.	18
2.3	A cross section of the drift chamber.	19
2.4	TDC time distribution of drift chamber.	20
2.5	SOD distribution.	21
2.6	The V and V' trigger hodoscope planes.	22
2.7	The KTeV electromagnetic Calorimeter.	23
2.8	E/p for electrons in K_{e3} decays, where E means an energy deposit in the calorimeter, and p denotes a momentum measured by the spectrometer.	25
2.9	The calorimeter intrinsic energy resolution measured in K_{e3} events as a function of electron momentum.	25
2.10	The schematic view of RC6, facing downstream. The beam passed through the inner aperture. The perimeter of outer circle fit right with the vacuum pipe. The other RCs were basically similar in a form but the dimensions seen in Table 2.2.	27
2.11	SA4 from upstream.	27
2.12	The Collar Anti just in front of the calorimeter.	27
2.13	The HA hodoscope.	28
2.14	The Mu2 counter.	28
2.15	Data acquisition system. Three planes were used for Level 3 trigger and the other was for online monitoring of the detector performance and online calibration.	33
3.1	Momentum distribution of the generated kaons.	37
3.2	K_L decay Z-distribution of Monte Carlo generated kaons.	37
3.3	E/p distribution of hadronic shower samples.	40
3.4	Electromagnetic and hadronic shower comparison.	41

4.1	Schematic view of the classification of hit pairs.	44
4.2	E/p comparison.	47
5.1	Mass distribution after basic cut.	52
5.2	Total momentum distribution of four charged tracks.	54
5.3	Total momentum from each background source.	54
5.4	Vertex χ^2 distribution.	55
5.5	M_{ee} distribution.	56
5.6	M_{ee} distribution from each background source.	56
5.7	p_t^2 distribution.	57
5.8	pt^2 distribution from each background source.	57
5.9	Schematic view of Pp0kine.	58
5.10	Pp0kine distribution.	59
5.11	Pp0kine distribution from each background source.	59
5.12	Invariant mass distribution after final cuts.	61
5.13	Distribution of mass of $\pi^+\pi^-e^+e^-$	65
5.14	HCC threshold distribution.	67
6.1	$M_{\pi\pi}$ distribution between data and Monte Carlo with a constant g_{M1} in the decay $K_L \rightarrow \pi^+\pi^-e^+e^-$	71
6.2	The diagrams for the vector meson intermediate model.	72
6.3	The g_{M1} form factor effect in the decay $K_L \rightarrow \pi^+\pi^-\gamma$	73
6.4	Fit result of a_1/a_2 and a_1 from two dimensional maximum likelihood method.	75
6.5	Comparison of various distributions between data and Monte Carlo.	76
6.6	The comparisons of $M_{\pi\pi}$ distribution between data and Monte Carlo with and without the form factor.	77
6.7	Fit results of a_1/a_2 and a_1	79
6.8	Fit results of a_1/a_2 and a_1 for the ten pseudo data samples.	80
6.9	Data and Monte Carlo comparison in vertex χ^2 for $K_L \rightarrow \pi^+\pi^-e^+e^-$	81
6.10	Data and modified Monte Carlo comparison in vertex χ^2 for $K_L \rightarrow \pi^+\pi^-e^+e^-$	81
6.11	Data and Monte Carlo comparison for M_{ee} distribution in the decay $K_L \rightarrow \pi^+\pi^-\pi_D^0$	83
6.12	Data and Monte Carlo comparison of track illumination at DC1 in Y view.	84
6.13	Distributions of $M_{\pi\pi ee}$ from $K_L \rightarrow \pi^+\pi^-\pi_D^0$ of data and Monte Carlo.	85
6.14	Averaged $M_{\pi\pi}$ as a function of $(E_{\pi 1} + E_{\pi 2})$ for $K_L \rightarrow \pi^+\pi^-\pi_D^0$ data and Monte Carlo simulation.	85
7.1	ϕ distribution of data overlaid with the Monte Carlo.	90
7.2	Distribution of $(2\cos\phi\sin\phi)$ from data, overlaid with the Monte Carlo.	90
7.3	ϕ distribution of identified $K_L \rightarrow \pi^+\pi^-\pi_D^0$	92
7.4	Raw asymmetries at different mass regions.	92

7.5	Relation between the <i>input</i> and <i>raw asymmetry</i>	94
7.6	Distributions of $K_L \rightarrow \pi^+\pi^-e^+e^-$ with respect to ϕ	96
7.7	Signal acceptance as a function of ϕ	97
7.8	The ϕ distribution of acceptance corrected data.	97
7.9	The resolution effect causing wrong sign events.	100
7.10	The difference between real ϕ and reconstructed ϕ	100
7.11	X track swapping.	101
7.12	The resolution effect causing wrong sign events with $M_{ee} < 2\text{MeV}/c^2$	102
7.13	The difference between real ϕ and reconstructed ϕ for events with $M_{ee} < 2\text{MeV}/c^2$	102
8.1	Invariant mass distribution after final cuts.	106
8.2	Invariant mass distribution with $0.0001 < p_t < 0.0002\text{GeV}^2/c^2$	107
8.3	Data and the Monte Carlo comparison after background subtraction.	108
8.4	Comparison between data and Monte Carlo estimation in the sideband.	112
9.1	Results on the DE form factor, a_1/a_2	116
9.2	$\theta_{\eta-\eta'}$ and DE branching ratio.	116

List of Tables

2.1	Positions and dimensions of the spectrometer elements.	18
2.2	Positions and dimensions of the photon vetoes.	26
2.3	Positions and dimensions of the detectors(downstream of the calorimeter).	28
2.4	The E799 four track trigger elements.	30
2.5	The KTeV-E799II run conditions.	34
3.1	The parameters referred from Malensek [7].	36
5.1	Signal to background ratio matrix table.	60
5.2	The signal acceptance at analysis each phase.	62
5.3	Backgrounds acceptance.	63
5.4	Cuts for $K_L^0 \rightarrow \pi^+\pi^-\pi_D^0$	64
5.5	Summary of the background level at the flux measurement.	66
5.6	Summary of systematic uncertainty in the flux measurement.	68
5.7	Summary of the flux calculation with $K_L^0 \rightarrow \pi^+\pi^-\pi_D^0$. Expected background was already subtracted.	69
6.1	Fixed physics parameters in the maximum likelihood fit. Values are reported by the Particle Data Group(PDG) [9] and the theoretical prediction [22].	74
6.2	Acceptance calculation dependency of the sample size.	78
6.3	Smearing effect by the detector resolution.	79
6.4	Stability to parameter fluctuations.	86
6.5	Background uncertainty	86
6.6	Deviations of analysis cut dependencies.	87
6.7	Systematic uncertainties.	87
7.1	<i>Raw asymmetries</i> at different mass regions.	91
7.2	Comparison between the <i>input</i> and <i>raw asymmetry</i>	93
7.3	Asymmetries of various data sets	98
7.4	Experimental Input Parameter.	103
7.5	Deviations of analysis cut dependencies in the <i>acceptance corrected asymmetry</i>	103

7.6 Summary of systematic uncertainties.	104
8.1 Background acceptance after final cut.	107
8.2 The signal acceptance at each analysis phase.	108
8.3 Stability to parameter fluctuations.	111
8.4 Summary of analysis dependency.	113
8.5 Summary of uncertainty in branching ratio measurement.	114

Abstract

CP violation in an angular asymmetry has been established in the decay $K_L \rightarrow \pi^+\pi^-e^+e^-$ based on 1162 events. Measured CP asymmetry, which appeared in the angular distribution between normals to $\pi^+\pi^-$ and e^+e^- planes, is $0.127 \pm 0.029(stat.) \pm 0.016(syst.)$. The form factor of M1 direct emission appeared in $K_L \rightarrow \pi^+\pi^-\gamma^*(\rightarrow e^+e^-)$ is determined as $a_1/a_2 = -0.684^{+0.031}_{-0.043}(stat.) \pm 0.053(syst.)$ and $a_1 = 1.05 \pm 0.14(stat.) \pm 0.18(syst.)$. The branching ratio has also been determined as $Br(K_L \rightarrow \pi^+\pi^-e^+e^-) = (3.55 \pm 0.11(stat.) \pm 0.08(syst.internal) \pm 0.14(syst.external)) \times 10^{-7}$.

Chapter 1

Introduction

The CP violation is a small effect, yet it has been one of the greatest discoveries in particle physics. Since its discovery in 1964, people have been eager for elucidating its origin, process and effect. Recently, we are finally recognizing its phenomenology in the electroweak physics. This thesis intends to show a part of such challenging efforts by exploring the decay " $K_L \rightarrow \pi^+\pi^-e^+e^-$."

In this introduction, we cover theoretical backgrounds of $K_L \rightarrow \pi^+\pi^-e^+e^-$ decay process. It starts with a historical overview on C, P and CP violations. Next, we describe phenomenology of the neutral kaon system and CP violation. In addition, we briefly introduce recent experimental status of its direct and indirect CP violation effects. We then study the decay $K_L \rightarrow \pi^+\pi^-e^+e^-$ process and the technique to measure the CP violation effect in this decay mode. Finally, we glance the overview of this thesis.

1.1 C, P, and CP Violation

Most of the theories in particle physics declare the existence of some kinds of symmetries in the framework. However, observations of symmetry breakings in nature have been a guide to a new theory, which declares underlying symmetry in the more fundamental level.

In particle physics, there are three interesting discrete symmetries; charge conjugation(C), parity, i.e., space inversion(P), and time reversal(T). These symmetry operations have eigenvalues of +1 and -1, called even and odd, respectively. Relativistic field theories require that the equations of motion must conserve its form under joint operations of C, P, and T. This is called a CPT theorem [1, 2]. The CPT theorem assures the equality of masses, lifetimes and magnitude of charges between particles and anti-particles. To date, no CPT violation has been observed experimentally.

At the dawn of modern particle physics, any physical processes were simply believed to be invariant under each operation of C, P, and T. In the early 50's, strange particles were found. Among them were those named " τ " and " θ ." Although they had the same lifetime and mass, these two particles decayed into different parity states, actually two pions and three pions respectively,

so that they were considered as different particles. In 1956, Lee and Yang insisted that no obvious evidence for the parity conservation had been found in the weak interaction [3]. They proposed experiments to test parity conservation in β decays of a polarized nuclei and so on. An experiment to test the invariance was performed in 1957 by Wu *et al.*[4], using the Gamow-Teller transition in ^{60}Co polarized nuclei, and they discovered the parity violation in the decay. With further studies on the weak interaction, it was found that C and P symmetries were fully violated, but still CP was thought to be invariant at that time.

In 1964, even CP symmetry was found to have a small but finite amount of violation in the long-lived neutral kaon system [5]. The long-lived kaon, K_L , which had been believed to be a pure CP odd state, was found to decay into CP even two pion state. Up to date, C, P and CP violations are known in the weak interaction only, and especially, CP violation has been observed only in the neutral kaon system.

Since the discovery of the CP violation, people have been exploring its mechanism and origin, and recently with sophisticated detectors and techniques, we have accumulated enough knowledge to almost clarify the nature of CP violation in the electroweak interaction.

1.2 CP violation in Neutral Kaon System

In this section, we explain phenomenological description of CP violation in the neutral kaon system and recent experimental status of them. First, we start with the phenomenology.

There are two kinds of neutral kaons in different eigenstates which are distinguished with strangeness of +1 and -1:

$$|K^0\rangle = |(d, \bar{s})\rangle, \quad |\bar{K}^0\rangle = |(\bar{d}, s)\rangle. \quad (1.1)$$

They are easily produced through the strong interaction, where the strangeness is conserved.

K^0 and \bar{K}^0 are defined as CP conjugate to each other:

$$CP|K^0\rangle = |\bar{K}^0\rangle, \quad (1.2-a)$$

$$CP|\bar{K}^0\rangle = |K^0\rangle, \quad (1.2-b)$$

with phase ambiguity, where CP means the CP transforming operation. Here we can choose the phase as above since the phase is not observable. If we define K_1 and K_2 as

$$|K_1\rangle = \frac{1}{\sqrt{2}}(|K^0\rangle + |\bar{K}^0\rangle), \quad (1.3-a)$$

$$|K_2\rangle = \frac{1}{\sqrt{2}}(|K^0\rangle - |\bar{K}^0\rangle), \quad (1.3-b)$$

these are CP eigenstates like

$$CP|K_1\rangle = |K_1\rangle \quad (\text{CP even}), \quad (1.4-a)$$

$$CP|K_2\rangle = -|K_2\rangle \quad (\text{CP odd}). \quad (1.4-b)$$

K^0 and \bar{K}^0 can transit to each other through $K^0 \leftrightarrow (2\pi, 3\pi \text{ etc.}) \leftrightarrow \bar{K}^0$, implying $\langle K^0 | H | \bar{K}^0 \rangle \neq 0$, where H includes the strong interaction H_S , and the weak interaction H_W causing decays. This phenomenon is called "mixing." Naturally, the mixing includes $\Delta S = 2$ transition.

To understand the mixing in the neutral kaon system in the rest frame, let us start from a time-dependent Schrödinger equation with two quantum states including the mixing like [6];

$$\begin{aligned}\phi(t) &= \alpha(t)|K^0\rangle + \beta(t)|\bar{K}^0\rangle, \\ i\frac{d}{dt}\begin{pmatrix} \alpha \\ \beta \end{pmatrix} &= \begin{pmatrix} \langle K^0 | H | K^0 \rangle & \langle K^0 | H | \bar{K}^0 \rangle \\ \langle \bar{K}^0 | H | K^0 \rangle & \langle \bar{K}^0 | H | \bar{K}^0 \rangle \end{pmatrix} \begin{pmatrix} \alpha \\ \beta \end{pmatrix} \\ &= \begin{pmatrix} \widetilde{M}_{11} & \widetilde{M}_{12} \\ \widetilde{M}_{21} & \widetilde{M}_{22} \end{pmatrix} \begin{pmatrix} \alpha \\ \beta \end{pmatrix}. \end{aligned} \quad (1.5)$$

Taking the second order of the weak interaction, we can rewrite \widetilde{M}_{ij} as a combination of two Hermitian matrices, M_{ij} and Γ_{ij} ;

$$\widetilde{M}_{ij} = M_{ij} - i\Gamma_{ij}/2 \quad (1.6-a)$$

$$M_{ij} = M_i\delta_{ij} + \langle i | H_W | j \rangle + \sum_{n \neq K^0, \bar{K}^0} P \frac{\langle i | H_W | n \rangle \langle n | H_W | j \rangle}{M_i - E_n} \quad (1.6-b)$$

$$\Gamma_{ij} = 2\pi \sum_{n \neq K^0, \bar{K}^0} \delta(M_i - E_n) \langle i | H_W | n \rangle \langle n | H_W | j \rangle, \quad (1.6-c)$$

where P means a principal value. The M is called mass matrix and Γ is called decay matrix, and its off-diagonal elements give the mixing between K^0 and \bar{K}^0 states.

We now consider the eigenvalue of this equation. We can rewrite

$$\phi(t) = \alpha'(t)|K_1\rangle + \beta'(t)|K_2\rangle = \alpha(t)|K^0\rangle + \beta(t)|\bar{K}^0\rangle \quad (1.7-a)$$

$$i\frac{d}{dt}\begin{pmatrix} \alpha' \\ \beta' \end{pmatrix} = \begin{pmatrix} \lambda_S & 0 \\ 0 & \lambda_L \end{pmatrix} \begin{pmatrix} \alpha' \\ \beta' \end{pmatrix} \quad (1.7-b)$$

$$\lambda_S = m_S - i\Gamma_S/2, \quad \lambda_L = m_L - i\Gamma_L/2, \quad (1.7-c)$$

where the eigenvalues are, in general, complex and $m_{L,S}$, $\Gamma_{L,S}$ are real.

Since only K_1 can decay into $\pi\pi^{*1}$, the Q value of K_1 is larger than that of K_2 . Therefore, K_2 lives longer than K_1 ($\Gamma_1 \gg \Gamma_2$). Until CP violation was observed in 1964, it was believed that the long lived kaon could have decayed only into odd CP state.

^{*1}Here is an explanation of CP state in 2π and 3π system:

1) 2π : $P\pi = -\pi$ and $C\pi^0 = \pi^0$, and $C\pi^\pm = \pi^\mp$. Because of Bose statistics, C is equivalent to P in $\pi^+\pi^-$ system. So $CP(\pi^+\pi^-) = (-1)^{2\ell} = +1$, where ℓ is an orbit angular momentum. For $2\pi^0$, an orbit angular momentum must be an even number from the Bose symmetry, thus $CP\pi^0\pi^0 = +1$.

2) 3π : For $\pi^+\pi^-\pi^0$, assuming the angular momentum of $\pi^+\pi^-$ is ℓ and a relative angular momentum between a π^0 and $\pi^+\pi^-$ system is L , it gives $CP(\pi^+\pi^-\pi^0) = (-1)^{2\ell+L+1}$. Since the angular momentum barrier forces to be $L = 0$ and $\ell = 0$, CP becomes negative. For $3\pi^0$, like 1), ℓ becomes zero. So $L = 0$ since the total momentum must be zero. Thus, $CP(\pi^0\pi^0\pi^0)$ must be negative.

1.2.1 Indirect CP Violation

CP violation was first observed as a signature of long lived kaons decaying into CP even two pion final states. This phenomenon is explained if the long lived kaon, K_L , is almost K_2 , but has an admixture of CP even K_1 state.

$$|K_L\rangle = \frac{1}{\sqrt{1+|\epsilon|^2}}(|K_2\rangle + \epsilon|K_1\rangle) = \frac{1}{\sqrt{2(1+|\epsilon|^2)}}((1+\epsilon)|K^0\rangle - (1-\epsilon)|\bar{K}^0\rangle), \quad (1.8-a)$$

$$|K_S\rangle = \frac{1}{\sqrt{1+|\epsilon|^2}}(|K_1\rangle + \epsilon|K_2\rangle) = \frac{1}{\sqrt{2(1+|\epsilon|^2)}}((1+\epsilon)|K^0\rangle + (1-\epsilon)|\bar{K}^0\rangle), \quad (1.8-b)$$

where we assume CPT invariance. The contamination of K_1 in the K_L causes the decay into CP even final state, such as two pions, and amount of CP asymmetry is determined by ϵ . The CP violation from the mixing asymmetry is called "indirect CP violation."

1.2.2 Direct CP Violation

The CP violation can be observed in a decay process also. This is called "direct CP violation." If we define decay amplitudes to a CP eigenstate f_{CP} like

$$\begin{aligned}a_{f_{CP}} &= \langle f_{CP} | H_{eff} | K^0 \rangle \\ \bar{a}_{f_{CP}} &= \langle f_{CP} | H_{eff} | \bar{K}^0 \rangle, \end{aligned} \quad (1.9)$$

direct CP violation means $a_{f_{CP}} \neq \bar{a}_{f_{CP}}$. Let us choose CP even final state, f_{CP} , and define a CP violating parameter:

$$r_{f_{CP}} = \frac{\langle f_{CP} | H_{eff} | K_L \rangle}{\langle f_{CP} | H_{eff} | K_S \rangle}. \quad (1.10)$$

Substituting Equation 1.9 into Equation 1.10, we obtain

$$r_{f_{CP}} = \frac{(a_{f_{CP}} - \bar{a}_{f_{CP}}) + \epsilon(a_{f_{CP}} + \bar{a}_{f_{CP}})}{(a_{f_{CP}} + \bar{a}_{f_{CP}}) + \epsilon(a_{f_{CP}} - \bar{a}_{f_{CP}})}. \quad (1.11)$$

If $a_{f_{CP}} \neq \bar{a}_{f_{CP}}$, not only ϵ term (i.e., indirect CP violation) but also the difference between $a_{f_{CP}}$ and $\bar{a}_{f_{CP}}$ contribute to the CP violation. Defining the decay asymmetry as

$$\chi_{f_{CP}} = \frac{a_{f_{CP}} - \bar{a}_{f_{CP}}}{a_{f_{CP}} + \bar{a}_{f_{CP}}}, \quad (1.12)$$

we can rewrite Equation 1.10 as

$$r_{f_{CP}} = \frac{\epsilon + \chi_{f_{CP}}}{1 + \epsilon\chi_{f_{CP}}} \approx \epsilon + \chi_{f_{CP}} \quad (1.13)$$

where we used an empirical fact that ϵ is very small, $\sim 10^{-3}$. Equation 1.13 shows CP violation can be separated into two effects.

The direct CP violation was predicted by many people. Among them, Kobayashi and Maskawa showed that CP violation results by extending the quark mixing from four quarks to six quarks [33],

which is now a part of the Standard Model. Since then, many searches have been performed, and finally, a finite direct CP violation has been reported by NA31 and KTeV collaborations in the neutral kaon system [34, 35].

1.2.3 Experimental Results of Indirect CP Violation

We briefly introduce experimental results in the field of indirect CP violation. We here show results from $K_L \rightarrow \pi\pi$, a semi-leptonic K decay, and a radiative K decay, $K_L \rightarrow \pi^+\pi^-\gamma$. The decay $K_L \rightarrow \pi^+\pi^-\gamma$ is strongly related to the decay $K_L \rightarrow \pi^+\pi^-e^+e^-$, which is the topic of this thesis.

Indirect CP violation in $K_L \rightarrow \pi\pi$

CP violation was first observed in $K_L \rightarrow \pi^+\pi^-$ by V.L.Fitch, J.W.Cronin *et al.* in 1964[5]. This was a direct observation of indirect CP violation with CP even final state, $\pi^+\pi^-$. This implies that K_L includes the CP even small component of K_1 which decays into $\pi^+\pi^-$ final state.

Now the branching ratio is known to be [9]

$$BR(K_L \rightarrow \pi^+\pi^-) = (2.067 \pm 0.035) \times 10^{-3}. \quad (1.14)$$

CP violation was also observed in a final state, $K_L \rightarrow \pi^0\pi^0$,

$$BR(K_L \rightarrow \pi^0\pi^0) = (9.36 \pm 0.20) \times 10^{-4}. \quad (1.15)$$

The related useful CP violation parameters are also provided from the decay amplitudes:

$$\begin{aligned} \eta_{+-} &\equiv \frac{Amp(K_L \rightarrow \pi^+\pi^-)}{Amp(K_S \rightarrow \pi^+\pi^-)} = |\eta_{+-}| \exp(i\Phi_{+-}), \\ \eta_{00} &\equiv \frac{Amp(K_L \rightarrow \pi^0\pi^0)}{Amp(K_S \rightarrow \pi^0\pi^0)} = |\eta_{00}| \exp(i\Phi_{00}). \end{aligned}$$

Recent results of these parameters are [9]

$$\begin{aligned} |\eta_{+-}| &= (2.285 \pm 0.019) \times 10^{-3}, & \Phi_{+-} &= 43.5^\circ \pm 0.6^\circ, \\ |\eta_{00}| &= (2.275 \pm 0.019) \times 10^{-3}, & \Phi_{00} &= 43.4^\circ \pm 1.0^\circ. \end{aligned}$$

Experimentally, a simultaneous collection of $K_L \rightarrow \pi^+\pi^-, \pi^0\pi^0$ and $K_S \rightarrow \pi^+\pi^-, \pi^0\pi^0$ decays gives more precise measurements of the ratio, $|\eta_{00}/\eta_{+-}|$, and the phase difference, $\Delta\Phi \equiv \Phi_{00} - \Phi_{+-}$ [9]:

$$|\frac{\eta_{00}}{\eta_{+-}}| = 0.9956 \pm 0.0023, \quad \Delta\Phi = -0.1^\circ \pm 0.8^\circ.$$

Indirect CP violation in $K_L \rightarrow \pi^\pm \ell^\mp \nu$

Another place to observe the CP violating effect is the charge asymmetry in kaon semileptonic decay, $K_L \rightarrow \pi^\pm \ell^\mp \nu$. The charge asymmetry is defined as

$$\delta \equiv \frac{\Gamma(K_L \rightarrow \pi^-\ell^+\nu_\ell) - \Gamma(K_L \rightarrow \pi^+\ell^-\nu_\ell)}{\Gamma(K_L \rightarrow \pi^-\ell^+\nu_\ell) + \Gamma(K_L \rightarrow \pi^+\ell^-\nu_\ell)}. \quad (1.16)$$

These decay amplitudes indicate $|K^0\rangle$ and $|\bar{K}^0\rangle$ composition of the K_L , since an ℓ^+ can come only from a K^0 decay, while ℓ^- can come only from \bar{K}^0 decay, as long as the “ $\Delta S = \Delta Q$ rule” holds. CPLEAR experiment at CERN reported that a deviation from $\Delta S = \Delta Q$ rule in K decay is consistent with zero [10]. Therefore, the charge asymmetry is calculated from relative amplitudes of $1 + \epsilon$ for $K^0 \rightarrow \pi^-\ell^+\nu_\ell$, and $1 - \epsilon$ for $\bar{K}^0 \rightarrow \pi^+\ell^-\nu_\ell$:

$$\delta = \frac{|1 + \epsilon|^2 - |1 - \epsilon|^2}{|1 + \epsilon|^2 + |1 - \epsilon|^2} \approx 2\text{Re}(\epsilon). \quad (1.17)$$

Averaging the results from $K_L \rightarrow \pi^\pm e^\mp \nu$ (called “ $Ke3$ ”), and $K_L \rightarrow \pi^\pm \mu^\mp \nu$ (called “ $K\mu3$ ”), the experimental result was reported [9]:

$$\delta = (3.27 \pm 0.12) \times 10^{-3}. \quad (1.18)$$

Using the phase of ϵ , this corresponds to $|\epsilon| = (2.25 \pm 0.09) \times 10^{-3}$.

These facts indicate that the same mixing mechanism is(at least) mostly responsible for CP violation effects in $K_L \rightarrow \pi\pi$ and the semileptonic decays.

CP violation in $K_L \rightarrow \pi^+\pi^-\gamma$

The decay process of $K_L \rightarrow \pi^+\pi^-\gamma$ consists of (a) an inner bremsstrahlung(IB) component associated with the CP violating decay, $K_L \rightarrow \pi^+\pi^-$, and (b) an $M1$ direct photon emission(DE) component of a CP conserving magnetic dipole moment [29](Figure 1.1)*².

The simultaneous existence of IB and DE amplitudes implies that the final state contains both $CP = +1$ and -1 states.

The radiative photon spectrum from this decay mode becomes a superposition of these two amplitudes. The photon spectrum of $K_{S,L} \rightarrow \pi^+\pi^-\gamma$ in the kaon center-of-mass system measured by Fermilab E731 experiment is shown in Figure 1.2 [37]. The dotted line is obtained from the $K_S \rightarrow \pi^+\pi^-\gamma$ photon spectrum, which is completely dominated by IB component. The data points indicate the E_γ spectrum for the K_L data. For the K_L decay, there is an enhancement in the higher photon energy region over $K_S \rightarrow \pi^+\pi^-\gamma$. This is naturally understood to be the DE component in the K_L decay.

Experimental results [36, 37, 38] on the branching ratio of $K_S \rightarrow \pi^+\pi^-\gamma$ is

$$\frac{\Gamma(K_S \rightarrow \pi^+\pi^-\gamma, E_\gamma^* > 20\text{MeV})}{\Gamma(K_S \rightarrow \pi^+\pi^-)} = (7.10 \pm 0.16) \times 10^{-3}(\text{IB}), \quad (1.19)$$

*²General formalism on radiative K decays is found in Ref. [20, 21]. In this thesis, in accordance with Ref. [29], we take the highest order of the magnetic dipole expansion, $M1$, which corresponds to a final state with a CP eigenstate, $CP = (-1)^1 = -1$. Note that the bremsstrahlung amplitude only includes CP even states.

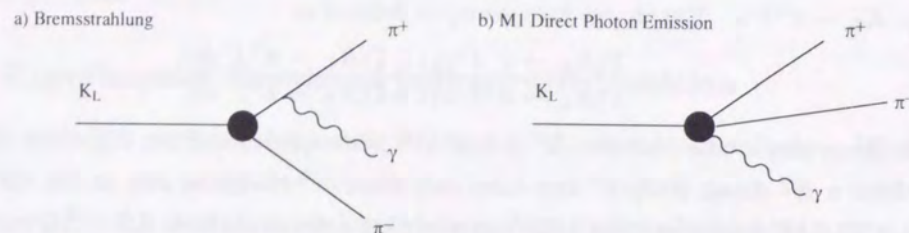


Figure 1.1: Major $K_L \rightarrow \pi^+\pi^-\gamma$ decay process. (a) an inner bremsstrahlung (IB) component associated with the CP violating decay, $K_L \rightarrow \pi^+\pi^-$, and (b) an M1 direct photon emission (DE) component of a CP conserving magnetic dipole moment.

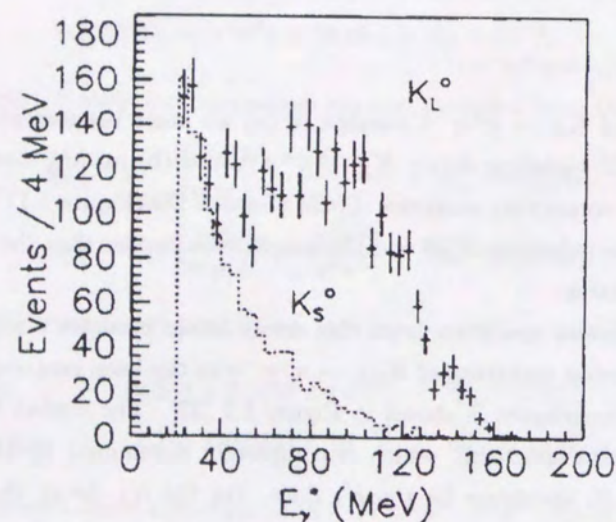


Figure 1.2: The photon spectrum in $K_L \rightarrow \pi^+\pi^-\gamma$ [37]. The data points indicate the E_γ spectrum for the K_L data. The dotted line is the same spectrum for the K_S data, rescaled to the K_L data.

corresponding to the IB term. The QED prediction of this ratio is 7.01×10^{-3} [39], in good agreement with the experimental result. The K_L data was fitted with IB component from K_S data and a pure DE spectrum based on Ref. [29]:

$$\frac{\Gamma(K_L \rightarrow \pi^+\pi^-\gamma, E_\gamma^* > 20\text{MeV})}{\Gamma(K_L \rightarrow \pi^+\pi^-)} = (7.31 \pm 0.38) \times 10^{-3} (\text{IB}) \quad (1.20\text{-a})$$

$$+ (15.7 \pm 0.7) \times 10^{-3} (\text{DE}) [37]. \quad (1.20\text{-b})$$

This indicates the existence of two components in the K_L decay.

1.3 $K_L \rightarrow \pi^+\pi^-e^+e^-$ Decay

This section describes a theoretical and experimental interpretation for the decay $K_L \rightarrow \pi^+\pi^-e^+e^-$ from an aspect of CP violation.

In the previous section, we looked at theoretical and experimental results of $K_L \rightarrow \pi^+\pi^-\gamma$. If we consider a virtual transition of the photon, $\gamma^* \rightarrow e^+e^-$, another CP violating effect will appear in this decay. Here, we explain how CP violating effect arises in this decay.

1.3.1 Decay Processes

We start this section with a brief introduction to the theoretical overview of the physics process in $K_L \rightarrow \pi^+\pi^-e^+e^-$. We first define decay amplitudes contributing to this decay. Similarly to the decay $K_L \rightarrow \pi^+\pi^-\gamma$, the most dominant contribution is the M1 magnetic dipole direct emission (DE) and the inner bremsstrahlung photon emission (IB).

The dominant decay amplitude of

$$K_L(P) \rightarrow \pi^+(p_+)\pi^-(p_-)e^+(k_+)e^-(k_-) \quad (1.21)$$

has the form

$$\mathcal{M}(K_L \rightarrow \pi^+\pi^-e^+e^-) = \mathcal{M}_{br} + \mathcal{M}_{mag}, \quad (1.22)$$

where

$$\mathcal{M}_{br} = e|f_S|g_{BR}\left[\frac{p_+\cdot\mu}{p_+\cdot k} - \frac{p_-\cdot\mu}{p_-\cdot k}\right]\frac{e}{k^2}\bar{\mu}(k_-)\gamma^\mu\mu(k_+), \quad (1.23\text{-a})$$

$$\mathcal{M}_{mag} = e|f_S|\frac{g_{M1}}{M_K^4}\epsilon_{\mu\nu\rho\sigma}k^\nu p_+^\rho p_-^\sigma\frac{e}{k^2}\bar{\mu}(k_-)\gamma^\mu\mu(k_+). \quad (1.23\text{-b})$$

The terms \mathcal{M}_{br} and \mathcal{M}_{mag} denote the bremsstrahlung and magnetic dipole, respectively. The coefficients appearing there are

$$g_{BR} = \eta_{+-}e^{i\delta_0},$$

$$g_{M1} = i(0.76)e^{i\delta_1},$$

and $|f_S|$ is defined by

$$\Gamma(K_S \rightarrow \pi^+\pi^-) = \frac{|f_S|^2}{16\pi m_K} \left[1 - \frac{4m_\pi^2}{m_K^2}\right]. \quad (1.25)$$

The η_\pm is defined as the ratio of amplitudes $\text{Amp}(K_L \rightarrow \pi^+\pi^-)/\text{Amp}(K_S \rightarrow \pi^+\pi^-)$ as shown in Section 1.2.3, and $\delta_{0(1)}$ is a phase shift in the final-state interactions in the $\pi\pi$ system with $I = 0(1)$ wave state.

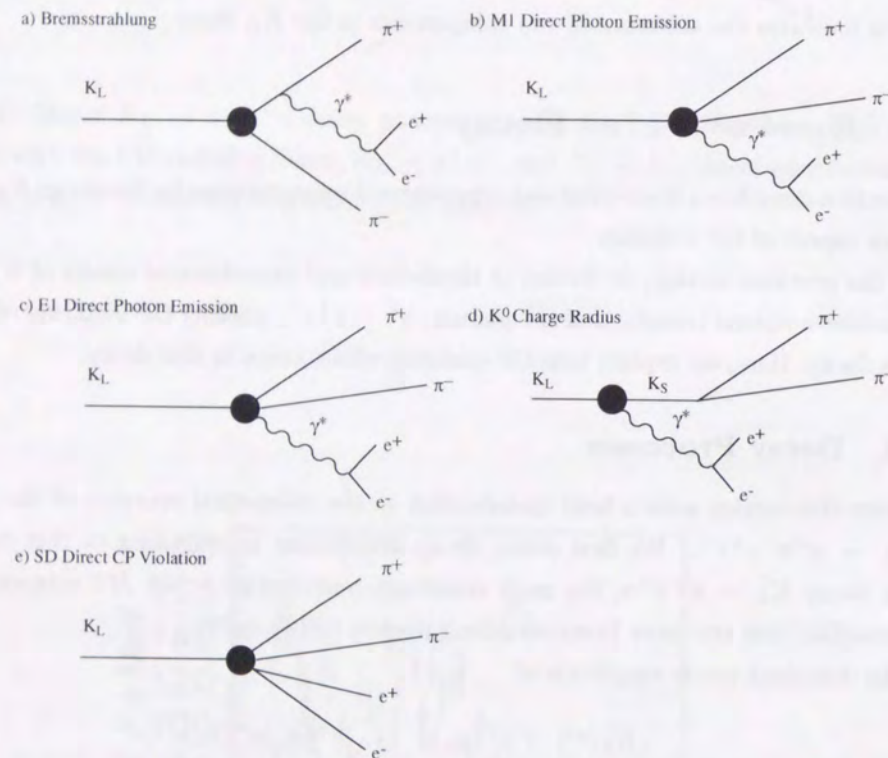


Figure 1.3: $K_L \rightarrow \pi^+\pi^-e^+e^-$ decay process. Besides major contributions of a) Inner Bremsstrahlung and b) M1 direct emission, there are other small contributions.

In addition, there are three small contributions; E1 electro dipole direct emission, charge radius and short distance direct CP violating amplitudes.

By integrating over all parameters, the branching ratio is calculated as

$$\text{Br}(K_L \rightarrow \pi^+\pi^-e^+e^-) \approx 3 \times 10^{-7} [22, 23]. \quad (1.26)$$

1.3.2 Indirect CP violation

Here we define critical parameters in $K_L \rightarrow \pi^+\pi^-e^+e^-$. This decay kinematics is defined completely with five kinematical parameters; invariant mass of $\pi^+\pi^-$, invariant mass of e^+e^- , an angle θ_{π^+} between the directions of electrons and π^+ in the pions center-of-mass frame, and an angle

θ_{e^+} between the directions of pions and e^+ in the electrons center-of-mass frame. The angle ϕ , which is of most interest in this thesis, is defined in terms of unit vectors constructed from the pion momenta p_\pm and lepton momenta k_\pm in the K_L rest frame:

$$\begin{aligned} \mathbf{n}_\pi &= (p_+ \times p_-)/|p_+ \times p_-|, \quad \mathbf{n}_\ell = (k_+ \times k_-)/|k_+ \times k_-|, \\ \mathbf{z} &= (p_+ + p_-)/|p_+ + p_-|, \\ \sin \phi &= \mathbf{n}_\pi \times \mathbf{n}_\ell \cdot \mathbf{z}, \quad \cos \phi = \mathbf{n}_\pi \cdot \mathbf{n}_\ell. \end{aligned} \quad (1.27)$$

Thus, the angle ϕ is simply understood as an angle defined between normals to $\pi^+\pi^-$ and e^+e^- decay planes in the K_L rest frame. The schematic view of these angles is shown in Figure 1.4.

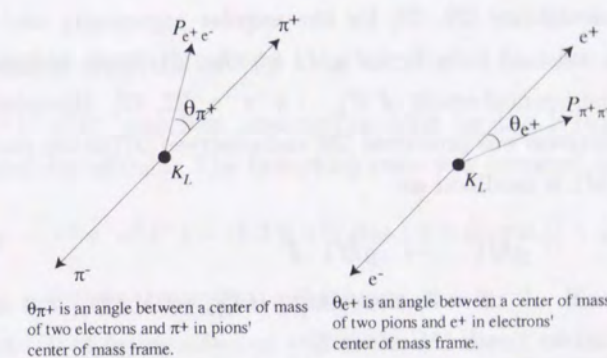
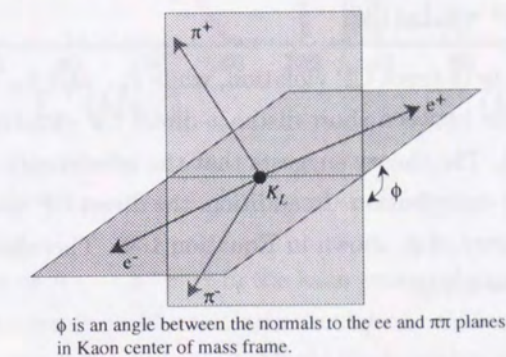


Figure 1.4: Critical angles in $K_L \rightarrow \pi^+\pi^-e^+e^-$.

Integrating over all kinematic variables except for ϕ , and ignoring small contributions, the differential cross section in terms of these angles is written as follows;

$$\frac{d\Gamma}{d\phi} = \Gamma_1 \cos^2 \phi + \Gamma_2 \sin^2 \phi + \Gamma_3 \sin \phi \cos \phi. \quad (1.28)$$

To identify the CP-violating terms in this expansion, we write the terms under the CP transformation, $p_\pm \rightarrow -p_\mp$, $k_\pm \rightarrow -k_\mp$, which gives;

$$\begin{aligned} \cos \phi &\rightarrow +\cos \phi, \\ \sin \phi &\rightarrow -\sin \phi. \end{aligned} \quad (1.29)$$

Those constants were evaluated numerically in Ref. [23]. The Γ_3 is the CP violating contribution, which is caused by the interference between IB and DE terms. In this sense, this is indirect CP violation. This contribution gives the angular asymmetry of

$$Asym. = \frac{\int_0^{\pi/2} \frac{d\Gamma}{d\phi} d\phi - \int_{\pi/2}^{\pi} \frac{d\Gamma}{d\phi} d\phi}{\int_0^{\pi/2} \frac{d\Gamma}{d\phi} d\phi + \int_{\pi/2}^{\pi} \frac{d\Gamma}{d\phi} d\phi} \approx 14\% [22, 23], \quad (1.30)$$

where we folded the distribution within $-2\pi < \phi < 0$ over $0 < \phi < 2\pi$ for simplicity. This suggests that there is a large CP violating effect in this decay mode.

1.3.3 Direct CP violation

The angle ϕ is related to indirect CP violation, while θ_{π^+} and θ_{e^+} is expected to exhibit direct CP violation by interference between short-distance direct CP violating term and other contributions at very small level [23]. The theory suggests that the interference can be at most of order 10^{-6} as compared with the DE contribution. In addition, the direct CP violating effect does not contribute to the angular asymmetry of ϕ , shown in Equation 1.30. Therefore, the direct CP violating effect can be neglected in this study.

1.3.4 $gM1$ Form Factor

The theoretical calculations [22, 23] for the angular asymmetry and branching ratio of $K_L \rightarrow \pi^+\pi^-e^+e^-$ used a constant form factor $gM1$ for the M1 direct emission contribution, which was taken from the experimental result of $K_L \rightarrow \pi^+\pi^-\gamma$ [22, 37]. However, an effect of vector meson intermediate contribution was predicted [29] and observed [37] in the parent process, $K_L \rightarrow \pi^+\pi^-\gamma$. The form factor $gM1$ is modified as;

$$gM1 \rightarrow gM1 \cdot F$$

$$F = a_1[(M_\rho^2 - M_K^2) + 2M_KE_\gamma]^{-1} + a_2, \quad (1.31)$$

where M_ρ is the mass of ρ vector meson, M_K is the mass of kaon and E_γ is the energy of the photon in the K_L rest frame. Figure 1.5 shows distributions of E_γ with vector meson intermediate contribution or a constant $gM1$ [37]. Clearly, inclusion of the vector meson effect in the form factor gives a better agreement.

Besides $K_L \rightarrow \pi^+\pi^-\gamma$, the form factor $gM1$ can be independently measured with $K_L \rightarrow \pi^+\pi^-e^+e^-$, in principle. The measurement should improve the estimate of the branching ratio and CP violating asymmetry of $K_L \rightarrow \pi^+\pi^-e^+e^-$. From a point of view of our experiment, the uncertainty in $gM1$ gave an uncertainty in the branching ratio measurement up to 10%, while the expected statistical uncertainty would be 3%. The accuracy of the branching ratio measurement would be systematic dominant unless we improve the accuracy of $gM1$ form factor.

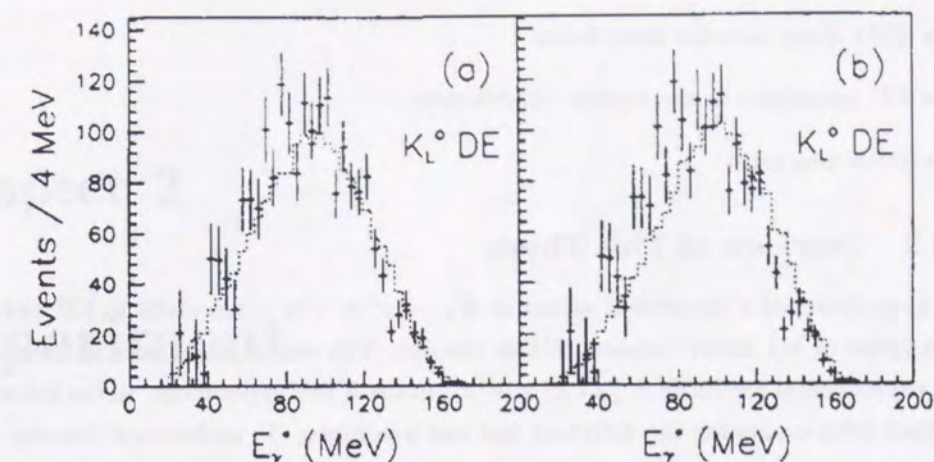


Figure 1.5: E_γ^* distribution of $K_L \rightarrow \pi^+\pi^-\gamma$ in the kaon center-of-mass frame [37]. Dots are from data and dotted histograms are from Monte Carlo simulation. a) Monte Carlo with a form factor taking account of vector meson intermediate. b) Monte Carlo with a constant $gM1$.

1.3.5 Experimental Status of $K_L \rightarrow \pi^+\pi^-e^+e^-$

The decay $K_L \rightarrow \pi^+\pi^-e^+e^-$ was first observed in 1998 by the KTeV collaboration with 46 events [40] based on one day of data. The branching ratio was reported as:

$$Br(K_L \rightarrow \pi^+\pi^-e^+e^-) = (3.2 \pm 0.6(stat.) \pm 0.4(syst.)) \times 10^{-7}, \quad (1.32)$$

and this result agrees well with theoretical predictions, 3×10^{-7} . However, statistics was not enough to evaluate the CP violating effect as well as the M1 direct emission form factor.

1.4 Summary

1.4.1 Purpose of This Study

The decay $K_L \rightarrow \pi^+\pi^-e^+e^-$ is a fruitful field to explore CP violation in particle physics. This mode is expected to show not only the fourth appearance of indirect CP violation, but also the significant CP violating effect.

In addition, we can measure the form factor of M1 direct emission contribution in $K_L \rightarrow \pi^+\pi^-e^+e^-$ for the first time. This serves as a cross check of the form factor measured with $K_L \rightarrow \pi^+\pi^-\gamma$.

Therefore, we will extract the following parameters of $K_L \rightarrow \pi^+\pi^-\pi^+\pi^-$ in this thesis:

- $gM1$ direct emission form factor.
- CP asymmetry in the angular distribution.
- Branching ratio.

1.4.2 Overview of This Thesis

We have discussed a theoretical aspect of $K_L \rightarrow \pi^+\pi^-\pi^+\pi^-$, especially in CP violation and the form factor of M1 direct emission in this chapter. The rest of this thesis is devoted to describe new experimental results on $K_L \rightarrow \pi^+\pi^-\pi^+\pi^-$ in the KTeV experiment. In the following chapters, we start from explaining the detectors and run conditions. To understand detector response and acceptance, we utilized a Monte Carlo simulation, described in Chapter 3. Event reconstruction strategy and its scheme in the analysis are explained in Chapter 4. After that, we describe event selection to extract the signal.

We proceed to physics analyses after the signal is obtained. First, we determine the form factor of M1 direct emission, and then feedback the measured parameters to the Monte Carlo simulation to improve its accuracy. Next, the angular asymmetry from the CP violating effect is evaluated and then, the branching ratio of this mode is determined. Finally, we summarize and discuss our results.

Chapter 2

Experiment

This analysis on $K_L \rightarrow \pi^+\pi^-\pi^+\pi^-$ was performed as a part of a K_L rare decay search program KTeV-E799II in the Fermi National Accelerator Laboratory in 1997.

This chapter describes the KTeV experiment and consists of three parts; short explanation of the data collecting strategy of $K_L \rightarrow \pi^+\pi^-\pi^+\pi^-$, K_L beam and detector configuration, and data taking. We briefly mention the issues only related to the $K_L \rightarrow \pi^+\pi^-\pi^+\pi^-$ analysis. More detailed information about the KTeV experiment can be found in KTeV Technical Design Report [8] and KTeV internal documents.

The final state of the decay $K_L \rightarrow \pi^+\pi^-\pi^+\pi^-$ consists of four charged tracks, $\pi^+\pi^-\pi^+\pi^-$. This means if all four particles are identified and momenta are measured well, the whole kinematics and decay topology can be fully reconstructed.

The decay $K_L \rightarrow \pi^+\pi^-\pi^+\pi^-$ was normalized by $K_L \rightarrow \pi^+\pi^-\pi^0$ with π^0 Dalitz decay (denoting " π_D^0 "), $\pi^0 \rightarrow e^+e^-\gamma$. In order to identify this decay, we should also detect a photon and measure the photon energy and position. Since this decay has a final state of $\pi^+\pi^-\pi^+\pi^-\gamma$, this can be a significant background if one photon is missed. Therefore, photon vetoes were also required to veto events with escaping particles.

From this regard, detector elements are required to have following functions:

- Momentum measurement of charged particles
- Identification of e^\pm , π^\pm and μ^\pm .
- Photon energy and position measurement.
- Vetoes for the particles escaping from the detector.

The KTeV detector was capable of satisfying these requirements. We here describe the KTeV detector system in this context.

Before proceeding to the description of the experiment, the coordinate system of the KTeV experiment is defined here. A target is the origin of the coordinate, and downstream horizontal direction along beams is defined as the positive Z axis. The Y axis is defined as vertically pointing up. The three axes are defined with the right-handed coordinate system.

2.1 K_L Beam Production

This section describes the neutral beam production.

A 800 GeV primary proton beam was incident on a BeO target, to create various particles. Among them, neutral particles were selected by series of dipole magnets and collimators. The beam was then transported to the experimental hall.

2.1.1 Beam Production

Tevatron main ring in Fermilab provided 800GeV protons to KTeV. Protons were delivered over a 23 seconds "spill" in every 60 seconds. The intensity of the proton beam provided to KTeV was 2.5×10^{12} to 5.0×10^{12} protons per spill. Each spill has microstructure divided with 53 MHz Tevatron radio frequency(RF), that is, a few nano second wide proton bunch delivered in every 19 nsec.

The primary proton beam was incident on the target with the vertical angle of 4.8 mrad in order to optimize both the higher neutral kaon flux and the better kaon to neutron flux ratio. The target was made of beryllium oxide(BeO) with the dimensions of 3×3 mm transverse to the proton beam and 30 cm(0.9 interaction lengths) along the beam.

2.1.2 Sweeper and Collimeter

A sweeper magnet(NM2S1), which was located two meters downstream from the target, removed the remaining primary protons from the neutral beam. The primary proton beam was absorbed by a beam dump.

Another three dipole magnets were placed in the region of $Z = 14$ to 93m from the target, to remove charged particles from the beam, including upstream decay, muons from the beam dump, and interaction products.

A Pb filter(NM2PB) at $Z = 18.5$ m converted photons in the neutral beam into e^+e^- to remove them effectively.

Two nearly parallel neutral beams were defined with a primary collimeter with two square holes placed at $Z = 19.8$ meters. A steel slab collimeter at $Z = 38.8$ m prevented particles crossing from one beam to the other.

At $Z = 85$ m, a collimeter named "the defining collimeter", which was made of steel, defined the final dimensions of the beams. The beams formed square dimensions of $0.5 \text{ mrad} \times 0.5 \text{ mrad}$ for the first part of the run(winter run) and $0.7 \text{ mrad} \times 0.7 \text{ mrad}$ for the second part of the

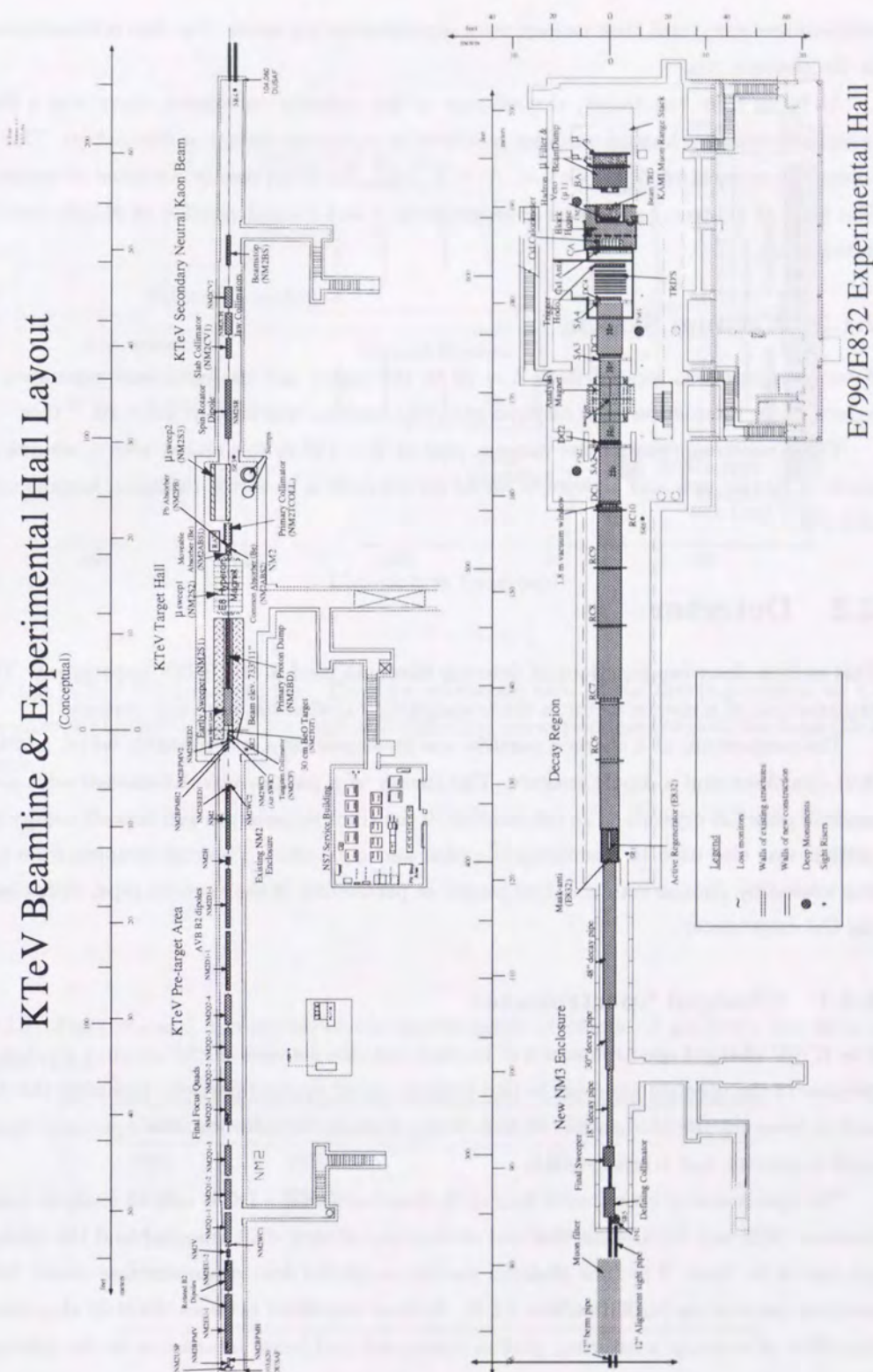


Figure 2.1: KTeV beamline and detector layout.

run(summer run), and their centers were separated by 1.6 mrad. The slab collimator was removed in the summer run.

At 90 m from the target, downstream of the defining collimator, there was a final sweeper magnet to remove charged particles produced in upstream decays or interaction. This provided a transverse momentum of 1.1 GeV/c. At this point, the beam mostly consisted of neutrons and K_L . The ratio of neutron and K was approximately 3 and a small number of K_S , Λ , and Ξ remained in the beam.

2.1.3 Vacuum System

A vacuum pipe was located from $Z = 22$ to 159 meter and its inside was evacuated in order to reduce beam interaction with residual gas. The vacuum was kept at 1.0×10^{-6} torr.

The downstream end of the vacuum pipe at $Z = 159$ m was sealed with a window, which was made of Kevlar web and aluminum mylar corresponding to 0.16% radiation lengths and diameter of 0.9 m.

2.2 Detector

This section describes functions of detector elements used in the KTeV experiment. This includes explanations of a spectrometer, an electromagnetic calorimeter, and veto system.

The momentum of a charged particle was measured by a spectrometer which consisted of four drift chambers and a dipole magnet. The energy of a photon was determined with a calorimeter made of pure CsI crystals. The information of the track momentum and deposit energy of a charged particle was also used to discriminate a pion and an electron. Photons escaping from the detector was vetoed by photon veto counters placed at perimeters of the vacuum pipe, drift chambers, and the CsI calorimeter.

2.2.1 Charged Spectrometer

The KTeV charged spectrometer was located just downstream of the vacuum window. The main purpose of the spectrometer was to find trajectories of charged particles including the decay vertex and to measure the momentum of each charged track. In addition, the upstream chambers were used to provide fast trigger signals.

The spectrometer consisted of four drift chambers(DC1 – DC4) and an analysis magnet placed between DC2 and DC3. Positions and dimensions of each drift chamber and the analysis magnet are shown in Table 2.1. The position resolution of the drift chambers was about $100\mu\text{m}$ and a nominal momentum resolution was 0.5 %. Helium bags filled between the drift chambers to reduce the effect of multiple scattering, photon conversion and beam interaction in the spectrometer.

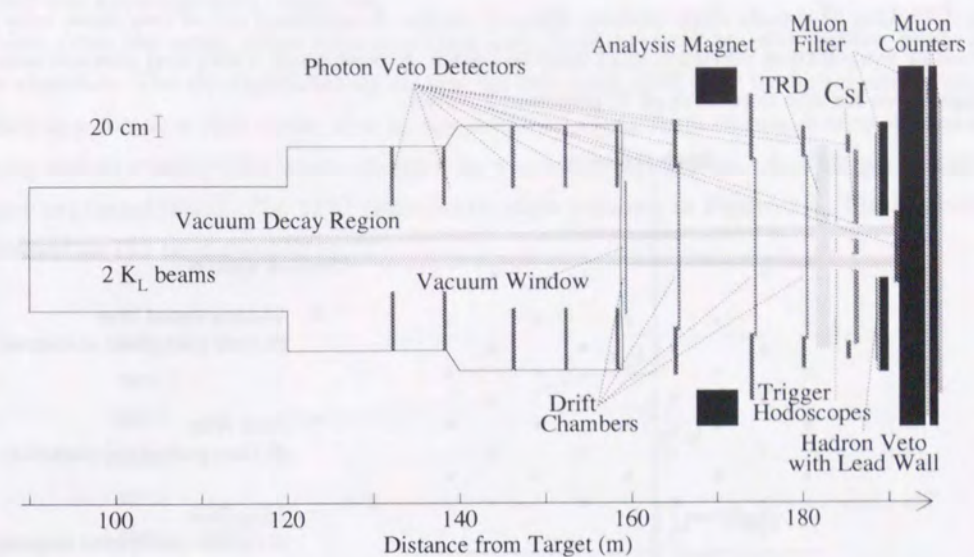


Figure 2.2: KTeV E799-II Detector. This is a schematic view of the detector region, as a downstream part of Figure 2.1. Note the scale of Z direction, corresponding the position from the target, is shrunk.

Table 2.1: Positions and dimensions of the spectrometer elements. Z positions are measured at upstream faces.

Elements	Z position(m)	Aperture(width(m) \times height(m))
DC1	159.42	1.30×1.30
DC2	165.57	1.64×1.44
Magnet	170.01	2.90×2.00
DC3	174.59	1.74×1.64
DC4	180.49	1.90×1.90

Drift Chamber

Figure 2.3 shows the cross section of each drift chamber. Each chamber had four sense plane for the detection of signals from passing charged tracks. A upstream set of two sense wire planes in a chamber were strung vertically and used to detect X position(X view) and downstream sense wire planes were for the detection of Y position(Y view).

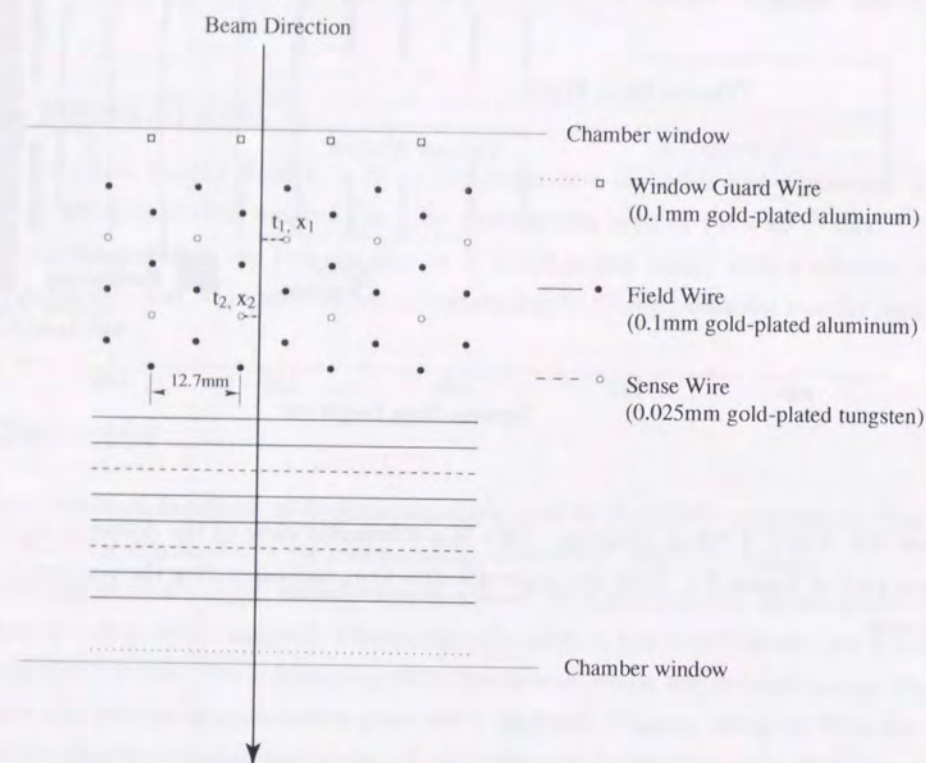


Figure 2.3: A cross section of the drift chamber. This is a look-down view of the drift chamber. The wires oriented vertically in the front were used for the X position measurement, and the rear part strung horizontally was for the Y position measurement.

The sense wires were 0.025 mm thick gold-plated tungsten and the field wires were 0.1 mm ϕ gold-plated aluminum. The field shaping wires were arranged in a hexagonal pattern around each sense wire and formed a hexagonal drift cell. The window guard wires were also 0.1 mm gold-plated aluminum, to maintain the field shape at the edge of drift cells. The sense wires in each sense plane were strung with a spacing of 12.7 mm (a half inch), and the adjacent sense planes were staggered by 6.35 mm with respect to the sense wire positions. This offset allowed us to resolve the left-right ambiguity of a particle.

The chambers were filled with Argon/Ethane gas mixture. The gas was a 49.75% Argon, 49.75% Ethane and 0.5% isopropyl alcohol mixture in the winter run, and proportion of isopropyl alcohol was raised to 1 % in the summer run for additional quenching. Alcohol in the gas absorbed

damaging ultraviolet light at the signal amplification around the wire. With typical operating high voltage of negative 2450 V – 2600 V on the cathodes and window wires, the drift velocity in each chamber was approximately $50 \mu\text{m}/\text{ns}$.

Pulses from the sense wires were amplified and discriminated by preamplifier cards mounted on the chamber. The discriminated signal was fed into LRS 3377 time to digital converters (TDCs) operated in a common stop mode, that is, the incoming signal from the sense wire started the TDC counting and all running TDCs were stopped by a common signal from a fast trigger (actually, Level 1 trigger explained later). The TDC time distribution is shown in Figure 2.4. The in-time window was defined as $115 \text{ ns} < t < 350 \text{ ns}$.

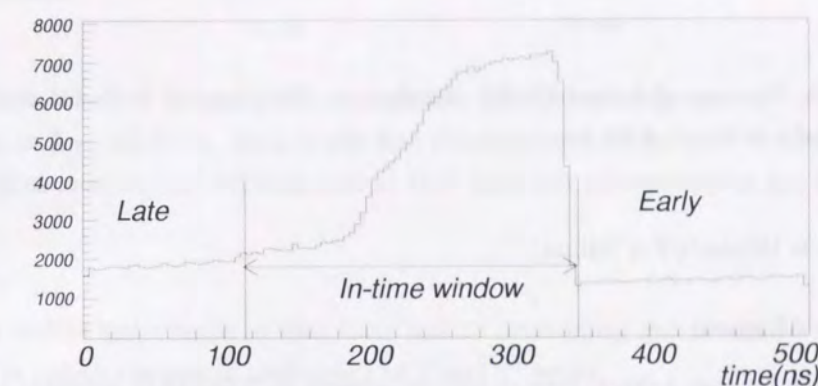


Figure 2.4: TDC time distribution of drift chamber. The in-time window was defined as $115 \text{ ns} < t < 350 \text{ ns}$. The sharp edge at 350 ns was short drift time near the sense wire. The tail at 200 ns or less, which corresponded to a longer drift time, was due to hits very far from the sense wire and non-uniformity of the electric field. The slope between 200 ns and 270 ns shows non-linearity of the drift velocity far from the sense wire.

The sharp edge at 350 ns corresponds to a short drift time near the sense wire. The tail at 200 ns or less, which corresponded to a longer drift time, was due to hits very far from the sense wire and non-uniformity of the electric field. The slope between 200 ns and 270 ns shows non-linearity of the drift velocity far from the sense wire.

The drift times were converted to drift distances and then to the position of the track at the chamber. For a hit pair of a proper single track, the sum of distances (SOD) of adjacent sense wires as seen $x_1 + x_2$ in Figure 2.3, can be determined and it must be equal to the offset of adjacent sense wires, 6.35 mm.

The SOD distribution is shown in Figure 2.5. There is a clear peak at 6.35 mm. The width of the distribution, considered as a combined position resolution of two sense planes, was $150 \mu\text{m}$ assuming Gaussian distribution. It implies that the individual position resolution of the drift

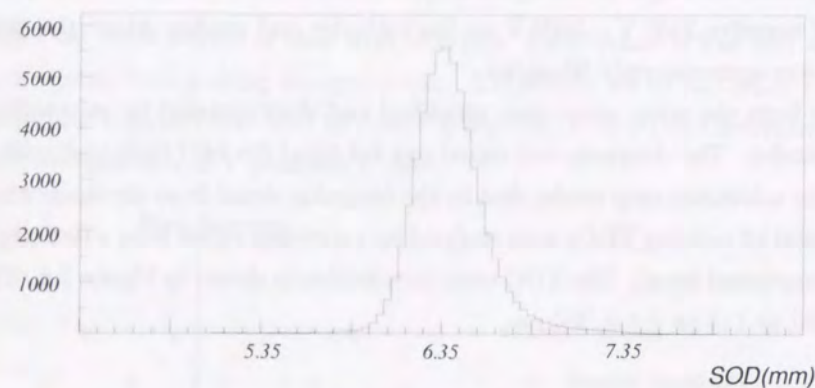


Figure 2.5: The sum of distance(SOD) distribution. The mean of SOD distribution corresponded to a half of a drift cell, 6.35 mm.

chambers is $150\mu\text{m}/\sqrt{2} \simeq 100\mu\text{m}$.

Analysis Magnet

The analysis magnet, a dipole magnet located between DC2 and DC3, provided a vertical magnetic field. The strength of the magnet field was about 2000 gauss over an aperture of about 2 meters. This gave a transverse momentum kick in horizontal direction of 205 MeV/c to charged particles.

Momentum Resolution

The momentum resolution of the KTeV spectrometer was measured to be a quadratic sum,

$$\frac{\sigma_p}{p} = 0.016\% \times p \oplus 0.38\%, \quad (2.1)$$

where p is the momentum of a charged particle in GeV/c and σ_p is its deviation. The constant term was due to the multiple scattering. The term linear in momentum is due to the finite position resolutions of the drift chambers, whose contribution becomes larger for tracks with smaller bending angle.

2.2.2 Trigger hodoscopes

Two planes of scintillator hodoscopes named V(upstream) and V'(downstream) were used at the trigger level to select events with charged particles. The V hodoscope was located at $Z = 183.90$ m while V' was located at $Z = 183.95$ m. Both banks had dimensions of $1.9\text{ m} \times 1.9\text{ m}$ and 1.0 cm thick. As shown in Figure 2.6, the scintillators were installed vertically and covered the fiducial region. Beam holes were cut to reduce the beam interaction. The scintillation counters irregularly

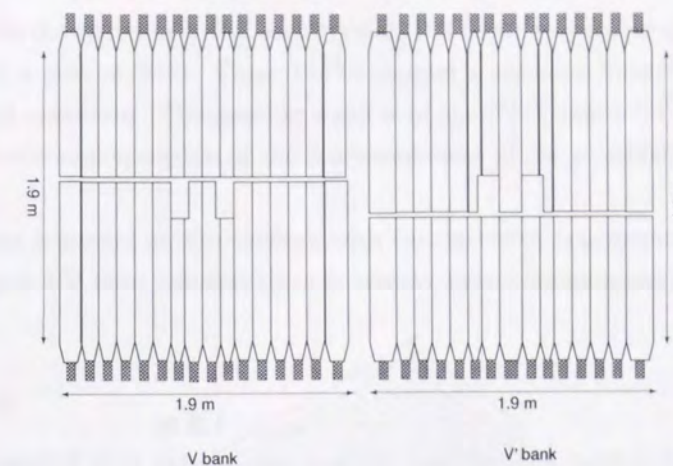


Figure 2.6: The V and V' trigger hodoscope planes. The V hodoscope located at $Z = 183.90$ m while V' was at $Z = 183.95$ m. Both banks had dimensions of $1.9\text{ m} \times 1.9\text{ m}$ and 1.0 cm thick. The scintillation counters had different sizes so that there was no overlapping gap between V and V' bank.

had different widths and lengths so that there was no overlapping gap between V and V' banks. This helped to reduce the overall inefficiency of V and V' banks.

2.2.3 Electromagnetic Calorimeter

The KTeV CsI electromagnetic calorimeter primarily provided a precision energy measurement of electromagnetic particles, e^\pm and γ . In addition, the information of the relation between a particle momentum and deposit energy in the calorimeter was used to identify electrons from pions.

The electromagnetic calorimeter was constructed of 3100 pure cesium iodide(CsI) crystals and located at 186m from the target. The dimension of the calorimeter was $1.9\text{ m} \times 1.9\text{ m}$ transverse to the beams.

CsI Crystals

The calorimeter was stacked with 2232 small CsI crystals($2.5 \times 2.5 \times 50.0\text{ cm}$) for the inner part and 868 large CsI crystals($5.0 \times 5.0 \times 50.0\text{ cm}$) for the outer part, as shown in Figure 2.7. The depth of the crystals corresponded to 27 radiation lengths, to capture photon and electron showers completely. The depth of crystals was also 1.4 nuclear interaction lengths so that most of hadrons such as charged pions passed the calorimeter as minimum ionizing particles but some made a hadronic shower in the calorimeter.

Each crystal was individually wrapped with $13\mu\text{m}$ -thick aluminized mylar and black mylar to tune the response uniformity to the level of 5%.

The scintillation light from the CsI crystal was conducted to photomultiplier tubes(PMT)

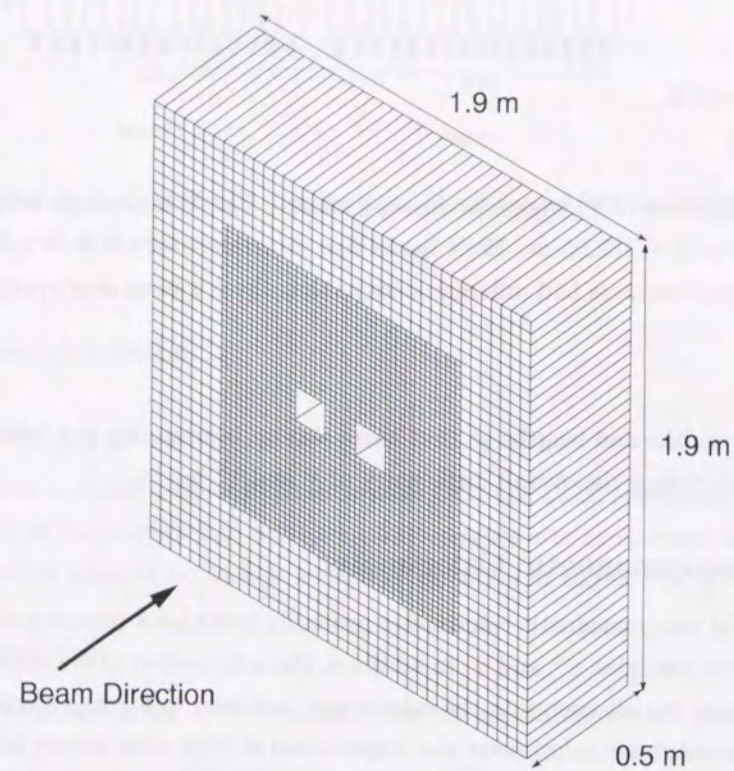


Figure 2.7: The KTeV electromagnetic calorimeter. The calorimeter had dimensions of 1.9 m(W) \times 1.9 m(H) \times 0.5 m(D) and located at 158m from the target. The calorimeter was constructed from 3100 blocks of pure cesium iodide(CsI) crystals which were 2232 small CsI crystals($2.5 \times 2.5 \times 50.0$ cm) for the inner part and 868 large CsI crystals($5.0 \times 5.0 \times 50.0$ cm) for the outer part.

instrumented on the downstream end of each crystal. PMTs were operated at -1200V high voltage typically, resulting a gain of 5000. These PMTs showed a response linearity within the level of 0.5% at the typical operation. The opening window of the PMT was a UV transmitting glass to accommodate the emission spectrum of the fast component of the scintillation light from the CsI crystal.

The PMTs were mounted on the crystals with two layers of transparent RTV rubber filters, and 1 mm-thick glass UV filter between them to remove slower components of the CsI scintillation light.

Readout System

A digital PMT base(DPMT) system was used to read out the signals from the PMTs. One DPMT card was attached just behind each CsI crystal. Since the DPMT digitized the signals right after PMT, it enabled us noise-free data collection, without transmitting analog pulses for long distance. The DPMT consisted of a high voltage divider for the PMT, a charge integrating and encoding(QIE) circuit, an 8-bit flash ADC, and a "driver-buffer-clock"(DBC) circuit[14]. The QIE and DBC devices were custom integrated circuits designed for this calorimeter.

The QIE was a hybrid digital/analog circuit integrating the charge from the PMT anode signal. To achieve both wide sensitivity range and sufficient precision, the QIE, with the help of the flash ADC, encoded the charge into an exponential form, i.e., 8 bits for the mantissa and 4 bits for the exponent.

Each QIE had four identical circuits and used them in a round-robin manner. Since the circuit was synchronized to the Tevatron RF and the operation was completed in one clock cycle, each period of the charge integration was about 19 nsec, referred as a "slice." This feature allowed non-deadtime readout. The output of the QIE was the analog signal and sent to the flash ADC for digitization.

Performance

Figure 2.8 shows a E/p distribution for electrons in K_{e3} events, where E means a deposit energy in the CsI calorimeter and p means the electron momentum measured with the spectrometer. The intrinsic energy resolution of the calorimeter is shown in Figure 2.9 as a function of the momentum. This can be roughly parameterized as a quadratic sum;

$$\frac{\sigma_E}{E} = 0.45\% \oplus \frac{2\%}{\sqrt{E(\text{GeV})}}. \quad (2.2)$$

2.2.4 Photon Vetoes

In order to detect escaping photons and electrons away from the detector sensitive region, such as the drift chambers and CsI calorimeter, ten photon veto counters were placed transverse to the beam. They kept hermeticity for the decay products.

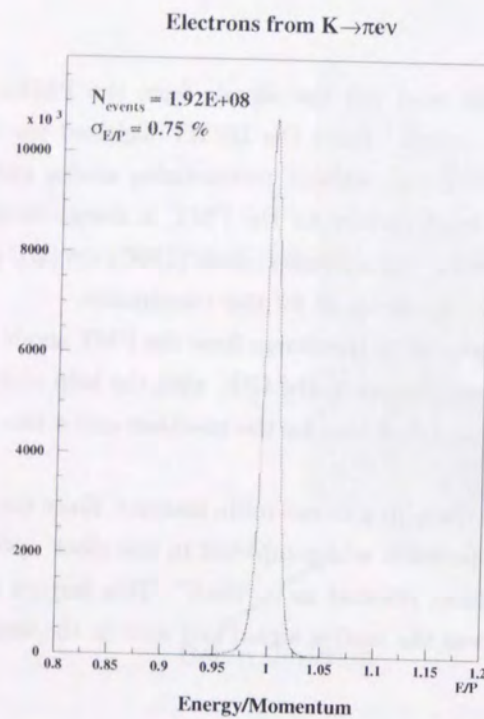


Figure 2.8: E/p for electrons in K_{e3} decays, where E means an energy deposit in the calorimeter, and p denotes a momentum measured by the spectrometer.

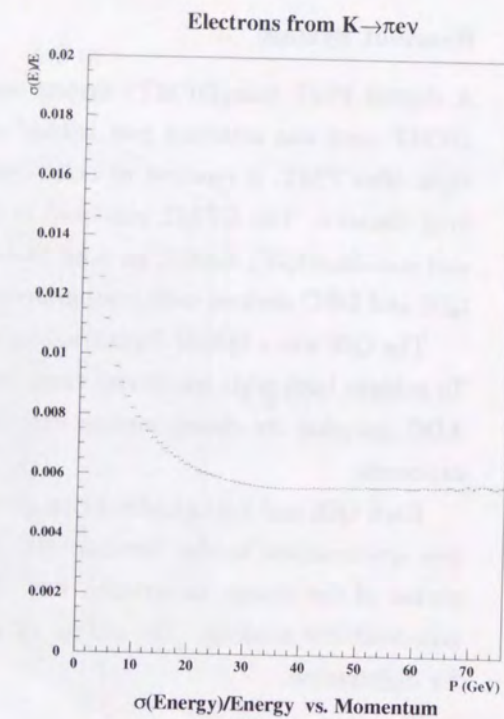


Figure 2.9: The calorimeter intrinsic energy resolution measured in K_{e3} events as a function of electron momentum.

Table 2.2: Positions and dimensions of the photon vetoes.

Elements	Z position(m)	Aperture(m)	Outer Dimension(m)
RC6	132.596	0.84×0.84	1.00 (radius)
RC7	138.598	0.84×0.84	1.00 (radius)
RC8	146.598	1.18×1.18	1.44 (radius)
RC9	152.600	1.18×1.18	1.44 (radius)
RC10	158.599	1.18×1.18	1.44 (radius)
SA2	165.116	1.540×1.366	2.500×2.500
SA3	173.985	1.692×1.600	3.000×2.400
SA4	180.018	1.754×1.754	2.372×2.372
CIA	185.191	1.842×1.842	2.200×2.200
CA	185.913	0.150×0.150	0.180×0.180

Ring counters(RC6-RC10) were located inside the vacuum pipe. These had a rounded outer shape to fit the vacuum pipe and square apertures, and were azimuthally divided into 16 modules. Each of them consisted of 24 scintillator-lead layers and approximately corresponded to 16 radiation lengths.

There were three "Spectrometer Anti"(SA2-SA4) surrounding DC2-4, respectively. The "Cesium Iodide Anti"(CIA) was also placed just upstream of the CsI calorimeter. These counters were rectangular in both the inner aperture and the outer shape. The amount of the material of them corresponded to 16 radiation lengths.

The Collar Anti(CA) was a veto counter which defined a fiducial area at the beam holes of the CsI calorimeter. It consisted of the three layers of counters and 2.9 radiation lengths of tungsten, and located in front of the calorimeter.

2.2.5 Hadron/Muon vetoes

At the downstream of the calorimeter, there were detector components to veto hadrons, muons and particles through beam holes of the calorimeter. The dimensions and the Z positions of these detectors are shown in Table 2.3.

Hadron Anti

A 15 cm thick lead wall was located $Z = 188.5\text{m}$, just downstream of the CsI calorimeter, to cut off the small electromagnetic shower leakage from the calorimeter and to produce hadron showers. A scintillator bank called "Hadron Anti"(HA) followed the lead wall, to veto events including hadrons. There was a hole in the beam region of HA and the lead wall, to let neutral beams pass through without interaction.

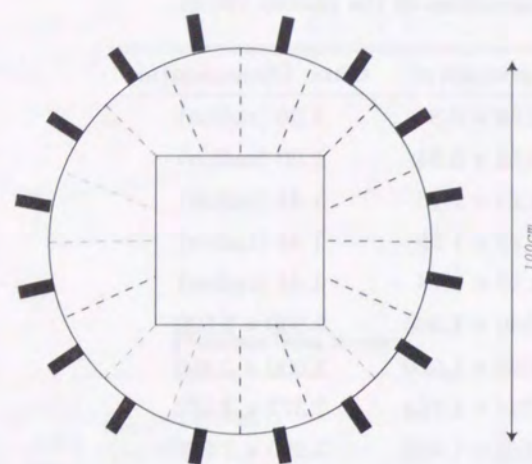


Figure 2.10: The schematic view of RC6, facing downstream. The beam passed through the inner aperture. The perimeter of outer circle fit right with the vacuum pipe. The other RCs were basically similar in a form but the dimensions seen in Table 2.2.

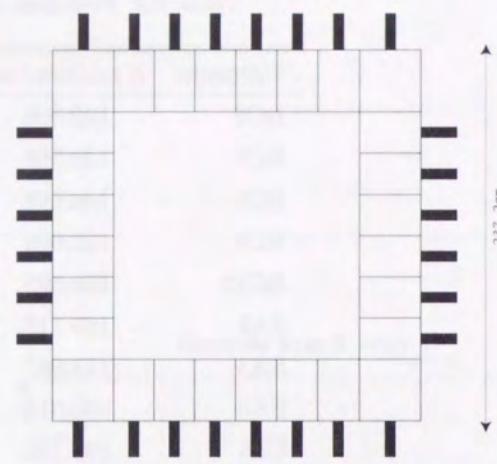


Figure 2.11: SA4 from upstream.

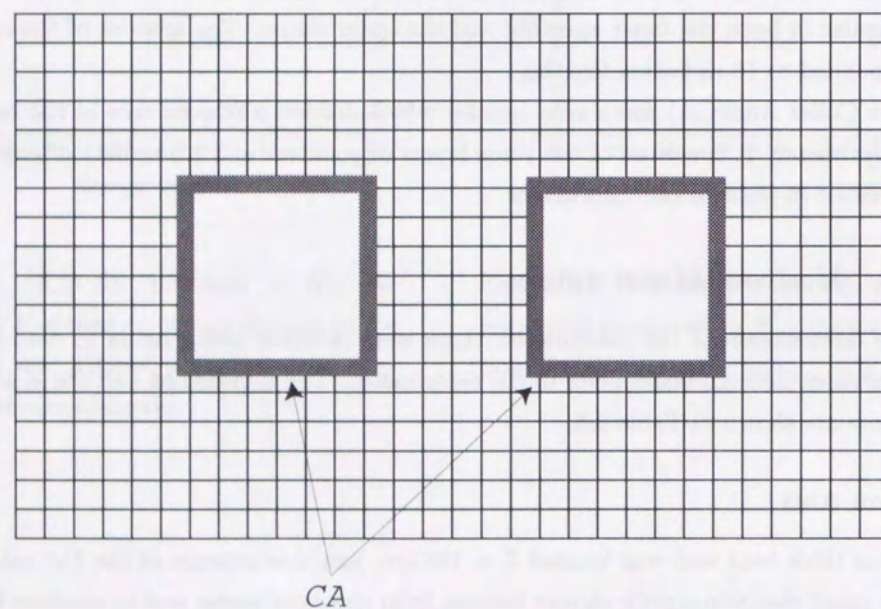


Figure 2.12: The Collar Anti just in front of the calorimeter.

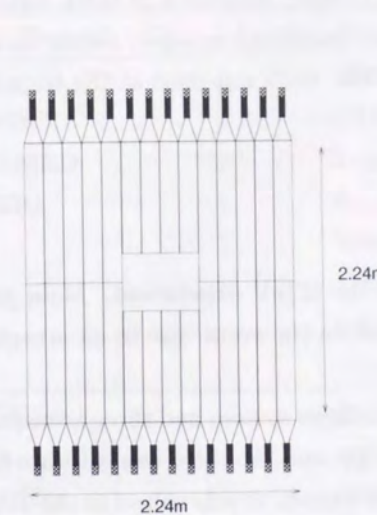


Figure 2.13: The HA hodoscope, which was composed of the same size of 28 scintillation counters. This followed the lead wall and detects hadronic particles.

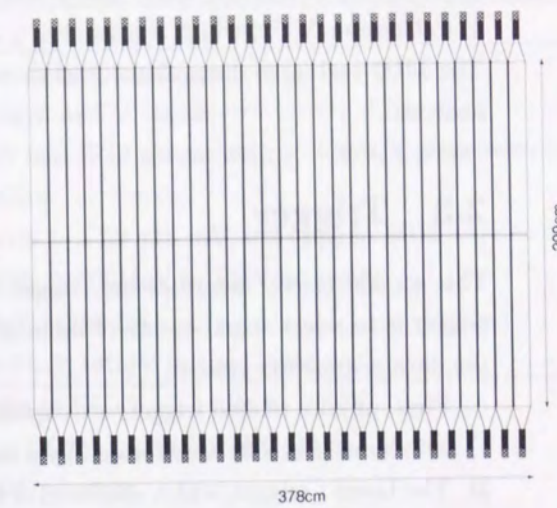


Figure 2.14: The Mu2 counter.

Table 2.3: Positions and dimensions of the detectors(downstream of the calorimeter).

Elements	Z position(m)	Dimensions(m)
Lead wall	188.53(0.15m thick)	2.43×2.43
HA	188.97	2.24×2.24
Steal 1	189.09(1m thick)	2.4×2.4
BA	191.09	0.60×0.30
Steal 2	191.74(3m thick)	4.3×3.4
MU2	194.83	3.93×2.99
Steal 3	195.29(1m thick)	3.5×3.6
MU3	196.36	3.00×3.00

Muon Counter

Downstream of the HA, there was a stack of steel totaling roughly 5 m-thick followed by Muon Veto Counter(MU2) which consisted of a scintillation hodoscope to reject events including muons. The MU2 had large dimensions, $2.99 \text{ m} \times 3.78 \text{ m}$. The MU2 was used at the trigger level in this analysis.

2.3 Trigger

This section briefly describes the trigger system in the KTeV experiment. Main purpose of the trigger is to select signal events of interest and to reduce the event rate to an acceptable level for the data acquisition system.

First, physics related triggers are explained. This trigger system had three levels; the first(Level 1) and second(Level 2) were formed by a hardware logic, and the third was software filtering(Level 3). The Level 1 trigger, which consisted of fast trigger sources, synchronized to the Tevatron RF(53 MHz) and provided a deadtimeless trigger. The Level 2 performed time consuming decisions such as counting the number of hits in DCs, and the number of photons in the calorimeter. The Level 3 trigger carried out complex event reconstructions including charged track trajectories, energy clusters in the calorimeter, and simple vertex finding. The Level 3 filtering is explained in Section 2.4, as a part of the data acquisition system. The trigger for the signal basically required the existence of four charged tracks and allowed some additional particles such as photons.

In addition, calibration triggers were used to collect events necessary for the CsI calibration and pedestal measurements.

2.3.1 Level 1 Trigger

In about 20 seconds of Tevatron spill, the primary proton beam and the secondary K_L beam arrived with a microstructure, called a bucket, $1 \sim 2 \text{ nsec}$ beam pulse once every 19 nsec. The Level 1 trigger, based on fast trigger sources such as photomultiplier signals, was synchronized to the microstructure and allowed deadtimeless triggering.

There were 80 Level 1 trigger sources in total which were made with NIM logic. Table 2.4 shows major Level 1 trigger sources used to take data for $K_L \rightarrow \pi^+\pi^-e^+e^-$ and $K_L \rightarrow \pi^+\pi^-\pi_D^0$. After resynchronizing to the Tevatron RF before triggering, the trigger sources were transferred to twelve memory lookup units and decision was made simultaneously for 16 trigger outputs for each RF clock cycle.

Next, we describe the Level 1 sources.

Table 2.4: The E799 four track trigger elements.

Trigger Element	Trigger Level	Description
GATE	1	Vetoes "fast neutrino pings"
3V_TIGHT	1	≥ 3 hits in both V and V' banks
2DC12_MED	1	3 out of 4 DC1 and DC2 planes with ≥ 2 hits, 1 plane with ≥ 1 hit
ET_THR1	1	$E_{\text{TOTAL}} \geq 11\text{GeV}$
$\overline{\text{MU2}}$	1	Veto events with ≥ 1 hit (15 mV, 0.2 mip) in MU2
$\overline{\text{PHV}}$	1	Veto events with $\geq 500\text{MeV}$ in PHV or events with $\geq 400\text{MeV}$ in the SA
$\overline{\text{CA}}$	1	Veto events with $\geq 14\text{GeV}$ in the Collar-Anti
34.HCY	2	require ≥ 3 hits in DC1Y, ≥ 3 hits in DC2Y and ≥ 4 hits in DC3Y, ≥ 4 hits in DC4Y
HCC_GE2	2	require ≥ 2 HCC clusters
YTF_UDO	2	YTF trigger: Requires a good track in the upper half and a good track in lower half or one good central track
3HC2X	2	≥ 3 hits in DC2X Bananas

Neutrino Ping

When the KTeV experiment was running, Tevatron also provided the primary proton beam to the other experiments. The "Neutrino Ping" signal was introduced to reject a fast, short-width high intensity spill for a neutrino-scattering experiment. This is because if fast high intensity beam happened to be delivered to the KTeV beam line, it could cause unacceptable high detector activity.

Trigger hodoscope

The V and V' were used to detect charged track hits. We required at least 3 hits in both the V and V' hodoscopes in this analysis.

DC-OR trigger

DC1 and DC2 were also used as a fast trigger source. Although the maximum drift time was about 200 ns, the track is always passing between two wires in two adjacent planes, so that one of the hits should arrive within 100 ns after track passing. Therefore, we could utilize the logical OR of the wires for the fast trigger source. The trigger source consisted of sets of 16 OR-ed sense wires(10.2 cm wide) and looked at the hit them in the X and Y views.

This trigger source called "DC-OR" was used to select events with charged particles passing between DCs and V and V' banks. The signal trigger required that three out of four planes had

at least 2 hits, and the rest had at least one hit.

Ettotal

An analog sum of the signals from all PMTs in the CsI calorimeter was used as a Level 1 trigger source. This approximately corresponded to total in-time energy deposit in the calorimeter. In this study, the energy deposit was required to be over 11GeV nominal.

Muon Counters

The muon counters were also used to veto events. Since both the signal and normalization modes do not include any muons, we vetoed events with any hits(0.2 mip) on the MU2 veto counter.

Photon Vetoes

Signals from the photon veto counters were also used to veto events with outgoing decay products from the fiducial volume. We vetoed if photons or electrons hit the photon vetoes and had an energy deposit of 500MeV or larger in the ring counters(RC6-10), or 400MeV or larger in the spectrometer anti(SA2-4). For the collar anti(CA), events were vetoed if particles hit CA and there was an energy deposit of over 14GeV.

2.3.2 Level 2 Trigger

The Level 2 trigger system is briefly explained here. Details can be found in Ref. [15] if one needs more explanation.

The Level 2 trigger consisted of a slower trigger logic. This allowed us to do a simple event reconstruction for further background and accidental event reduction. When an event was accepted by Level 1, the Level 2 trigger decided if the event should be accepted to be sent to the DAQ/Level 3 system, or not.

Drift Chamber Activity(Kumquat)

This trigger required hits which were identified as proper track hits in Y view of drift chambers. In this analysis, the drift chamber hit in a 205 ns gate was required in Y view for the trigger level; at least 3 hits each in DC1Y and DC2Y, and at least 4 hits each in DC3Y and DC4Y.

Hardware Cluster Counter

The hardware cluster counter [16] counted the number of in-time clusters in the CsI calorimeter. The hardware cluster was defined as a cluster consisting of crystals which had the energy deposit of 1GeV or more with a shared perimeter. Therefore, the particle associated with the hardware cluster was identified to be a electron or photon. This counting was achieved with a hard-wired

energy cluster search algorithm and PMT outputs. We required at least two hardware clusters in the event.

YTF trigger

The function of Y Track Finder(YTF) [17] trigger made a simple Y track reconstruction by looking at hit-patterns in the drift chamber. For the momentum balance, we required the existence of reconstructed tracks in both upper and lower halves of chambers.

Sum of Distance Correlation(Banana)

This trigger equipment was used to require events with in-time hits in the drift chambers. The hits were assumed to be in-time if the sum of distances was in an allowed region. The time of each hit was measured with 625 MHz TDCs.

At least three proper hits in DC2-X were required in this analysis.

2.3.3 Trigger Rate

During the winter run, the beam intensity was about 4×10^{12} protons per spill, where the beam duration was about 19 sec. For four track trigger containing $K_L \rightarrow \pi^+ \pi^- e^+ e^-$ and $K_L \rightarrow \pi^+ \pi^- \pi_D^0$, the trigger rate was about 25 kHz for the Level 1 trigger and about 2 kHz for the Level 2 trigger(70 kHz for Level 1 and 7 kHz for Level 2 of total trigger rate). The DAQ live time was typically 60–70%, depending on the beam rate and instantaneous beam intensity.

2.3.4 Calibration Trigger

The calibration trigger involved the following: laser calibration of the CsI calorimeter; pedestal measurements in all the detectors; uniformity measurements of the CsI by using cosmic muons. They were generated from local logic circuits.

The trigger of laser calibration was formed by a flash of laser/dye system(5 Hz on- and off-spill).

The pedestal was collected by opening ADC gates intentionally both on-spill and off-spill at the rate of 3 Hz.

There were additional muon telescopes located at the top and bottom of the CsI blockhouse for triggering and positioning the cosmic muon event. The rate of this trigger was about 30 Hz, and it was taken during off-spill only. These events were used to measure the CsI uniformity in response along the Z direction.

2.4 Data Acquisition System

After performing event selection at the L1/L2 triggers, data were sent to KTeV data acquisition system(DAQ). In the KTeV experiment, the event rate after the Level 2 trigger was approximately

11 KHz and the average event size was 8 KBytes nominal, equal to about 2 GBytes per spill($\sim 11\text{KHz} \times 8\text{KBytes} \times 20\text{sec/spill}$). The system was designed to handle twice this level of bandwidth.

Here, we glance over the DAQ and Level 3 filtering. More details are found in Ref. [18, 19].

2.4.1 Frontend and DAQ

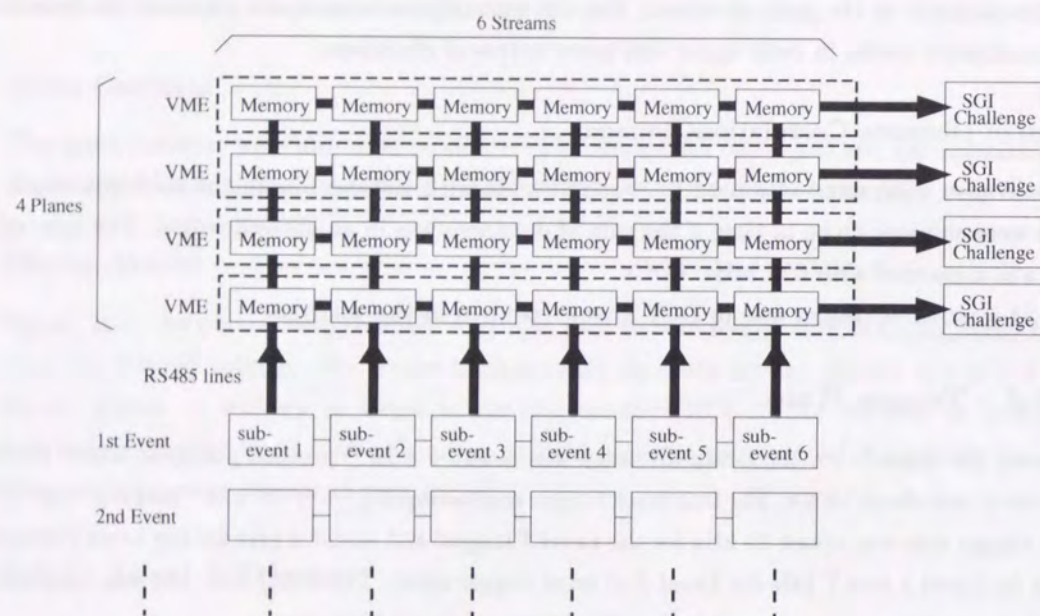


Figure 2.15: Data acquisition system. Three planes were used for Level 3 trigger and the other was for online monitoring of the detector performance and online calibration.

In Figure 2.15, the basic structure of the DAQ is drawn. An event, which consisted of six subevents at the frontend, was asynchronously read out through a fast data bus. The data was then sent to buffer memories(streams) through six RS485 lines, whose bandwidth was 40Mbytes/sec/line each. The buffer memory had a capacity of 4GB, large enough to store all the events collected over a spill, approximately 2GB.

Each stream formed "plane", which was logically connected to a Unix workstation(SGI Challenge). The Unix work stations performed the event reconstruction for the filtering and monitoring: Three of four planes were used for the Level 3 filtering, and the other was used for monitoring of the detector response and online calibration.

2.4.2 Level 3 filtering

The level 3 filtering provided a simple event reconstruction with a software filtering on SGI Challenges. This allowed us to reduce the trigger rate based on the information from sets of detector elements such as charged track and vertex reconstruction, particle identification with calorimeter E/p, and muon counter hits.

The Level 3 filter for our study required three reconstructed tracks shared a vertex which located from 90.0 to 158.0 meters from the target.

2.5 Physics Run

This section describes the data collected in the KTeV-E799II runs, which was used for physics analysis of $K_L \rightarrow \pi^+\pi^-e^+e^-$ and $K_L \rightarrow \pi^+\pi^-\pi_D^0$.

The data used in this measurement consisted of two runs of KTeV-E799II experiment, winter run and summer run. The winter run was performed between February 1 and March 23, 1997, run 8245 through 8910. The summer run was between July 24 and September 3, 1997, run 10463 through 10970.

There were some differences between the winter and the summer runs, as shown in Table 2.5. The main difference between them was the proton beam intensity and neutral beam size. The proton beam intensity was lowered during the summer run due to the sharing of the proton beam in the Tevatron with other experiments. To keep appropriate kaon beam intensity, the larger neutral beams were used in the summer run to compensate for the decreased intensity of the primary proton beam.

Table 2.5: The KTeV-E799II run conditions.

	Winter Run	Summer Run
Run Number	8245-8910	10463-10970
Proton Intensity(spill)	5.0×10^{12}	3.5×10^{12}
Beam Size at the CsI	10 cm \times 10 cm	12 cm \times 12 cm
4 Track L1 Trigger Rates	20 KHz	23 KHz
4 Track L2 Trigger Rates	1.5 KHz	2.3 KHz

The collected data were written to about 500 Digital Linear Tapes(DLT) at the experiment. Each DLT stored about 10GB of data. Since they included all physics triggers, we split off only 4 track tagged events into 38 DLTs for the winter and 44 DLTs for the summer runs. Furthermore, the data of 82 4 track triggered tapes were processed in a step. This separated and filtered the 4 track triggered events into datasets which were used for a different analysis. The filtering was performed with offline event reconstruction code. This stage reduced the total data size to 17 DLTs. In our analysis, we analyzed events based on this data set.

Chapter 3

Monte Carlo Simulation

In each phase of this analysis, such as the acceptance calculation in both the signal and the normalization mode, the background estimation, and the systematic study, we strongly relied on the Monte Carlo simulation(MC) to understand the detector performance and particle decays' kinematics. In the Monte Carlo simulation, we simulated the beam production, particle decays, detector response, signal digitization and the triggering. Since output data format from the Monte Carlo simulation was the same as that from the real KTeV detector, we could analyze real data and the Monte Carlo events with the same event reconstruction algorithm and to make detailed, synthetic study on both of them.

The Monte Carlo simulation was processed in five stages: Kaon beam production, decay generation, tracing in the detector, signal digitization, and trigger. We will glance them in this chapter.

3.1 Kaon production

The neutral kaons were produced in the target, based on the measured beam position and width. In the generation, we used a parameterization by Malensek [7] for the momentum spectrum of K^+ and K^- produced by protons incident onto a beryllium target. In the parameterization, the number of kaons with momentum p into a solid angle $d\Omega$ at a polar angle θ was proportional to:

$$\frac{d^2N}{dpd\Omega} = \frac{B}{400} \cdot x \cdot \frac{(1-x)^A(1+5e^{-Dx})}{(1+p_t^2/M^2)^4}, \quad (3.1)$$

where p is the produced particle momentum and E_B is the beam energy, $x = p/E_B$, and p_t represents the transverse momentum of the produced particle relative to the incident beam direction. The B, A, D , and M^2 were determined from the experimental data obtained by 400 GeV/c proton beam, and their values are shown in Table 3.1.

The production spectrum for the neutral kaon can be derived from that for charged kaons. Let us define σ_u, σ_d , and σ_s , as the production probabilities of $u\bar{u}$, $d\bar{d}$ and $s\bar{s}$ quark pairs, respectively, and let us assume $\sigma_u = \sigma_d$. The production of a K^+ needs the creation of a $s\bar{s}$. In this case,

Table 3.1: The parameters referred from Malensek [7]

	K^+	K^-
A	2.924	6.107
B	14.15	12.33
M^2	1.164	1.098
D	19.89	17.78

since one of the two valence u quarks in the proton beam couples to the s quark, the production probability of K^+ is proportional to $2\sigma_s$. We can also consider another case, where a u quark is taken from the sea whose probability is proportional to $\sigma_s\sigma_u$. Similarly,

$$\sigma(K^+) \sim 2\sigma_s + \sigma_s\sigma_u \quad (3.2)$$

$$\sigma(K^-) \sim \sigma_s\sigma_u \quad (3.3)$$

$$\sigma(K^0) \sim \sigma_s + \sigma_s\sigma_u = \frac{\sigma(K^+) + \sigma(K^-)}{2} \quad (3.4)$$

$$\sigma(\bar{K}^0) \sim \sigma_s\sigma_u = \sigma(K^-). \quad (3.5)$$

This provides an approximation of the K^0 and \bar{K}^0 production spectra. The spectrum was tuned further to match kaon momentum measured by $K_{L,S} \rightarrow \pi^+\pi^-$ events in the data. The correction factor, $\xi(p)$ was

$$\xi(p) = 1 + 10.655x - 55.337x^2 + 60.033x^3, \quad (3.6)$$

where $x = p(\text{GeV}/c)/1000$. This was multiplied as a factor of the generation probability:

$$\frac{d^2N}{dpd\Omega}(K^0) = \frac{1}{2}[\frac{d^2N}{dpd\Omega}(K^+) + \frac{d^2N}{dpd\Omega}(K^-)] \times \xi(p), \quad \frac{d^2N}{dpd\Omega}(\bar{K}^0) = \frac{d^2N}{dpd\Omega}(K^-) \times \xi(p). \quad (3.7)$$

Both K^0 and \bar{K}^0 were produced according to Equation 3.7 in our Monte Carlo simulation. Figure 3.1 shows the momentum spectrum of generated kaons.

After the production of a K^0 or \bar{K}^0 , it was propagated to a decay point in the vacuum volume of the detector by taking into account the full amplitude evolution. The decay position was chosen based on its lifetime and momentum. The distribution of the decay position of K_L s is shown in Figure 3.2.

3.2 The Decays

After the decay position was determined, the Monte Carlo simulation generated decay products of K_L . Here, we briefly explain the decay processes used in the Monte Carlo simulation.

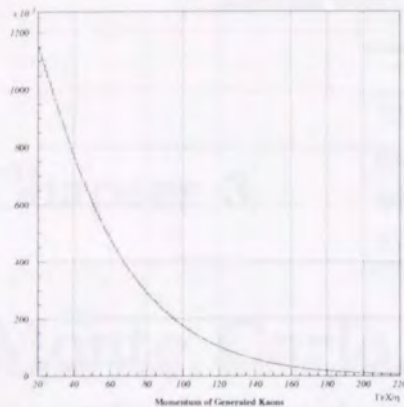


Figure 3.1: Momentum distribution of generated kaons at the target.

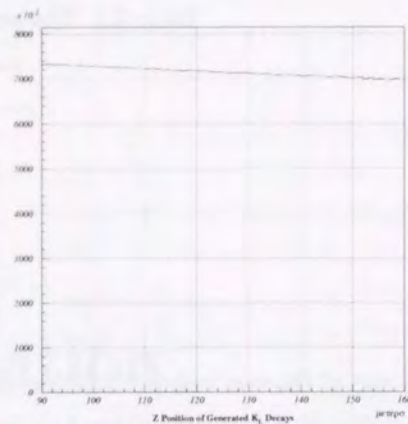


Figure 3.2: K_L decay Z-distribution of Monte Carlo generated kaons.

3.2.1 $K_L \rightarrow \pi^+\pi^-e^+e^-$

The matrix element to generate the decay $K_L \rightarrow \pi^+\pi^-e^+e^-$ completely relied on the equation in Ref. [22, 23], as described in Section 1.3. The direct CP violating effect, however, was eliminated since the effect on this analysis was expected to be negligible. The coefficients in the matrix element were obtained from PDG [9] and theoretical estimation from Ref. [22, 23].

In addition, we also modified the form factor in direct photon emission component $gM1$, as in the recent study [29, 37, 38],

$$gM1 \rightarrow gM1 \cdot F$$

$$F = \frac{a_1}{(M_\rho^2 - M_K^2) + 2M_K E_{\gamma^*}} + a_2, \quad (3.8)$$

where E_{γ^*} is the energy of the parent photon of the electron-positron pair in the kaon center-of-mass system, and M_ρ is the mass of the neutral ρ meson. We independently determined a_1/a_2 from the kinematics of $K_L \rightarrow \pi^+\pi^-e^+e^-$ in Chapter 6.

3.2.2 $K_L \rightarrow \pi^+\pi^-\pi^0$

The $K_L \rightarrow \pi^+\pi^-\pi^0$ decay was simulated with a pure phase space distribution. Since the π^0 flies too short ($c\tau = 25.1\text{nm}$) to trace with the KTeV detector, it immediately decayed to $\gamma\gamma$ or $e^+e^-\gamma$ in the Monte Carlo simulation.

In case of the Dalitz decay, $\pi^0 \rightarrow e^+e^-\gamma$, the generation was based on the formulation by Kroll and Wada [43], including $\mathcal{O}(\alpha_{\text{EM}}^2)$ radiative corrections by Mikaelian and Smith [44, 45], and inner bremsstrahlung corrections ($\pi^0 \rightarrow e^+e^-\gamma\gamma$) and virtual-photon corrections.

3.2.3 Particle Tracing

After a kaon decay was generated and π^0 decayed into $\gamma\gamma$ or $e^+e^-\gamma$ immediately, decay products were boosted to the lab frame and traced through the detector. Tracing was terminated if the particle decayed, interacted with materials, or went out from the detector. All decay products except π^\pm 's were stable so they were propagated without decaying. For charged pions, the proper lifetime was assumed and some of them decayed into $\mu\nu$ in flight.

3.3 Detector

Charged particles passing through the detector material could be scattered by the Coulomb multiple scattering according to a parameterization of the Molière theory [46]. This also accounted for a scattering angle distribution of a non-Gaussian tail caused by the single scattering effect. For electrons, in addition to the scattering, radiative bremsstrahlung was allowed according to the Bethe-Heitler cross-section. Radiated photons could be converted in material with probability $1 - e^{-\frac{7}{9}(X/X_0)}$, where X/X_0 is the amount of the material in radiation lengths. The energy spectrum of the converted electron-positron pair was defined by Bethe-Heitler formula, and routines in EGS4 electromagnetic shower library [47] was imported for calculating the opening angle of electron and positron pair.

Generated particles in these interactions were also traced as well as daughter particles of the decay.

When a particle escaped from the fiducial volume of the detector, defined by the outer edge of detector elements, it was not traced further, to save the processing time.

3.3.1 Photon Veto

Charged particles, except electrons, were treated as minimum ionizing particles, when they pass through photon veto counters, and an energy deposit of the incident particle was smeared with Gaussian distribution. The parameter of the energy deposit distribution was determined with calibration constants acquired from calibration runs. Minimum ionizing particles were also scattered here.

For electrons and photons, the particle was stopped when it entered a photon veto, and all of its energy was deposited in the detector after Gaussian smearing.

A trigger was vetoed if the total deposit energy of one of the counters, exceeded its threshold. The energy deposit was digitized to ADC counts based on a gain determined with calibration runs.

3.3.2 Drift Chamber

When charged particles pass through the drift chambers, the incident position was stored and the drift distance, which is the distance between the particle trajectory and the closest sense wires in the chamber plane, was calculated. A drift time was translated from the drift distance with the

calibration data, and smeared to the chamber resolution of $100\mu\text{m}$. The drift time was converted into TDC counts with certain offsets. Only the first hit on a wire in multiple hits was simulated.

The δ -ray effect which causes low-SOD pairs were simulated in the chamber gas. This was treated as multiple hits on the same cell.

3.3.3 CsI calorimeter

The CsI calorimeter was simulated for all particles entering to the front face of the calorimeter. For photons, electrons, and pions, the simulation determined the incident position and generated a shower. Muons were treated as minimum ionizing particles. After calculating deposit energy for each crystal in an event, the response of scintillation light was simulated, and its digitization was done for each crystal. The trigger component Etot and HCC were instrumented in the Monte Carlo simulation.

Electromagnetic Shower

When electrons and photons were propagated to the face of the CsI crystal, its extrapolated transverse position at the depth of the shower mean was determined. The depth was calculated with:

$$Z_e(\text{m}) = 0.11 + 0.018 \times \ln E(\text{GeV}) \quad \text{for electrons,} \quad (3.9)$$

$$Z_\gamma(\text{m}) = 0.12 + 0.018 \times \ln E(\text{GeV}) \quad \text{for photons,} \quad (3.10)$$

where E is the incident energy of electron(photon). The CsI calorimeter has 27 radiation lengths so that electron or photon showers were well-contained in the calorimeter. Therefore, tracing was terminated at the calorimeter for those particles.

With the information of the incident position and the incident energy, the energy deposit in the crystals was determined by samples(shower library) premade by GEANT simulation. Each single event in the shower library was composed of energy maps on 13×13 small($2.5\text{cm} \times 2.5\text{cm}$) crystals. The large crystal($5.0\text{cm} \times 5.0\text{cm}$) was simulated as four small crystals.

The events in the library were classified into bins according to the incident energy, 2, 4, 8, 16, 32, and 64 GeV. In addition, the incident position of the face of the CsI crystal were binned into 50×50 bins, to simulate the position resolution at sub-millimeters with reconstructing an energy cluster.

The energy deposit were segmented longitudinally into 25 slices to simulate the light output from a crystal with nonuniform behavior. The uniformity was calibrated for each crystal with radioactive source in advance, and cosmic muons during runtime.

Hadronic Shower

The hadronic shower in the CsI calorimeter was also simulated in the Monte Carlo. This is because the shower shape and the energy deposit in the CsI calorimeter are used to distinguish

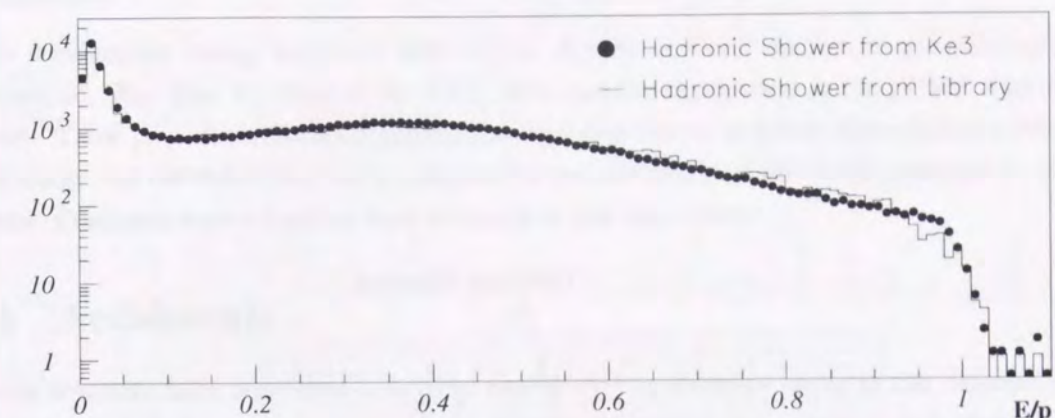


Figure 3.3: E/p distribution of pion shower samples(actual data from K_{e3} and Monte Carlo simulation from hadronic shower library).

electrons from pions in the analyses, and satellite clusters of the hadronic shower can mimic photon clusters(Figure 3.4).

In order to avoid time consuming event by event shower simulation, a large sample of hadronic showers was first produced and stored in a library to be used later in the Monte Carlo event generation. The shower library for the KTeV detector simulation was generated using GEANT 3.21 with FLUKA for the hadronic interactions. In the generation, a pion was used as an incident particle and cut off energy in the CsI was 0.001 GeV for hadronic and electromagnetic interactions.

Pions were injected uniformly on the surface, and its incident position was binned into 0.25 cm by 0.25 cm square regions. The incident energy is also divided into 12 bins from 2 GeV to 64 GeV in the library. Each event in the library had energy deposit in 13 by 13 array of 2.50 cm crystals, and in the hadron anti counters. The crystals were segmented along beam axis into 25 slices to obtain the energy cluster information in depth. The energy deposit in each slice was stored in the library.

When generating events in the Monte Carlo simulation, if a pion hits the CsI, a shower sample from an appropriate incident energy and position bin is selected randomly from the shower library. The energy deposits in each slice in depth are scaled to the energy of the incident particle and convoluted with measured CsI scintillation response to calculate the total charge from PMTs.

As shown in Figure 3.3, E/p distribution of the Monte Carlo simulation with the shower library is consistent with that of actual hadron showers from K_{e3} decay.

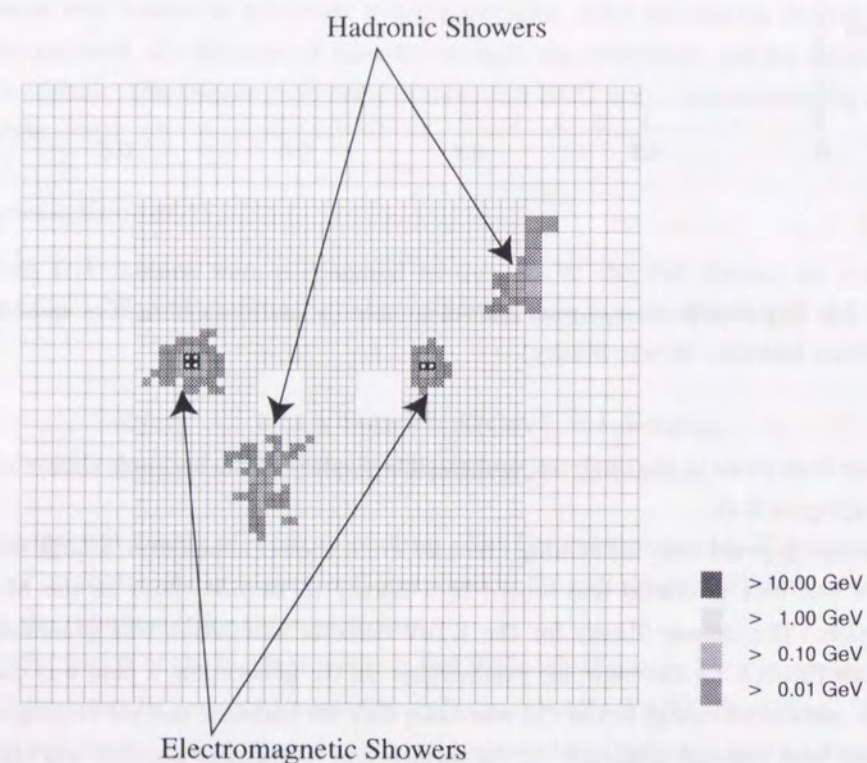


Figure 3.4: Electromagnetic and hadronic shower shape comparison in the Monte Carlo. The electromagnetic shower forms round while the hadronic shower has an irregular shape.

For muons, the deposit energy in the CsI crystals was calculated as a minimum ionizing particle.

Digitization

After deciding the energy deposit in each crystal, the Monte Carlo simulation proceeded to the digitization. The time structure of the PMT pulse and the digitization at the DPMT were simulated. These procedures included appropriate smearing due to simulate photostatistics effects. The energy was converted into charge assigned to each DPMT time slice with constants for each crystal. Constants were calculated from electrons in real K_{e3} events.

3.4 Accidentals

Actual detectors have accidental activities, caused by the electronic noise in the detector and contaminations in the neutral beam, mostly neutrons scattering or interacting with materials of the detector. This section describes how the accidental activities were simulated.

3.4.1 Accidental Effect

The accidental activity faked hits on the detectors. For $K_L \rightarrow \pi^+\pi^-\pi^+\pi^-$ study, there were two major effects on the analysis. First, a signal acceptance decreased with accidental hits. This is because accidental hits on the photon veto and muon veto counters could fire the vetoes. This effect was also found in the event selection in the analysis. Second, the accidental activities contributed to the misreconstruction of the events. This effect mainly increased the background level. Therefore, accidental activities should be simulated in the Monte Carlo simulation.

3.4.2 Accidental Overlay

While the Monte Carlo simulation cannot reproduce such activities precisely, these accidental activities are independent of the kaon decay in nature. Therefore, the Monte Carlo simulated the accidental activity by overlaying accidental hits collected from the actual run. The accidental trigger served for this purpose. This trigger was a random trigger, whose rate was proportional to the instantaneous proton rate. The accidental trigger was taken during the experiment.

After the event generation in usual manner on the Monte Carlo, the accidental overlay was performed at the digitization: ADC counts from accidental hits were simply added to the Monte Carlo simulation. The latch hits of detectors were OR-ed, and the earliest TDC hit was kept. Trigger requirements were then tested for each component again.

Chapter 4

Event Reconstruction

In $K_L \rightarrow \pi^+\pi^-\pi^+\pi^-$ analysis, it is important to find charged tracks, the decay vertex of K_L , and to identify the particles. Event reconstruction, which gives these information, was done by a combination of track finding with the spectrometer and the CsI calorimeter. In this chapter, we describe how events were reconstructed in the analysis.

The details in the reconstruction procedure are described in the following sections. The event reconstruction sequence is:

- Finding candidates of tracks from the drift chamber hits.
- Energy cluster finding on the CsI calorimeter.
- Track reconstruction with the information of the track candidates and the energy clusters.
- Vertex finding.
- Particle identification with the track momentum and cluster energy.

4.1 Track Candidate Finding

Track candidates were reconstructed with chamber hits in this phase [48]. Since tracks were bent at the analysis magnet in X(horizontal) view but not in Y(vertical) view, tracks were reconstructed in X and Y view separately.

4.1.1 Hit Pairing

First, hit pairs in each plane of the drift chambers were searched for in X and Y planes independently. A hit pair was defined as a hit on a sense wire and a neighboring hit in the adjacent plane.

The hit pairs were classified for their quality. Figure 4.1 shows possible cases. The “good SOD” pair was defined as the SOD close to a half the drift cell size, $|SOD - 6.35\text{mm}| < 1.0\text{mm}$. The

“low SOD” pair having SOD less than 6.35 mm was also accepted since a hit pair with low SOD generally occurred when two or more tracks happened to pass through a cell. A “high SOD” pair was discarded in this analysis. Because the drift chambers had a small intrinsic inefficiency, it is also necessary to identify an “isolated hit” without a neighboring hit, to use them to form a track candidate.

In order to evaluate the quality of the reconstructed track later, a number called “pair value” was assigned to the good-SOD, low-SOD and isolated hit pair as 4, 2, and 1, respectively.

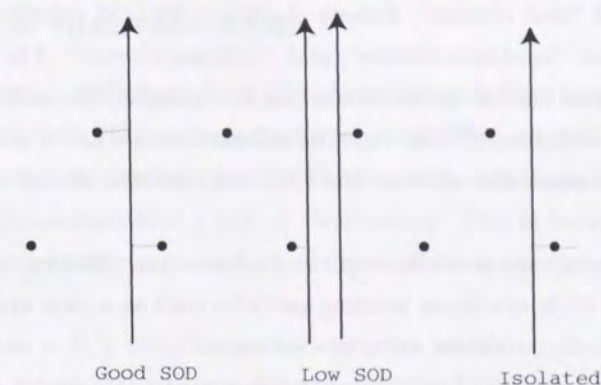


Figure 4.1: Schematic view of the classification of hit pairs. Dots indicate the sense wires. The solid arrow means the trajectory of a charged particle, and a hair line between a trajectory and a sense wire shows drift distance reconstructed from TDC counts. A good SOD pair could define a trajectory while an isolated hit had a two-way ambiguity. The evaluation value called “pair value” was assigned to these hit pairs as 4, 2, and 1, respectively.

4.1.2 Finding Y track candidates

After hit pairs were found, Y track candidates were searched for by picking a hit pair in DC1 and DC4 each, and interpolating them with a straight line. If hit pairs in both DC2 and DC3 lied within 1 cm from this line, those hit pairs were fitted for a straight line and the χ^2 was calculated. In addition, the sum of the pair values was required to be at least 11, to select good track candidates.

4.1.3 Finding X track candidates

The X track had a kink at the magnet placed in the middle of the spectrometer. For this reason, X tracks were reconstructed in upstream and downstream segments of the spectrometer, separately. The pair value was also required as greater than 3 in both upstream and downstream X track reconstruction.

The upstream and downstream track segments were then extrapolated to the center of the analysis magnet at $Z = 170$ m. If the distance between the two track segments was less than 0.6

cm, and the sum of the pair values of both segments was 11 or more, they formed an X track candidate.

4.2 Cluster Finding

In the CsI calorimeter, the cluster energy was defined as a sum of energy deposits in a 7×7 array of small crystals or 3×3 array of large crystals centered on a crystal with the local maximum deposit energy, which is called "seed crystal." Energy clusters in the CsI calorimeter were classified into two different categories; "hardware cluster", and "software cluster." The only difference was the determination of the seed crystal in the cluster. In this analysis, the hardware cluster was formed around a seed crystal with the HCC bit on. The software cluster had a seed crystal with a deposit energy of 100 MeV or more and without the HCC bit, and the cluster energy was 250 MeV or more.

Therefore, electromagnetic particles such as a photon and electron must be associated with the hardware clusters while minimum ionizing particles such as a pion and muon, which typically deposited 350 MeV, mostly produced software clusters.

After clustering, a sequence of corrections were made to the cluster energies. This included cluster overlap correction, boundary correction between small and large crystal region, missing crystal correction around the beam holes and the outer perimeter.

In order to determine the X(Y) position of the cluster, the sum of energies in the central column(row) and the adjacent columns(rows) were calculated. The energy ratio between the adjacent column(row) with larger energy and the central column(row) was used to get the cluster position within the central block, by looking up a table generated with GEANT. Typically, the position resolution for electromagnetic clusters was 1 mm.

4.3 Track-Cluster Matching and Vertex Finding

After cluster finding, the correct combination of track candidates in X and Y views was chosen by matching the cluster to a track position on the CsI calorimeter. The distance between the track X-Y position at the shower maximum and the cluster was required to be less than 7.0 cm. The combination of the X and Y view tracks with the smallest track-cluster separation was considered as the correct matching.

The momentum of a reconstructed track was measured by using the track bending angle in the X view and the p_t kick of the analysis magnet.

We proceeded to the vertex finding if four well-defined tracks were found. To obtain the vertex position, we looked at the Z position of the intersection of X-tracks and Y-tracks, and then we evaluated the vertex quality with χ^2 calculation.

Once the vertex position was confirmed to be inside the decay volume, various corrections were made on the hit positions in each chamber, in order to measure kinematic variables precisely.

These included the fringe field of the analysis magnet, chamber rotation, propagation time deviation by the hit position. The vertex position was finally determined from the fit with charged tracks weighted according to their multiple scattering angles and the errors in the hit position measurement in each chamber. For some events with multiple vertex position candidates, a proper vertex was chosen by looking at the fit quality of the vertex and tracks. In this analysis, the four-track vertex resolution was about 0.5 m in Z.

4.4 Particle Identification

Particle discrimination of charged pions and electrons are critical in the asymmetry study of the decay $K_L \rightarrow \pi^+ \pi^- e^+ e^-$. The e/π separation was done by using the information from the cluster energy E and the track momentum p . Electrons deposited most of their energy in the CsI calorimeter while pions deposited a part of their energy. This is because the CsI calorimeter had 27 radiation lengths, enough to contain all of the electron energy, but only 1.4 interaction lengths for pions.

Figure 4.2 shows a E/p distribution for electrons and pions of K_{e3} decays, where particles were identified by transition radiation detectors(TRDs). Electrons have a sharp peak at unity, while pions have a peak around zero with a gentle tail. A small peak at zero for electron was due to pions and muons misidentified by TRDs. In this analysis, we required the E/p to be unity within $\pm 10\%$ for electrons, and less than 0.9 for pions. In the electron identification, 99.6 % of electrons were accepted while 99.3 % of pions were rejected after this cut. This means the particle misidentification rate was only 0.7 % level with the E/p particle identification method. For further improvement of the particle identification, the KTeV detector was instrumented with transition radiation detectors(TRDs), although we did not use it for our analysis since we did not have any significant background originated from the particle misidentification.

Muons were vetoed by MU2 counter at the triggering level. No further suppression of muons were necessary because there was no significant background due to muons.

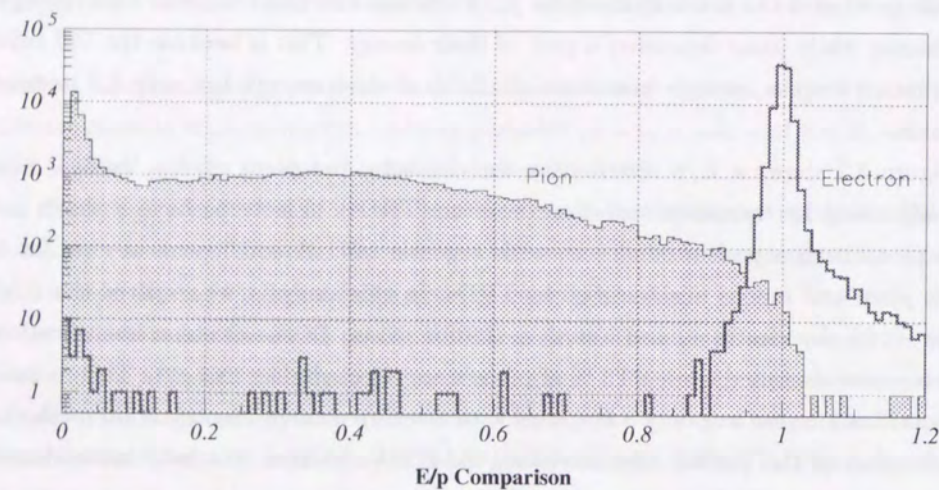


Figure 4.2: E/p comparison between electrons and pions of K_{e3} decays. Particles were identified by transition radiation detectors (TRDs). Electrons have a sharp peak at unity while pions have a peak around zero with a gentle tail. A small peak at zero for electron was due to pions and muons misidentified by TRDs.

Chapter 5

Event Selection

This chapter describes the event selection to suppress various types of backgrounds.

First, we summarize potential background sources remaining in the dataset after the triggering phase. Next, an event selection scheme to suppress backgrounds while keeping signal events is described. Finally, to estimate the absolute background level from each source, we explain the normalization procedure, which includes K_L flux measurement by using the decay $K_L \rightarrow \pi^+ \pi^- \pi_D^0$. In this chapter, to estimate the background level and signal acceptance, we used the Monte Carlo simulation described in Chapter 3.

5.1 Background

Here, let us classify background sources potentially contaminating the signal region. This helps us to decide a policy to reduce each background effectively. Generally speaking, backgrounds are complex compositions caused by a kinematical similarity, a lack of information from the detector, a finite resolution and smearing at the detection, accidental activity, and misreconstruction in the analysis. They should be suppressed with appropriate constraints.

The main background sources are classified into three groups:

1. Dalitz background. Charged tracks are reconstructed while one or more photons are missed.

$$K_L \rightarrow \pi^+ \pi^- \pi_D^0$$

$$K_L \rightarrow \pi^+ \pi^- \pi_D^0 (\pi^0 \rightarrow e^+ e^- e^+ e^-)$$

$$\Xi \rightarrow \Lambda (\rightarrow p \pi^-) \pi_D^0$$
2. Conversion background. A photon from decay products converts to an electron-positron pair at material.

$$K_L \rightarrow \pi^+ \pi^- \pi^0$$

$$K_L \rightarrow \pi^+ \pi^- \gamma$$
3. Double decay background. Two or more simultaneous decays in the detector happen to be

consistent with the signal.

Simultaneous decays of $K_L \rightarrow \pi^+ e^- \nu$ and $K_L \rightarrow \pi^- e^+ \nu$

These background sources are classified with the distinctive features of decay kinematics and topology from those of the signal. Therefore, different treatments are required for them. Here, let us consider how to suppress those background decays.

- $K_L \rightarrow \pi^+ \pi^- \pi_D^0$

This background was most serious in this study since it has a large branching ratio (1.5×10^{-3}) compared with the signal (3×10^{-7}). Especially, the event topology is exactly the same as the signal if the photon is missed or escaped from the detector or overlapped on the other cluster. The difference from the signal shows up in a finite transverse momentum squared of the four charged tracks, the invariant mass reconstructed with charged tracks, and an existence of a photon-like energy deposit in the CsI calorimeter. For further suppression, we introduced a constraint on a kinematical variable, named "Pp0kine", described later.

- $K_L \rightarrow \pi^+ \pi^- \pi_D^0 (\pi^0 \rightarrow e^+ e^- e^+ e^-)$

Although this decay mode has small branching ratio (4×10^{-6}), this mode is also a potential background, since two slow electrons in the products of $\pi^0 \rightarrow e^+ e^- e^+ e^-$ could easily be kicked out from the fiducial volume by the analysis magnet. The existence of two missing particles means that the invariant mass cut around kaon mass can limit this mode.

- $K_L \rightarrow \pi^+ \pi^- \pi^0$

This decay will give the same decay topology of $K_L \rightarrow \pi^+ \pi^- \pi_D^0$ if one of the photons from π^0 decay converted at material such as the vacuum window. This kind of background is named as a "conversion background." Fortunately, material upstream of the DC1 was kept very little, and the opening angle of the converted electron-positron pair is small enough so that we can identify and reject those effectively. Besides, this background has similar characteristics of the decay $K_L \rightarrow \pi^+ \pi^- \pi_D^0$.

- $K_L \rightarrow \pi^+ \pi^- \gamma$

Another conversion background is from the decay $K_L \rightarrow \pi^+ \pi^- \gamma$. This is potentially a background since the track topology is identical to the signal when the photon converts. As well as the other conversion background, this also has a small opening angle between the electron-positron pair, so the same cuts to reduce the conversion background will work well.

- $\Xi \rightarrow \Lambda (\rightarrow p \pi^-) \pi_D^0$

Since the KTeV detector could not distinguish π^\pm from a proton, this decay could be a background source. This decay mode was characterized with a large momentum of the Ξ and an offset vertex of $\Lambda \rightarrow p \pi^-$ from $\Xi \rightarrow \Lambda \pi_D^0$. A vertex quality cut and a constraint on the K_L momentum can reject this background.

- $K \rightarrow \pi^\pm e^\mp \nu$ simultaneous double decays

Simultaneous double decays of $K \rightarrow \pi^\pm e^\mp \nu$ gives the same charged track topology of the signal. Since their two vertices have no correlation, we can reject these events by looking at the vertex quality, as well as other kinematical constraints.

5.2 Basic Constraints

Before proceeding to the specific background rejection, we will apply basic constraints to the dataset, in order to verify the trigger constraint, and to define the fiducial volume of the KTeV detector. This reduces the uncertainty from the KTeV detector and the backgrounds, caused by the discrepancy between the detector simulation and the real detector.

5.2.1 Fiducial Volume Cut

In order to certify events from proper K_L decays, we required fiducial volume constraints for all events. The constraints should be made not only to define the decay volume and detector sensitive materials, but also to reject misreconstructed events.

- X-Y Vertex Constraint

The X-Y position of the reconstructed vertex projected onto the calorimeter from the target should be within the squares of $14 \text{ cm} \times 14 \text{ cm}$ centered at the beam-center, regardless of the beam size. This reduced events caused by interactions at materials, such as photon veto counters.

- Z Vertex Constraint

The vertex must be between $Z = 95 \text{ m}$ and 154 m . At $Z = 160 \text{ m}$, the vacuum window was placed and it could cause backgrounds from photon conversion and beam interaction. Around $Z = 90 \text{ m}$, the sweeper magnet and the defining collimeter were located, so this cut reduced events with products originating in them.

- Track hit position on the CsI calorimeter

When photons and charged tracks hit near the perimeter of the CsI calorimeter, the deposit energy of a particle would leak outside of the calorimeter. This caused an inaccurate energy cluster reconstruction. This means that the energy deposit calculation, track-cluster association, and, E/p might be unreliable around the perimeter. For this reason, the collar anti was served to veto hits around the beam holes. We made a verification that tracks did not point to the collar anti. In addition, we vetoed events with hits within 2 cm from the outer edge of the calorimeter.

5.2.2 Trigger Verification

Constraints were made on the data sample to ensure that events should satisfy the Level 1 and Level 2 trigger. This rejects the event which passed the trigger with extra accidental activities in the detector, even if the event could not have by itself. These “volunteer” events could not be simulated accurately in the Monte Carlo, so they should be removed from the data sample. The trigger verification was applied to the Monte Carlo events, also.

The trigger requirements were shown in Section 2.3. The required trigger verification was:

- There were at least three in-time hits in both V and V' banks which were associated with tracks. The in-time hits in the counter were identified with TDC timing.
- The minimum energy of the hardware cluster was required to be at least 2GeV. This suppressed the effect from the fluctuation of the HCC thresholds.
- Two electrons should have a total energy deposit in the CsI calorimeter of more than 11GeV. This verified the Etotal trigger processor.
- The deposit energies of the photon vetoes were required to be below their online thresholds.
- The muon veto counters were required not to have any in-time hits. The in-time hit was identified with TDC timing. Also, the threshold of counters was set the same as the online trigger.

5.2.3 Consistency Check

As further basic cuts, we checked that the events were consistent with the $K_L \rightarrow \pi^+ \pi^- e^+ e^-$ signal, as follows:

- The number of charged tracks was required to be exactly four, and all the tracks should share the same vertex. This requirement rejected any background with accidental hits or tracks.
- Four charged tracks should point to the CsI calorimeter. This gave us well-identified tracks.
- Events with extra hardware clusters, which had a deposit energy of 2GeV or more, were rejected. Such extra clusters were identified as photons.
- No cluster sharing was allowed. Since the particle identification was made with a cluster energy and a track momentum, a shared cluster gave wrong information of the deposit energy. The distance between two tracks at the shower maximum in the calorimeter should be 8 cm or more, for the same reason.
- Particles should be identified as $\pi^+\pi^-e^+e^-$, including the charges. A half of K_{e3} double decay background would be rejected with this cut.
- Since the reconstructed K_L momentum of signal was mostly populated over 40 GeV/c, we reject events with a momentum below 40 GeV/c.

5.3 Event Selection

After applying the basic constraints, we turn to background suppression against the individual background sources. Some backgrounds have been already suppressed with the basic cuts, but still background events were dominant in the data sample. The background feature was simulated well by the Monte Carlo in this phase, so that we compared the Monte Carlo to the data sample, in order to understand the kinematic feature of backgrounds.

An accumulation plot in Figure 5.1 shows the background contribution from each source overlaid onto the actual data. Note the plot was made of events with only $p_t^2 < 0.0001 \text{ GeV}^2/\text{c}^2$, to emphasize the signal peak and clarify the background contribution. Most of the events in the lower tail, $M_{\pi\pi ee} < 0.48 \text{ GeV}/\text{c}^2$, was from $K_L \rightarrow \pi^+\pi^-\pi_{(D)}^0$. At the K_L mass region, the background was from $K_L \rightarrow \pi^+\pi^-\gamma$, under the clear peak coming from the signal, $K_L \rightarrow \pi^+\pi^-e^+e^-$. In spite of their small contributions, the Ξ decay and the simultaneous double decays were still populated in higher mass tail.

We made further background reductions described in the following sections.

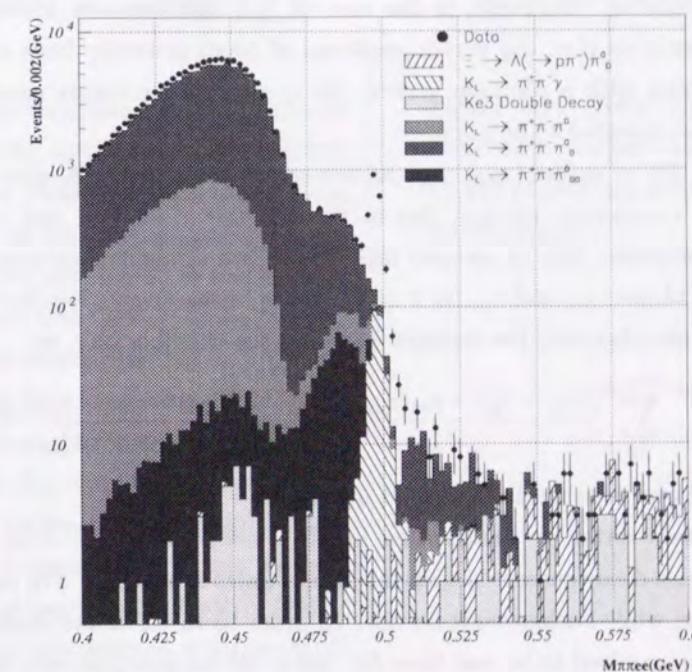


Figure 5.1: Mass distribution after the basic cut. To clarify the background contribution and the signal, transverse momentum squared was restricted to be less than $0.0001 \text{ GeV}^2/c^2$.

5.3.1 M_K Invariant Mass Cut

First, we defined the invariant mass window for four charged tracks. The window width was $|M_{\pi^+\pi^-e^+e^-} - M_K^0| < 0.005 \text{ GeV}/c^2$, where $M_{K^0} = 0.4978 \text{ GeV}/c^2$ [9]. As described in Section 5.3.7, this width corresponded to 2.9σ of the signal distribution.

5.3.2 Total Momentum Cut

The Ξ was produced at the target and had higher momentum of around 220 GeV/c at the peak. This is a striking contrast to the K_L , whose average momentum was 70 GeV/c. Figure 5.2 shows the momentum distributions of the signal and the hyperon decays. To reject $\Xi \rightarrow \Lambda(\rightarrow p\pi^-)\pi_D^0$, we required the total momentum to be below 200 GeV/c. As shown in Figure 5.3, we can reject 72 % of the cascade decays, while keeping 99.6% of the signal.

5.3.3 Vertex χ^2 Cut

For $\Xi \rightarrow \Lambda(\rightarrow p\pi^-)\pi_D^0$, since the Λ has a finite lifetime ($c\tau = 7.89 \text{ cm}$), the vertex position of $\Lambda \rightarrow p\pi^-$ has a certain offset from the primary vertex of $\Xi \rightarrow \Lambda\pi_D^0$, which can be detected with the KTeV spectrometer. Similarly, in the case of K_{e3} simultaneous double decays, both K_{e3} 's decay independently so that the vertex positions of them generally have a disparity. If we try to reconstruct them with a common vertex, the quality of the vertex reconstructed from these backgrounds were expected to be poor.

For example, let us define (x_{a2}, z_{xa2}) as the space point in the X view at DC2 for track a , and σ_{xa2} as the uncertainty on x_{a2} , due to the chamber resolution and multiple scattering at the upstream materials. Let us assume that tracks are straight lines coming from the vertex, (x_v, y_v, z_v) , with slopes, s_{xi} and s_{yi} , in x and y views, respectively. We can then form the vertex χ^2 using the distance between the straight lines and the chamber hits, as:

$$\chi^2 = \sum_i \sum_n^{4\text{tracks DC1,2}} \frac{[(x_{in} - x_v) - s_{xi}(z_{xin} - z_v)]^2}{\sigma_{xin}^2} + \frac{[(y_{in} - y_v) - s_{yi}(z_{yin} - z_v)]^2}{\sigma_{yin}^2}. \quad (5.1)$$

Here we summed over four tracks, and DC1 and DC2.

Figure 5.4 shows vertex χ^2 distribution for $K_L \rightarrow \pi^+\pi^-\pi^0$, $\Xi \rightarrow \Lambda(\rightarrow p\pi^-)\pi_D^0$, and K_{e3} simultaneous double decay generated with the Monte Carlo simulation. The signal has a sharp peak around the origin, while backgrounds do not. In order to reject Ξ and double K_{e3} backgrounds, the vertex χ^2 was required to be less than 50. After all the previous cuts, the signal acceptance was 98.9 % with the vertex χ^2 cut, while the acceptances of Ξ s and the K_{e3} double decays were 35.8 % and 36.0 %, respectively.

5.3.4 M_{ee} Cut

For the conversion backgrounds, such as $K_L \rightarrow \pi^+\pi^-\pi^0(\gamma)$, the invariant mass of electron-positron pair originated from a real photon is smaller than that from a virtual photon in $K_L \rightarrow \pi^+\pi^-\pi^0e^+e^-$.

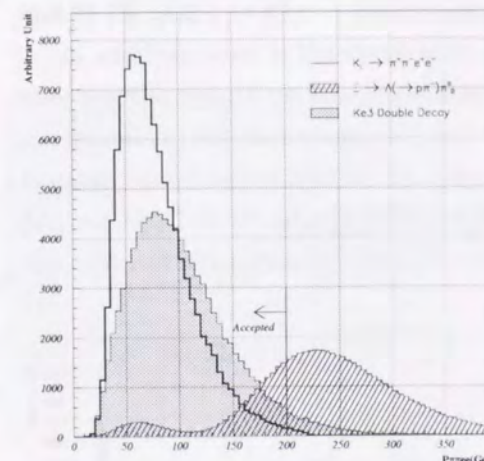


Figure 5.2: Total momentum distribution of four charged tracks, estimated with the Monte Carlo simulation. Note that each distribution is plotted with an arbitrary scale. The decay $\Xi \rightarrow \Lambda(\rightarrow p\pi^-)\pi_D^0$ dominated in the momentum region above 200 GeV/c, while the signal was in lower momentum region. A small peak around 60 GeV/c was an effect of the interaction at materials such as the defining collimeter. The K_{e3} simultaneous double decays also have higher total momentum than the signal. After introducing a total momentum constraint of less than 200 GeV/c, 72 % of the cascade decay was rejected, whereas 99.6% of the signal was kept.

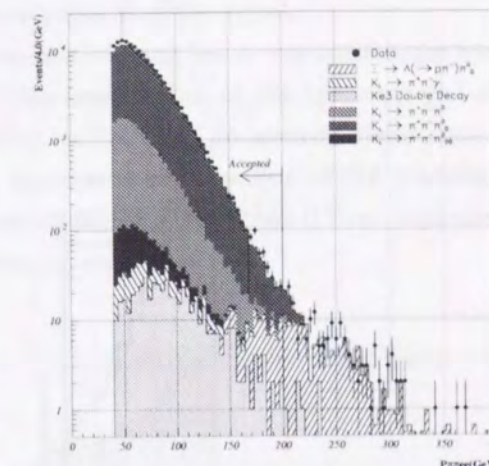


Figure 5.3: Total momentum distribution from each background source. Over 200 GeV/c of total momentum, the cascade decay was dominated.

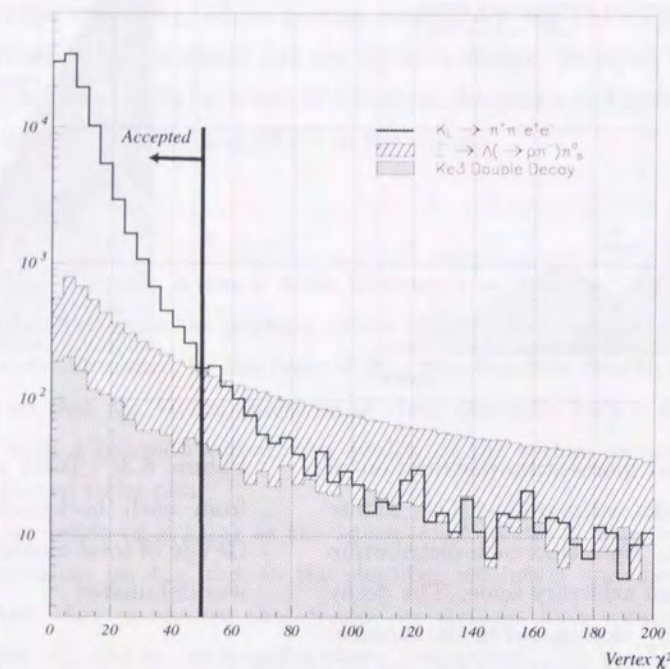


Figure 5.4: Vertex χ^2 distribution for $K_L \rightarrow \pi^+\pi^-e^+e^-$, $\Xi \rightarrow \Lambda(\rightarrow p\pi^-)\pi^0$, and K_{e3} simultaneous double decay generated with the Monte Carlo simulation after basic cuts. The number of events for the decays are not normalized. The signal has a sharp peak at the origin while backgrounds do not. The cut for the vertex χ^2 was introduced at 50. After all the previous cuts, the signal acceptance was 98.9 % with this cut, while the acceptances of Ξ s and the K_{e3} double decays were 35.8 % and 36.0 %, respectively.

This means that the electron-positron pair have a very small opening angle. This is a prominent feature to distinguish a virtual photon conversion from a real photon conversion.

Figure 5.5 shows M_{ee} distributions for $K_L \rightarrow \pi^+\pi^-e^+e^-$ and $K_L \rightarrow \pi^+\pi^-\pi^0$ generated with the Monte Carlo simulation. The conversion background is populated in a very low invariant mass region while the signal has a very long tail. The cut at $M_{ee} > 0.002\text{GeV}/c^2$ gave a very clear separation from the conversion background. This cut rejected 96.4% of $K_L \rightarrow \pi^+\pi^-\pi^0$ background and 97.7% of $K_L \rightarrow \pi^+\pi^-\gamma$ background, while keeping 86.6 % of the signal.

In addition, even in the signal mode, the electron-positron pair has a very small angle because they are the virtual photon conversion product. This implies that at the upstream end of the spectrometer, the two tracks are still close together, so DC1 has to identify those close hits. Because simultaneous hits in the same drift cell aggravated the precision of the tracking, the $M_{ee} > 0.002\text{GeV}/c^2$ cut assured the track separation at DC1 is greater than 0.7 cm, equivalent to one drift cell separation for the decay within the fiducial region.

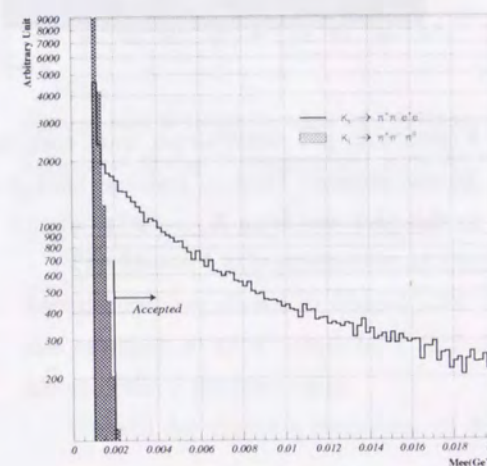


Figure 5.5: M_{ee} distribution after all the previous cuts for $K_L \rightarrow \pi^+\pi^-e^+e^-$ and $K_L \rightarrow \pi^+\pi^-\pi^0$ generated with the Monte Carlo simulation.

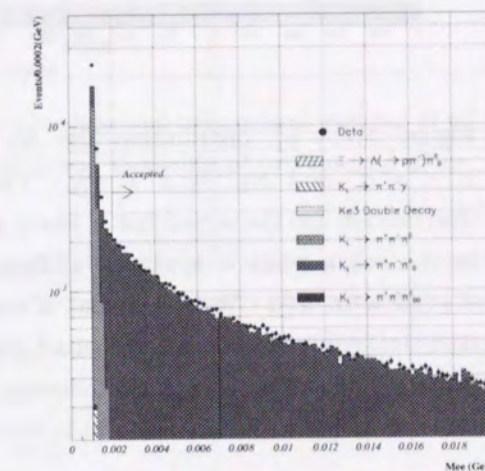


Figure 5.6: M_{ee} distribution from each background source. The conversion backgrounds such as $K_L \rightarrow \pi^+\pi^-\gamma$ and $K_L \rightarrow \pi^+\pi^-\pi^0$ were populated in the region of $M_{ee} < 0.002\text{GeV}/c^2$.

5.3.5 p_t^2 Cut

The total momentum of decay products must be the same as that of the decay particle. For this fixed target experiment, it is useful to define p_t^2 , the transverse momentum squared of the decay products, relative to the straight line between the target and decay vertex.

Generally speaking, the p_t^2 is exactly zero for $K_L \rightarrow \pi^+\pi^-e^+e^-$. However, p_t^2 has a uniform

distribution for the decay with missing particles as shown in Figure 5.7. In our analysis, we use this difference to reject the background, which mimicked the signal with some missing particles. A constraint on p_t^2 will be determined in the following section.

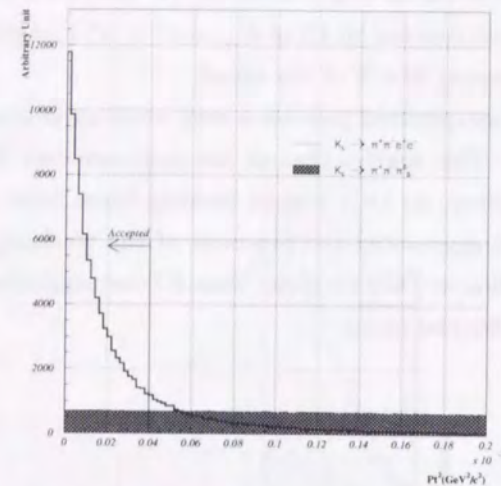


Figure 5.7: p_t^2 distribution for $K_L \rightarrow \pi^+\pi^-e^+e^-$ and $K_L \rightarrow \pi^+\pi^-\pi_D^0$. The p_t^2 distribution for the signal has a sharp peak at the origin while it is almost uniform for $K_L \rightarrow \pi^+\pi^-\pi_D^0$. We introduced a cut at $0.00004\text{GeV}^2/c^2$ to separate the background contribution as discussed in the following section.

5.3.6 Pp0kine Cut

After all the above cuts, the remaining background to $K_L \rightarrow \pi^+\pi^-e^+e^-$ came from $K_L \rightarrow \pi^+\pi^-\pi_D^0$ decays where an extra photon was not detected. To reduce this background, we used a kinematic variable called “Pp0kine” [51, 52](Appendix B).

The parameter Pp0kine shows a very unique feature of the kinematic relation in the mode where one particle in the final state was either missed or ignored. In our case, we assumed that the event is $K_L \rightarrow \pi^+\pi^-\pi^0$ and we missed the π^0 in its final state. The π^0 longitudinal momentum is reconstructed from the given information, π^0 mass, π^\pm momenta and their mass, and the K_L direction vector extrapolating from the target to the vertex position. We then look at the square of π^0 longitudinal momentum in the frame boosted along the K_L flight direction, where the longitudinal momentum of the $\pi^+\pi^-$ system is equal to zero. This is the definition of Pp0kine.

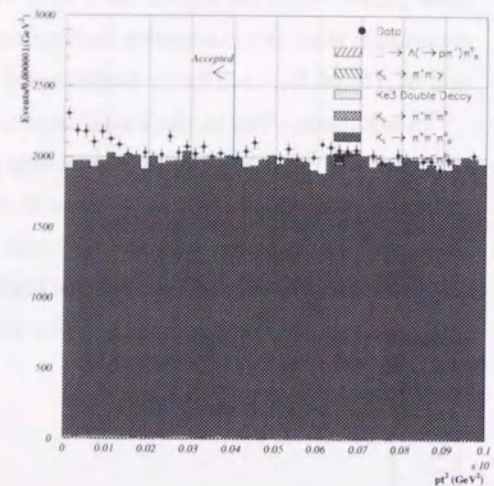


Figure 5.8: p_t^2 distribution from each background source. Most of residual background in this plot was from $K_L \rightarrow \pi^+\pi^-\pi_D^0$.

The exact formulation is as follows:

$$\text{Pp0kine} = \frac{(M_K^2 - M_{\pi^0}^2 - M_{\pi\pi}^2)^2 - 4M_{\pi^0}^2 M_{\pi\pi}^2 - 4M_K^2 (P_T^2)_{\pi\pi}}{4[(P_T^2)_{\pi\pi} + M_{\pi\pi}^2]} \quad (5.2)$$

where $M_{\pi\pi}$ is the invariant mass of the $\pi^+\pi^-$ system, M_{π^0} is the mass of π^0 , M_K is the mass of K_L , and $(P_T^2)_{\pi\pi}$ is the square of the transverse momentum of the $\pi^+\pi^-$ system with respect to the kaon flight vector. Figure 5.9 shows a schematic view of the situation.

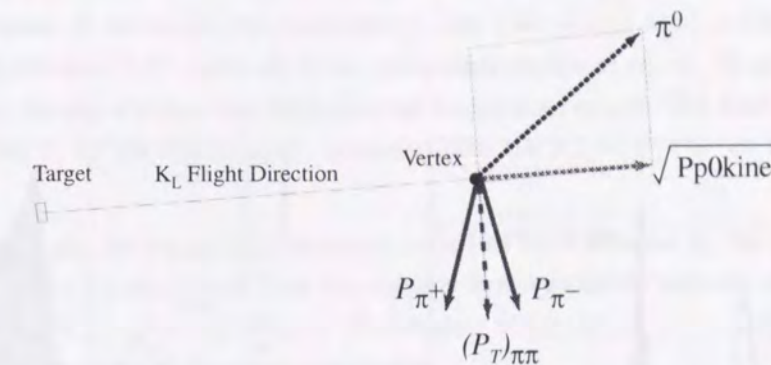


Figure 5.9: Schematic view of Pp0kine. Pp0kine is a longitudinal momentum squared of π^0 in the kaon rest frame reconstructed with K_L flight direction and momenta of two charged pions.

The Monte Carlo predictions of the distribution of Pp0kine for the signal and $K_L \rightarrow \pi^+\pi^-\pi_D^0$ background are shown in Figure 5.10. For $K_L \rightarrow \pi^+\pi^-\pi_D^0$, Pp0kine is positive-definite because the momentum of π^0 must be a real. On the other hand, Pp0kine of the signal event does not always take a positive value.

We will determine a constraint of the combination of p_t^2 and Pp0kine in the next section.

5.3.7 Optimization of p_t^2 and Pp0kine Cuts

Based on the Monte Carlo simulation, optimum cuts for p_t^2 and Pp0kine are considered by looking at a matrix in Table 5.1, with an invariant mass window defined in section 5.3.1. Since the background is expected to be dominated by $K_L \rightarrow \pi^+\pi^-\pi_D^0$, the number of background events was estimated by $K_L \rightarrow \pi^+\pi^-\pi_D^0$ Monte Carlo simulation.

In principle, there are three constraints to determine the optimum cuts configuration:

1. At least 1000 signal events are required to evaluate the theoretical predictions in the angular asymmetry measurement with a good confidence level (3σ or larger).
2. Number of background events is small enough to ignore its effect in the form factor and asymmetry measurements. Since we plan to include the background effect into systematic

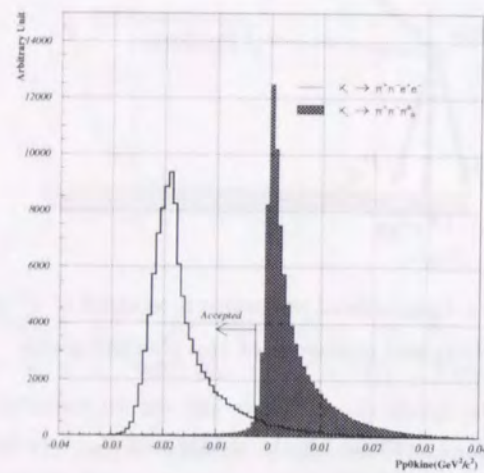


Figure 5.10: Pp0kine distribution for the signal $K_L \rightarrow \pi^+\pi^-e^+e^-$ and the background $K_L \rightarrow \pi^+\pi^-\pi_D^0$ after basic cuts. The background is populated mostly in the positive, physically allowed region, while the signal can be in negative region. A small smearing into the negative region of $K_L \rightarrow \pi^+\pi^-\pi_D^0$ is due to resolution effects.

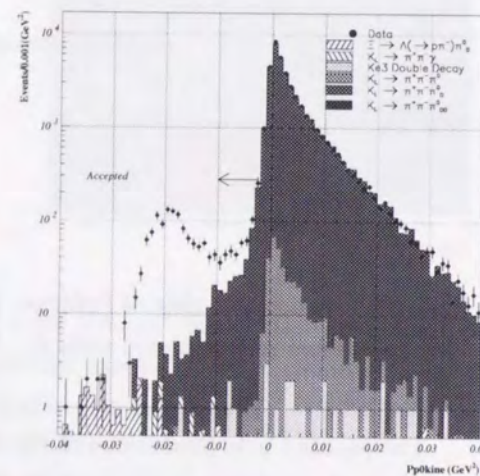


Figure 5.11: Pp0kine distribution from each background source. In the negative-definite region, an excess over the background was expected to be $K_L \rightarrow \pi^+\pi^-e^+e^-$ signal.

uncertainty, number of background events should be less than 1/3 of the uncertainty from the statistical fluctuation of the signal.

3. Since Pp0kine cut directly changes $M_{\pi\pi}$ distributions in $K_L \rightarrow \pi^+\pi^-e^+e^-$ decay, this cut may affect the acceptance calculation. Therefore, Pp0kine cut should be loose.

From constraint 1, we should pick set of constraints with more than 1000 signal events. The constraint 2 requires that the number of background should be less than 10 events if we assume 1000 signal events. If we require the constraint 3, only a set of cuts of $p_t^2 < 0.00004 \text{ GeV}^2/c^2$ and $\text{Pp0kine} < -0.0025 \text{ GeV}^2/c^2$ meets all of our constraints explained above. Therefore, we obtained 1173 events in the signal region and 9.03 expected background events. The final acceptance of the signal was 1.392 % for the signal events, estimated with the $K_L \rightarrow \pi^+\pi^-e^+e^-$ Monte Carlo.

After all the cuts, the signal window was expected to be dominated by the $K_L \rightarrow \pi^+\pi^-e^+e^-$ signal. In Figure 5.12, a sharp peak from the signal is shown while the events in the lower mass tail were mostly from $K_L \rightarrow \pi^+\pi^-\pi_D^0$ decays. The window width $|M_{\pi^+\pi^-e^+e^-} - M_K^0| < 0.005 \text{ GeV}/c^2$ corresponds to the $\pm 2.9\sigma$ of the signal distribution.

$p_t^2 (10^{-5} \text{ GeV}^2/c^2)$	< 20	< 15	< 10	< 8	< 6	< 4	< 2
pp0kine (GeV^2/c^2)							
N/A	1813 199.4	1778 188.6	1731 169.2	1679 162.5	1620 148.6	1485 124.7	1191 88.5
< -0.00	1498 63.1	1467 57.86	1428 46.1	1387 41.1	1341 35.3	1232 30.4	982 18.9
< -0.025	1414 35.5	1387 31.3	1352 19.5	1315 15.6	1274 12.5	1173 9.03	939 4.51
< -0.05	1380 30.0	1355 25.8	1322 15.0	1287 12.5	1246 10.5	1150 8.00	921 4.51
< -0.075	1330 25.4	1306 21.2	1274 10.5	1240 8.72	1202 7.70	1108 5.23	887 4.51
< -0.100	1266 20.6	1242 16.4	1212 8.42	1180 6.68	1142 5.65	1051 3.19	841 2.47
< -0.125	1173 16.7	1151 12.5	1122 5.95	1093 4.21	1057 3.19	971 1.74	776 1.02

Table 5.1: Signal to background ratio matrix table. (Numerator: number of events after the cuts. Denominator: number of estimated background events from $K_L \rightarrow \pi^+\pi^-\pi_D^0$ Monte Carlo.)

5.4 Acceptance and Data After Final Cuts

The previous section described the event selection to suppress backgrounds to a sufficient level. Here, we turn to summarize the signal acceptance in each analysis phase. Table 5.2 shows the estimated signal acceptance at each analysis phase. With the basic cuts, we lost nearly 3/4 of events: the requirements for four tracks hitting the CsI calorimeter with a shared vertex, and identified two pions and two electrons, lost 66% of the signal. The other loss by the basic cuts was due to the fiducial volume cuts and the trigger verification. At the end, the signal efficiency was 1.39 %, and from data, we accepted 1173 events as signal candidates.

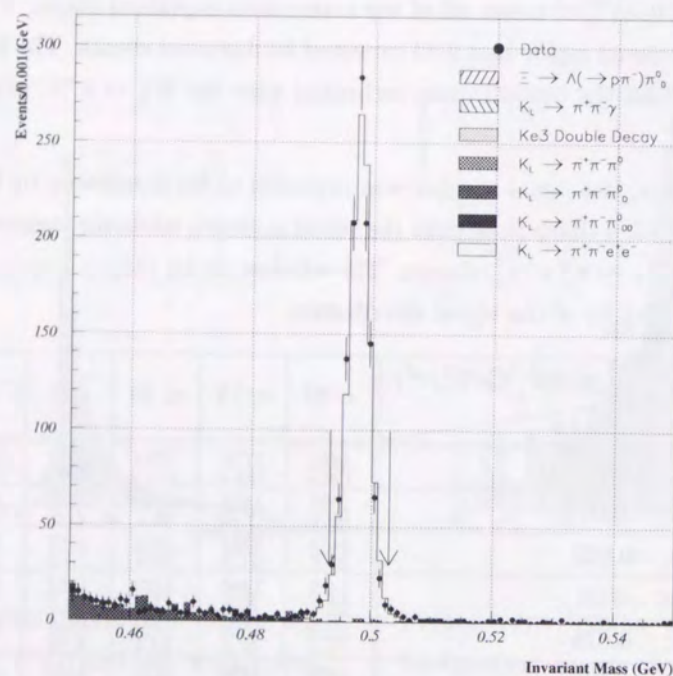


Figure 5.12: Invariant mass distribution after final cuts. The mass window is defined as $|M_{\pi^+\pi^-e^+e^-} - M_K^0| < 0.005\text{GeV}/c^2$, which corresponds to the $\pm 2.9\sigma$ of the signal distribution. In this plot, the number of events in the signal window is 1173 events while the expected number of backgrounds is 9. The residual background in the signal region was mostly from $K_L \rightarrow \pi^+\pi^-\pi^0_D$. The normalization of the signal Monte Carlo is based on the previous publication, $BR(K_L \rightarrow \pi^+\pi^-e^+e^-) = 3.2 \times 10^{-7}$ [12].

Table 5.2: The estimated signal acceptance at each analysis phase from $K_L \rightarrow \pi^+\pi^-e^+e^-$ Monte Carlo.

Analysis phase	Efficiency
Level 1 trigger	12.8%
Level 2 trigger	9.08%
Level 3 trigger	8.40%
Basic Cuts	2.18%
$0.493 < M_K < 0.503\text{GeV}/c^2$	2.07%
$P_{\pi\pi ee} < 200\text{GeV}/c$	2.06%
Vertex $\chi^2 < 50$	2.05%
$M_{ee} > 0.002\text{GeV}/c^2$	1.78%
$p_t^2 < 0.00004 (\text{GeV}^2/c^2)$	1.49%
$Pp0kine < -0.0025(\text{GeV}^2/c^2)$	1.392%

5.5 Background Estimation

Since background contaminating the signal region causes systematic uncertainty in the analyses, we have to understand it, and certify that it is ignorable. In this chapter, we summarize the background level from each background source with the flux-normalized Monte Carlo simulation. In addition, we fit the sideband of signal region to estimate the background, and compare it with the estimation from the Monte Carlo prediction.

5.5.1 Background Level from Each Source

Here, we estimate the background by using the Monte Carlo simulation except for the simultaneous double decays. We generated the same number of events as the K_L flux for $K_L \rightarrow \pi^+\pi^-\pi^0_D$ because of its huge statistics. The number of generated events with the Monte Carlo simulation corresponded to three times the K_L flux for the other background sources.

For K_{e3} simultaneous double decays, the background level was evaluated from the real data. Namely, we looked at another possible final state, $\pi^\pm\pi^\pm e^\mp e^\mp$ from the K_{e3} double decays, and calculated the number of events in the signal region by applying the analysis cuts explained above. This obtained number of events was considered to be the same as the number of background events from K_{e3} double decays, $(K_L \rightarrow \pi^+e^-\nu) + (K_L \rightarrow \pi^-e^+\nu)$.

Table 5.3 shows the efficiency of each background source and the estimated number of background events, which was normalized with the measured K_L flux. The most prominent background was from $K_L \rightarrow \pi^+\pi^-\pi^0_D$. Some backgrounds did not appear in the background estimation so that we set the upper limit at the 90% confidence level.

We determined that the number of background events was 11.3 ± 3.5 .

Table 5.3: The estimated background acceptance of each background source generated with the Monte Carlo. The estimated background levels were normalized to the K_L flux, so the sum of them is the final number of background events in the signal region.

Background source	Efficiency	Background events
$K_L \rightarrow \pi^+\pi^-\pi_D^0$	2.4×10^{-8}	9.0 ± 3.0
$K_L \rightarrow \pi^+\pi^-\pi^0$	$< 1.2 \times 10^{-11}$	$< 0.8(90\% \text{C.L.})$
$K_L \rightarrow \pi^+\pi^-\pi_D^0\pi_D^0$	2.7×10^{-7}	0.3 ± 0.2
$K_L \rightarrow \pi^+\pi^-\gamma$	$< 3.0 \times 10^{-8}$	$< 0.7(90\% \text{C.L.})$
K_{e3} double decay		2.0 ± 1.4
$\Xi \rightarrow \Lambda\pi_D^0$	$< 8.3 \times 10^{-9}$	$< 0.7(90\% \text{C.L.})$
Total		11.3 ± 3.5

5.5.2 Background estimation with sideband fit

Since the background was mostly from $K_L \rightarrow \pi^+\pi^-\pi_D^0$, the background level was also estimated by fitting the sideband with the distribution of $K_L \rightarrow \pi^+\pi^-\pi_D^0$ Monte Carlo, in the region of $0.45 < M_{\pi\pi ee} < 0.48 \text{GeV}/c^2$ after the final cut. The estimated number of the background events in the signal region by this method was 10.6 ± 3.3 events, consistent with the background estimation from the flux normalization.

5.5.3 Summary of Background Level

The number of background events estimated by the flux normalization and sideband fitting indicated approximately 11 events. This gives the signal to background ratio of over 100. Comparing to the statistical uncertainty of the signal, 1173 ± 34.2 events, the background was small enough to be ignorable in both the form factor measurement and angular asymmetry analysis. Hence, in the following chapter, the contribution from the background was treated as a systematic uncertainty, and not subtracted.

5.6 K_L Flux Calculation

In the previous section, we utilized an estimated K_L flux in the collected data to normalize the Monte Carlo event generation for background. The measured K_L flux was used for signal normalization, to optimize the cuts to suppress background, and to estimate the background level in the signal region.

Since the normalization mode was required to have a similar feature as the signal to reduce a systematic uncertainty, we used the decay $K_L \rightarrow \pi^+\pi^-\pi_D^0$ for the normalization in our study. $K_L \rightarrow \pi^+\pi^-\pi_D^0$ has four charged tracks, including two electrons from internal conversion of a virtual photon, two charged pions, and an extra photon.

Here, we explain the K_L flux measurement in our analysis.

5.6.1 Acceptance and Flux Calculation

We defined the K_L flux as the number of K_L decays in the fiducial volume in the kaon energy range of 20 to 220 GeV and decay position between 90 and 160 m downstream from the target. The Monte Carlo $K_L \rightarrow \pi^+\pi^-\pi_D^0$ decay was generated within the fiducial volume and energy defined above.

The event selection for the normalization mode, $K_L \rightarrow \pi^+\pi^-\pi_D^0$, was performed by using the exactly same tracking, clustering and vertexing algorithms as used for the signal mode.

The basic constraint was the same as for the signal described in Section 5.2 except for a photon identification. The same fiducial volume cut was made for a vertex position shared with four tracks. In addition, all four tracks were required to hit the CsI calorimeter, to identify two electrons and two pions, which are consistent with $K_L \rightarrow \pi^+\pi^-\pi_D^0$. Only one extra photon was required in the calorimeter with at least 2 GeV energy deposit. The extra photon was required to be more than 0.4 m away from pion energy clusters, in order to avoid misidentification from pion's satellite clusters. The identified photon cluster and the two electrons were required to form the π^0 invariant mass; $0.127 < M_{e^+e^-\gamma} < 0.143 \text{GeV}/c^2$. Finally, K_L invariant mass cut was made as $0.492 < M_{\pi^+\pi^-\pi^0} < 0.504 \text{GeV}/c^2$. The summary of cuts is shown in Table 5.4.

Table 5.4: Cuts for $K_L^0 \rightarrow \pi^+\pi^-\pi_D^0$.

Cut	Description
$95\text{m} < Z_{\text{vertex}} < 154\text{m}$	Fiducial volume Cut
Photon Cluster Energy $> 2.0 \text{GeV}$	
Minimum Cluster Sep $> 0.4\text{m}$	distance from π^\pm to a photon
4 tracks hit the CsI	Verify PID, Reject Hyperons
Vertex $\chi^2 < 50$	Ke3 Double decays and Hyperons
Charges consistent with $\pi^+\pi^-\pi_D^0$	Ke3 Double decays
$M_{ee} > 0.002 \text{GeV}/c^2$	
$0.127 < M_{ee\gamma} < 0.143 \text{GeV}/c^2$	
$0.490 < M_{\pi\pi ee\gamma} < 0.506 \text{GeV}/c^2$	

The possible background source in the normalization mode was $K_L \rightarrow \pi^+\pi^-\pi^0$ with a photon converted at the vacuum window, since they had the same topology as four charged tracks and a photon. The reduction for this background source was mostly done by invariant mass cut for two electrons, $M_{ee} > 0.002 \text{GeV}/c^2$, as described in the signal selection. Other background source was the Ξ decay, but expected to be a very small contribution. The result of background study is shown in Table 5.5. The background level itself, which was evaluated to be only 0.43% of the flux of normalization mode, was found to be smaller than the other systematic uncertainties.

The acceptance of normalization mode was calculated based on the ratio of the number of accepted Monte Carlo events to the number of generated events. The result was $(0.6065 \pm 0.0005)\%$ for the winter run and $(0.5850 \pm 0.0005)\%$ for the summer run, where errors are statistical only.

The number of accepted events was about 2.12 millions after subtracting 16000 background events shown in Table 5.5. Using the branching ratio, $Br(K_L \rightarrow \pi^+\pi^-\pi_D^0) = (0.151 \pm 0.0047)\%$ [9], the K_L flux was estimated as $(2.343 \pm 0.0016) \times 10^{11}$ K_L decays.

Figure 5.13 shows the invariant mass distributions of data and the Monte Carlo simulation after all cuts were applied. The discrepancy at higher mass region between data and Monte Carlo simulation was of 0.3%, as described later.

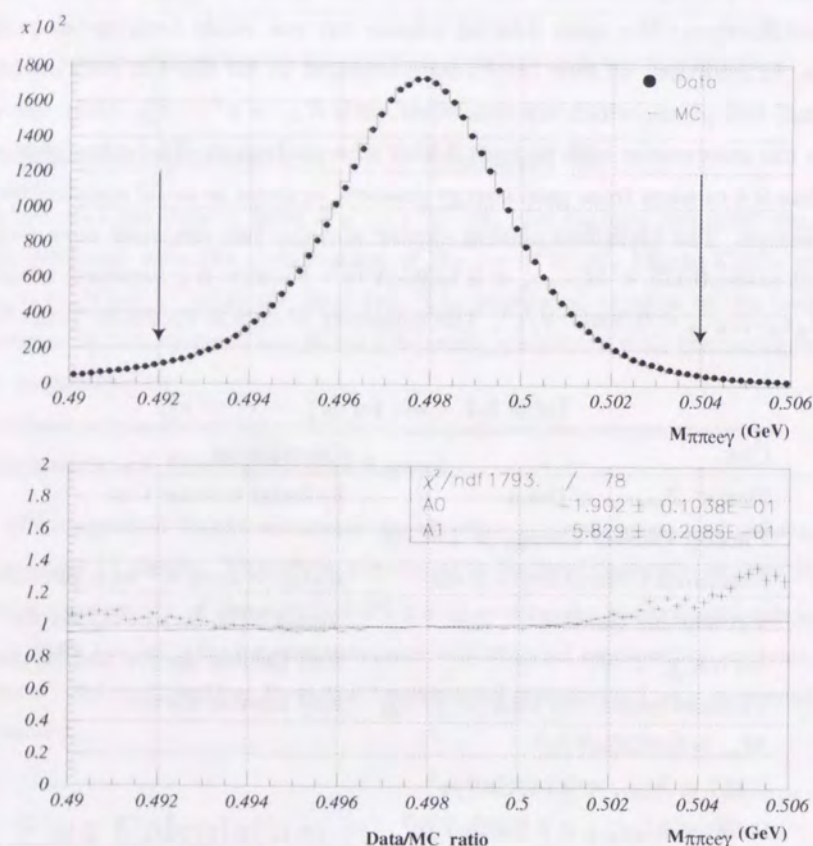


Figure 5.13: Distribution of mass of $\pi^+\pi^-e^+e^-\gamma$ after all cuts. Dots shows data and histogram shows the Monte Carlo simulation in upper plot. Lower plot shows ratios between data and the Monte Carlo. The discrepancy at higher mass tail gave the flux uncertainty of only 0.3% level.

5.6.2 Systematic Uncertainty

We now consider systematic uncertainty in the normalization.

$K_L \rightarrow \pi^+\pi^-\pi_D^0$ Branching Ratio

Particle Data Group [9] reports $K_L \rightarrow \pi^+\pi^-\pi^0$ branching ratio as $(12.56 \pm 0.20)\%$, and π^0 Dalitz decay branching ratio as $(1.198 \pm 0.032)\%$. These cause the relative flux uncertainty of 1.6% and 2.7% respectively, and the quadratically combined error is 3.14%.

π^0 Form Factor

Another possible error source was an uncertainty of the π^0 form factor in the Dalitz decay. We parameterized the form factor as

$$F = 1 + ax \quad (5.3)$$

with $a = 0.032 \pm 0.004$ for the slope [9], where $x = (m_{ee}/m_{\pi^0})^2$. The form factor causes the enhancement at high mass tail of M_{ee} . This uncertainty to the flux measurement was very small as expected from Equation 5.3. The error was evaluated as 0.046%, so the error could be neglected in the flux measurement.

Background Subtraction

As shown in Table 5.5, since the fraction of background was as small as 0.43% of the $K_L \rightarrow \pi^+\pi^-\pi_D^0$ decays, the expected uncertainty from background subtraction was only 0.0019%. Thus, we concluded that the uncertainty from background subtraction was negligible.

Table 5.5: Summary of the background level at the flux measurement.

Source	Expected BG events
$K_L \rightarrow \pi^+\pi^-\pi^0$	(16001 ± 75) events
$\Xi \rightarrow \Lambda\pi_D^0$	(1.5 ± 0.8) events
K_{e3} Double decays	(62 ± 7.9) events

Drift Chamber Inefficiency

A tracking inefficiency was found in neutral beam region of upstream drift chambers. The detail will be described later in each signal analysis, so we give a short explanation and systematic study for the normalization mode here.

The discrepancy between data and the detector simulation in the total tracking inefficiency in upstream chambers was reported to be 5% in the worst case. To study the effect, we reduced the tracking efficiency by 5% in the beam region in the Monte Carlo simulation. This decreased the

acceptance of normalization mode by 1.85 %. Hence, we included this in systematic uncertainty. However, this error is almost canceled out when taking the ratio in the branching ratio measurement of $K_L \rightarrow \pi^+\pi^-e^+e^-$, so we will study this effect again in the branching ratio measurement.

Energy Cluster Threshold

For clustering of photons and electrons, we utilized the hardware cluster counting(HCC). The threshold for the crystal at the local maximum of the cluster was approximately 1GeV. However, the threshold level of each crystal in the Monte Carlo did not agree well with data. Figure 5.14 shows data and Monte Carlo comparison of HCC threshold distributions of 3100 CsI crystals for both the winter and summer run. Obviously, the threshold level of Monte Carlo was higher by about 5% in the winter run and 10% in the summer run, than the actual data. This effect in the Monte Carlo could decrease the trigger efficiency of HCC requirement, especially for the low energy electrons and photons.

In order to evaluate this effect, we artificially shifted the threshold for all crystals to agree with data. This only changed 0.1 % of the number of Monte Carlo events. This is because that electrons were required to solely satisfy E_{total} and hardware cluster threshold at the trigger verification: sum of two electron energies should be 11GeV or more, and each electron must have a momentum of 2 GeV/c or higher.

Therefore, we assigned 0.1 % as the systematic uncertainty from this source.

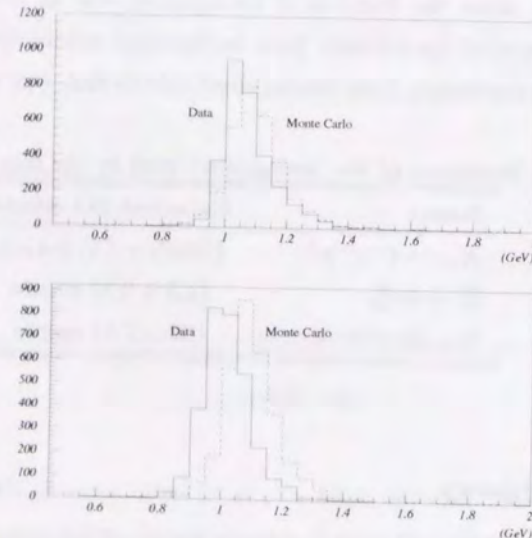


Figure 5.14: HCC threshold distribution. Solid histograms are from data, dashed ones from Monte Carlo. Top plot is taken from the winter data and bottom is from the summer data. The peaks of data were shifted by about 5 to 10%, compared to the Monte Carlo.

Mass Resolution

As shown in Figure 5.13, the comparison of $M_{\pi\pi ee\gamma}$ distributions between data and the Monte Carlo was almost consistent. However, there was a small discrepancy at higher and lower mass regions. This came from a photon reconstruction accuracy, such as the accidental overlay and pion shower simulation. To see the effect of discrepancy, we changed the mass cut position to $0.492 < M_{\pi\pi ee\gamma} < 0.500 \text{ GeV}/c^2$ and compared it with the sample with nominal cut. Applying this mass cut, we found that the K_L flux was changed by 0.4% for the winter run and 0.3% for the summer run. We introduced an averaged error of 0.3% as a systematic uncertainty from this source.

5.6.3 Summary

We summarize the flux measurement with the decay $K_L \rightarrow \pi^+\pi^-\pi_D^0$. Most part of uncertainty in this measurement came from the branching ratio measurement of this mode, 3.14%, and the total uncertainty is 3.7%, as shown in Table 5.6. Total K_L flux was $(2.343 \pm 0.002(stat) \pm 0.085(syst)) \times 10^{11}$, as shown in Table 5.7. Since the statistical error was 0.07% level in the flux calculation while the error from the branching ratio uncertainty was approximately 3% level, the error was naturally systematic dominant. As described above, some systematic sources will be canceled out when we proceed to the branching ratio measurement.

Table 5.6: Summary of systematic uncertainty in the flux measurement.

Source	Uncertainty
$K_L \rightarrow \pi^+\pi^-\pi_D^0$ Branching ratio measurement	3.14%
Drift chamber inefficiency	1.9%
$M_{\pi\pi ee\gamma}$ mass resolution	0.3%
Cluster energy threshold	0.1%
$K_L \rightarrow \pi^+\pi^-\pi_D^0$ Monte Carlo statistics	0.06%
π^0 form factor	0.05%
Background subtraction	0.002%
Total	3.66 %

Table 5.7: Summary of the flux calculation with $K_L^0 \rightarrow \pi^+\pi^-\pi_D^0$. Expected background was already subtracted.

Dataset	# Events(Data)	K_L flux
Winter	1301650	1.421×10^{11}
Summer	814227	0.922×10^{11}
Total	2115877	$(2.343 \pm 0.002(stat.) \pm 0.085(syst.)) \times 10^{11}$

Chapter 6

Form Factor Measurement

In the decay matrix element of $K_L \rightarrow \pi^+\pi^-e^+e^-$, there is an ambiguity in the form factor measurement for the $gM1$ magnetic dipole transition. Recently, KTeV collaboration has reported a preliminary result on this measurement through a photon spectrum in the decay $K_L \rightarrow \pi^+\pi^-\gamma$ [50]. Since we can make a precise measurement of the form factor through $K_L \rightarrow \pi^+\pi^-e^+e^-$, we independently determine the form factor here and compare distributions of characteristic variables, especially the pions invariant mass, $M_{\pi\pi}$.

6.1 Formulation

The matrix element of $K_L \rightarrow \pi^+\pi^-e^+e^-$ described in Chapter 1 matched the data well in most of the kinematic variable distributions. However, $M_{\pi\pi}$ distribution for the data shifted higher than the Monte Carlo with a constant $gM1$, as shown in Figure 6.1. This is phenomenologically understood as an effect of vector-meson dominance in the M1 direct emission amplitude. This suggests that the photoemission in this kind of decays is also intermediated by a vector meson, ρ , as shown in Figure 6.2.

This effect was already pointed out in Ref [22, 29] and observed through $K_L \rightarrow \pi^+\pi^-\gamma$ in Ref. [37]. The data and Monte Carlo comparison with and without the form factor in $K_L \rightarrow \pi^+\pi^-\gamma$ are shown in Figure 6.3. The effect makes the structure function of the form of

$$\begin{aligned} gM1 &\longrightarrow gM1 \cdot F, \\ F &= a_1[(M_\rho^2 - M_K^2) + 2M_K E_\gamma]^{-1} + a_2, \end{aligned} \quad (6.1)$$

where M_ρ is the mass of ρ vector meson, M_K is the mass of kaon, and E_γ is an energy of the photon in the K_L rest frame.

For the decay $K_L \rightarrow \pi^+\pi^-e^+e^-$, it was natural to modify the form factor by replacing the photon in the decay $K_L \rightarrow \pi^+\pi^-\gamma$ by a virtual photon which converts to e^+e^- . We used a

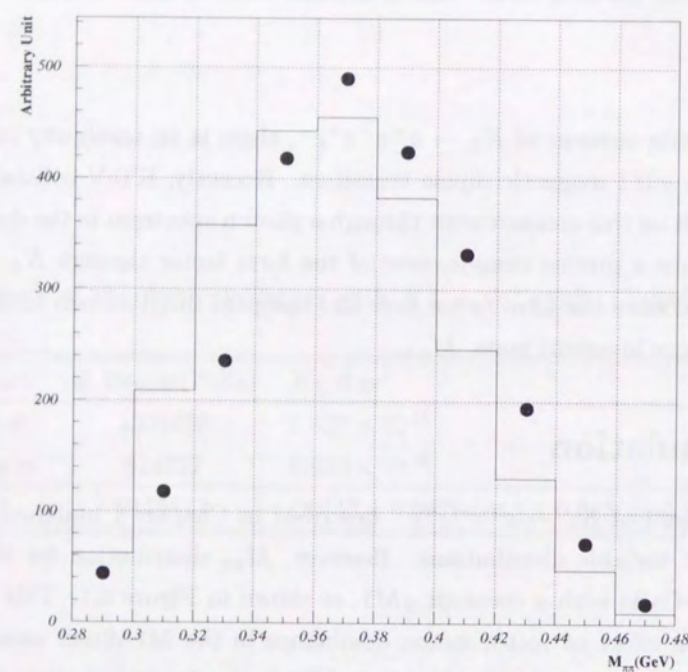


Figure 6.1: $M_{\pi\pi}$ distributions of data(dots) and Monte Carlo with a constant $gM1$ (histogram) in the decay $K_L \rightarrow \pi^+\pi^-e^+e^-$. The distribution of the Monte Carlo clearly shifted lower than that of data.

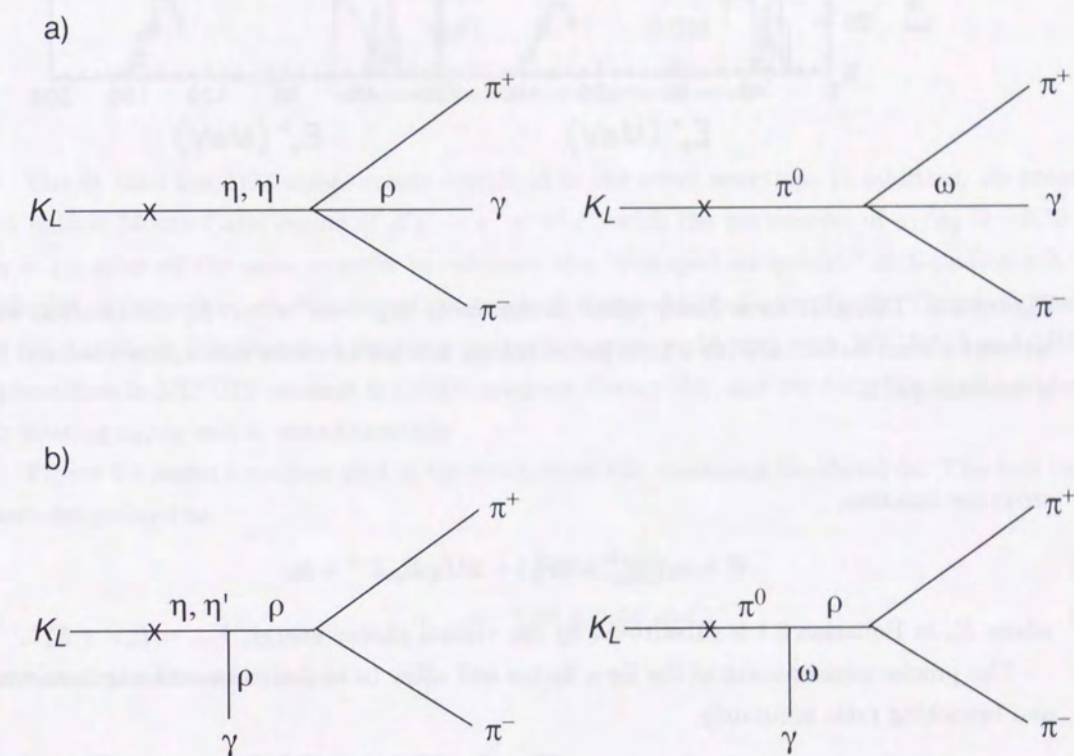


Figure 6.2: Contributions to the vector-meson intermediate model of the direct emission in the decay $K_L \rightarrow \pi^+\pi^-\gamma$: (a) contact terms and (b) pole(ρ propagator) terms [29].

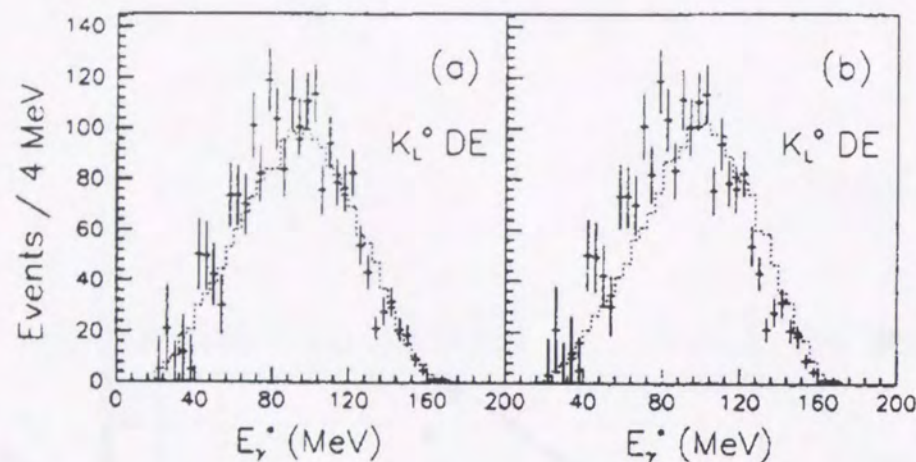


Figure 6.3: The $gM1$ form factor effect in the decay $K_L \rightarrow \pi^+\pi^-\gamma$. E_γ distribution with and without a form factor. a) With a form factor taking account of vector meson intermediate. b) With a constant $gM1$.

structure function:

$$F = a_1[(M_\rho^2 - M_K^2) + 2M_K E_{\gamma*}]^{-1} + a_2, \quad (6.2)$$

where E_γ in Equation 6.1 is substituted by the virtual photon energy, $E_{\gamma*} = E_{e^+} + E_{e^-}$.

The precise measurement of the form factor will allow us to determine the angular asymmetry and branching ratio accurately.

6.2 Maximum Likelihood Fit

In this section, we extract the constants in the form factor term, a_1/a_2 and a_1 by fitting the data event by event, using five independent variables, ϕ , $M_{\pi\pi}$, M_{ee} , $\cos\theta_{\pi^+}$, and $\cos\theta_{e^+}$. The definition of the likelihood function with floating variables ($a_1/a_2, a_1$) is

$$\ln L(a_1/a_2, a_1) = \sum_i \ln \frac{d\Gamma(\phi_i, M_{\pi\pi i}, M_{ee i}, \cos\theta_{\pi^+ i}, \cos\theta_{e^+ i}; a_1/a_2, a_1)/d\phi dM_{\pi\pi} dM_{ee} d\cos\theta_{\pi^+} d\cos\theta_{e^+}}{(\text{Averaged Acceptance}(a_1/a_2, a_1))}, \quad (6.3)$$

where $d\Gamma(\phi_i, M_{\pi\pi i}, M_{ee i}, \cos\theta_{\pi^+ i}, \cos\theta_{e^+ i}; a_1/a_2, a_1)/d\phi dM_{\pi\pi} dM_{ee} d\cos\theta_{\pi^+} d\cos\theta_{e^+}$ is a differential cross-section for the set of kinematical variables ($\phi_i, M_{\pi\pi i}, M_{ee i}, \cos\theta_{\pi^+ i}, \cos\theta_{e^+ i}$) for each event calculated with the matrix element, Equation 1.23, described in Chapter 1. "Averaged Acceptance" is an averaged overall acceptance of $K_L \rightarrow \pi^+\pi^-e^+e^-$ decay in this analysis. This

acceptance is a function of $(a_1/a_2, a_1)$, which depends on the detector, trigger, and analysis cuts. The detailed formulation and fitting procedure are explained in Appendix A. Table 6.1 lists the fixed physics parameters in the fitting.

Table 6.1: Fixed physics parameters in the maximum likelihood fit. Values are reported by the Particle Data Group(PDG) [9] and the theoretical prediction [22].

Physics parameters	values
η_{+-}	2.285×10^{-3}
Φ_{+-}	43.5°
$gE1$	0.038
gP	0.15

The fit used the 1173 signal events described in the event selection. In addition, we prepared 0.5 million Monte Carlo events of $K_L \rightarrow \pi^+\pi^-e^+e^-$ with the parameters of $a_1/a_2 = -0.70$ and $a_1 = 1.0$ after all the cuts, in order to calculate the "averaged acceptance" in Equation 6.3. For different a_1/a_2 and a_1 , the "averaged acceptance" was reweighted accordingly. The maximization of the likelihood function and the error estimation were performed with MIGRAD and MINOS subroutines in MINUIT package in CERN program library [49], and the form factor was evaluated by floating a_1/a_2 and a_1 simultaneously.

Figure 6.4 shows a contour plot of the result from the maximum likelihood fit. The best values were determined as

$$a_1/a_2 = -0.684^{+0.031}_{-0.043}(\text{stat.}) \quad (6.4)$$

$$a_1 = 1.05 \pm 0.14(\text{stat.}) \quad (6.5)$$

with statistical errors only.

6.3 Data and Monte Carlo Comparison

With the new form factor, we regenerated the Monte Carlo $K_L \rightarrow \pi^+\pi^-e^+e^-$ events and compared kinematical parameter distributions with the data. The distributions are shown in Figure 6.5. In general, data and the Monte Carlo agree well, and we concluded that the new form factor constants can reproduce the signal. Especially, the new form factor improves the agreement in $M_{\pi\pi}$ distribution between data and Monte Carlo simulation as shown in Figure 6.6.

6.4 Error on the Form Factor

We will next describe the systematic uncertainties on the form factor measurement. In this form factor measurement, the systematic uncertainties may arise from four points: 1) fitting procedure, 2) theoretical ambiguity, 3) understandings of the detectors, and 4) residual background.

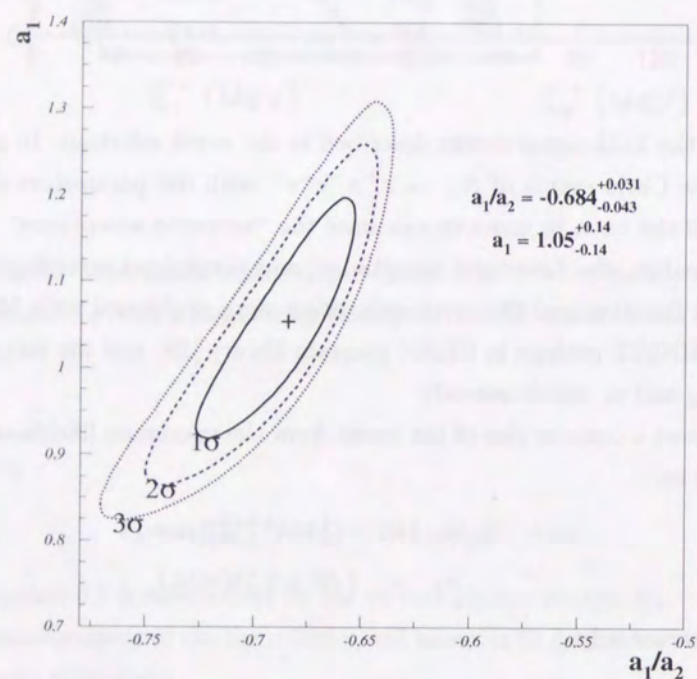


Figure 6.4: Fit result of a_1/a_2 and a_1 from two dimensional maximum likelihood method. The errors were statistical only. The statistical errors were determined with widths of the 1σ contour projection on the axes of a_1/a_2 and a_1 respectively.

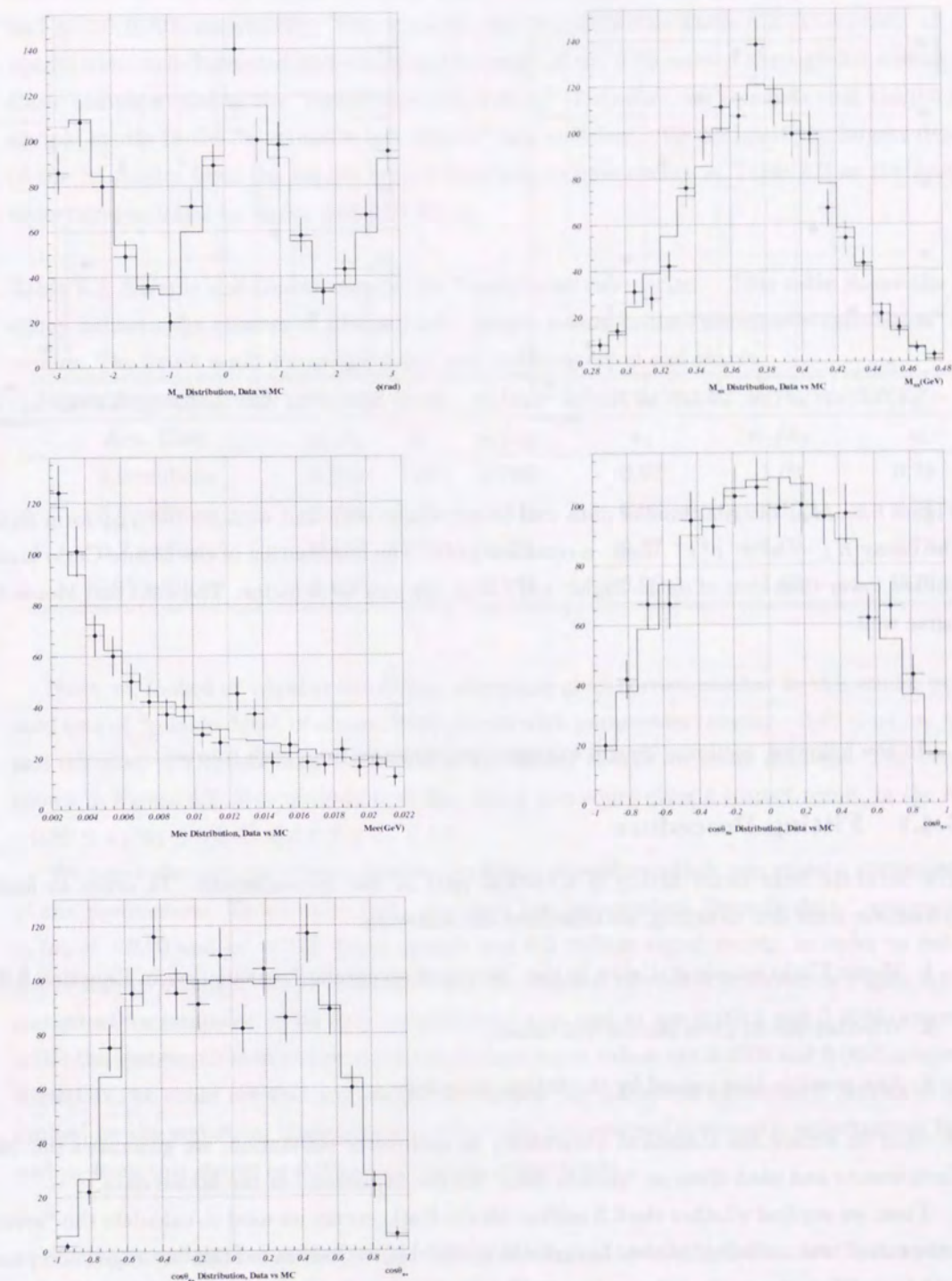


Figure 6.5: Comparison of various distributions between data and Monte Carlo. Dots represent data and solid histograms represent the Monte Carlo. These five kinematic parameters completely define a topology of the decay $K_L \rightarrow \pi^+\pi^-e^+e^-$. All parameters from data agree well with the Monte Carlo.

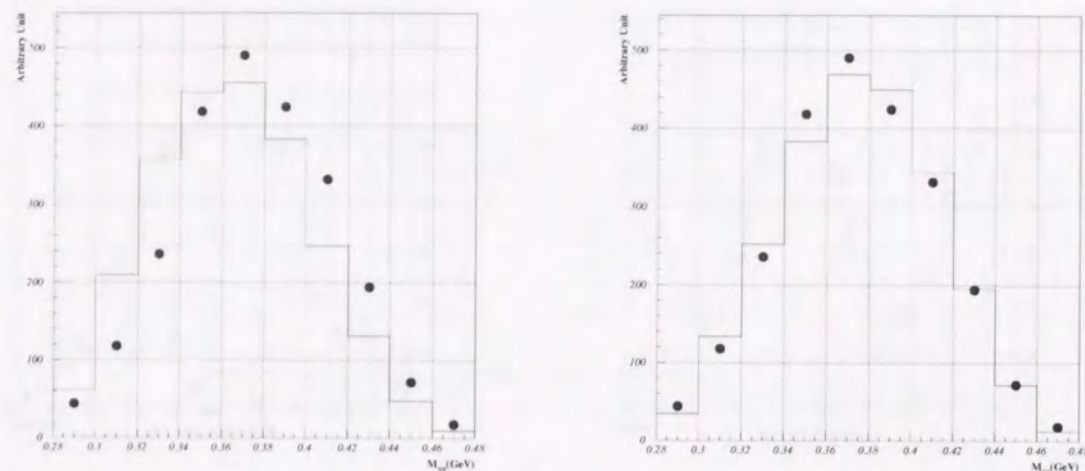


Figure 6.6: $M_{\pi\pi}$ distributions of data and Monte Carlo with and without the g_{M1} form factor in the decay $K_L \rightarrow \pi^+\pi^-e^+e^-$. Left: a constant g_{M1} . The distribution of the Monte Carlo is clearly shifted lower than that of data. Right: g_{M1} with the new form factor. The data and Monte Carlo agree well.

In the following sections, we will examine uncertainties from each source.

6.4.1 Fitting Procedure

The accurate form factor fitting is a critical part of this measurement. In order to find the systematic error due to fitting, we examined the following:

1. Monte Carlo sample statistics in the “averaged acceptance” calculation in Equation 6.3,
2. Whether the fit gives the correct values,
3. Any possible bias caused by the fitting procedure.

In order to reduce the statistical uncertainty in each error estimation, we generated the Monte Carlo events and used them as “pseudo data” for the fit, instead of the actual data.

First, we studied whether the 0.5 million Monte Carlo events we used to calculate the “averaged acceptance” was sufficient or not. In order to study this, we calculated the “averaged acceptance” with four different samples ranging from 0.05 million to 2 million events. These Monte Carlo events were generated with the parameters of $a_1/a_2 = -0.70$ and $a_1 = 1.0$. The fits were performed on the actual 1173 signal events. The fit results for a_1/a_2 and a_1 are shown in Table 6.2. In addition, in order to look at the fit accuracy, besides the actual data, we fitted two sets of “pseudo data”, which

were 25000 Monte Carlo signal events generated with the parameters of $(a_1/a_2, a_1) = (-0.70, 1.0)$ and $(-1.0, 0.70)$, respectively. These results are also shown in Table 6.2. Obviously, all the fit results were well-converged and stable in the range of the 0.05 million through 2.0 million Monte Carlo sample events in the “acceptance calculation.” Therefore, we conclude that the 0.5 million sample events in the “acceptance calculation” was sufficient. We assigned the largest deviations of the fit results from the results with 0.5 million sample events in Table 6.2 as the systematic uncertainties; 0.002 for a_1/a_2 and 0.01 for a_1 .

Table 6.2: Sample size dependency in the “acceptance calculation.” This table shows the dependency between the number of Monte Carlo sample events in the “acceptance calculation” and fit results. The fitted result for each dataset was well-converged and stable.

Inputs for pseudo data	(Actual data)	$a_1/a_2 = -0.70, a_1 = 1.0$		$a_1/a_2 = -1.0, a_1 = 0.70$	
Acc. Calc.	a_1/a_2	a_1	a_1/a_2	a_1	a_1/a_2
2.0 millions	-0.684	1.06	-0.702	0.97	-1.09
0.5 millions	-0.684	1.05	-0.703	0.97	-1.10
0.2 millions	-0.682	1.06	-0.701	0.97	-1.09
0.05 millions	-0.683	1.04	-0.703	0.96	-1.09

Next, we looked at whether the fitting procedure gives correct results. In this study, we generated sets of “pseudo data” of about 25000 events with parameters ranging $-0.80 \leq a_1/a_2 \leq -0.60$ and $0.9 \leq a_1 \leq 1.1$, and then we looked at the fitting results for those datasets. The results are shown in Figure 6.7. We conclude that the fitting procedure gives a correct result, in the range of $-0.80 \leq a_1/a_2 \leq -0.60$ and $0.9 \leq a_1 \leq 1.1$.

We also looked for an intrinsic bias in the fitting procedure which may cause a systematic offset of the parameters. To estimate this, we fitted ten independent “pseudo data,” generated with $a_1/a_2 = -0.70$ and $a_1 = 1.0$. Each sample had 0.2 million signal events, in order to reduce the statistical uncertainty. The two-dimensional distribution of results is shown in Figure 6.8. Total statistical uncertainties of the ten samples for a_1/a_2 and a_1 are 0.0013 and 0.0044, respectively, while the systematic shifts between fit results and input values are 0.0005 and 0.0026, respectively. Therefore, we could not find any fitting bias within the statistical uncertainty. Since the bias was limited by the statistical uncertainty in this study, we assigned systematic uncertainties for a_1/a_2 and a_1 from this source as 0.0013 and 0.0044, respectively.

Thus, we assigned combined errors, 0.0024 for a_1/a_2 , and 0.011 for a_1 , into systematic uncertainties from the understandings of the fit procedure.

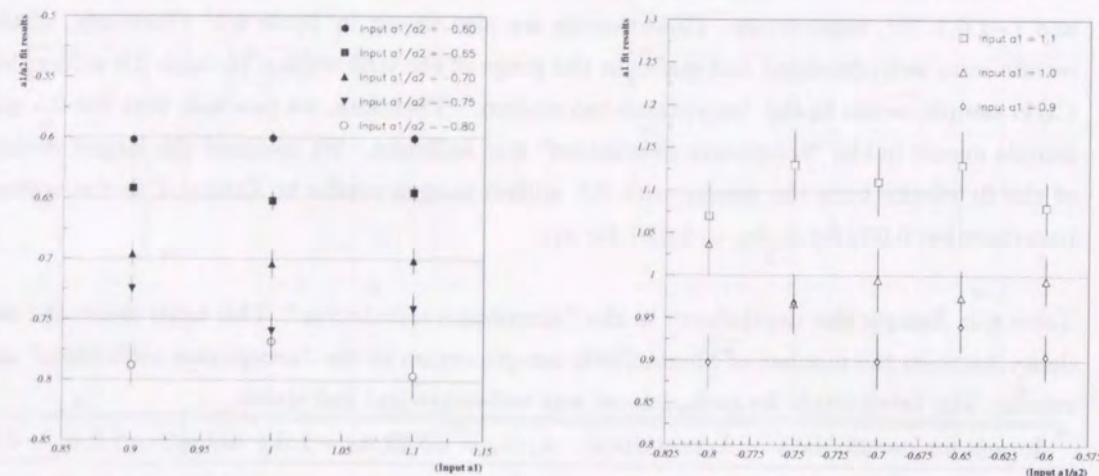


Figure 6.7: Fit results of a_1/a_2 (left plot) and a_1 (right plot) in the range of $-0.80 \leq a_1/a_2 \leq -0.60$ and $0.9 \leq a_1 \leq 1.1$. The fits gave correct results for any datasets.

6.4.2 Smearing by Detector Resolution

The smearing of any kinematic variables could occur since detectors, especially the spectrometer, had a finite precision and inefficiency. This effect could cause the deviation in the momentum and track hit position measurements(i.e., the decay topology), and give ambiguities in the fitting procedure.

In principle, the matrix element in the numerator in Equation 6.3 should be calculated with the *true* values of the five kinematic variables, whereas we could only obtain the reconstructed and smeared values from data. This means that the difference between true and reconstructed(smeared) values in the numerator may give some uncertainty.

In order to clarify this issue, we first fit a dataset of 25000 events generated by the Monte Carlo simulation, by using reconstructed variables as usual. We then fit the same dataset by using the true five variables, and looked at the difference between them.

Table 6.3: Smearing effect by detector resolution in determination of the form factor parameters. The matrix element was calculated for the same Monte Carlo dataset by using both true and reconstructed variables. The difference between the true and reconstructed variables results was small enough.

Fitted data	$a_1/a_2 = -0.70, a_1 = 1.0$		$a_1/a_2 = -1.0, a_1 = 0.70$	
	a_1/a_2	a_1	a_1/a_2	a_1
True	-0.703(16)	0.971(53)	-1.10(11)	0.743(61)
Reconstructed	-0.704(17)	0.969(53)	-1.09(11)	0.743(61)

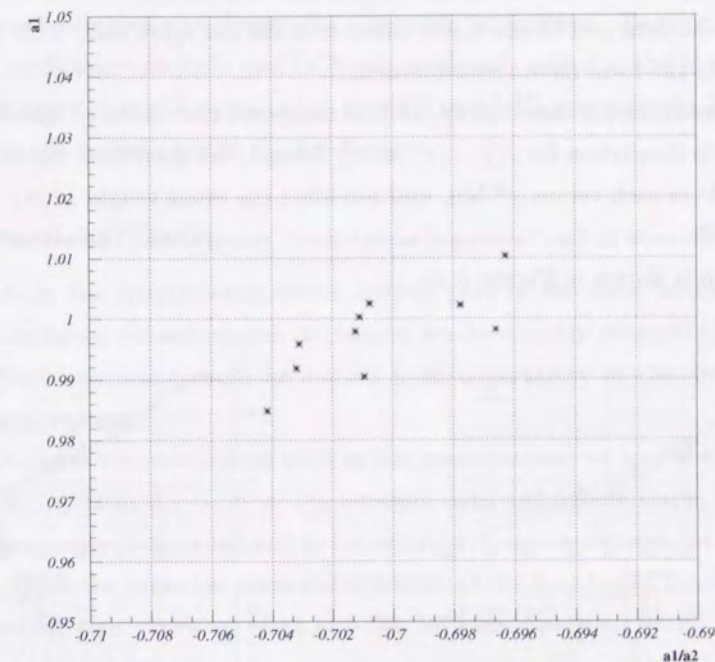


Figure 6.8: The fit results of a_1/a_2 and a_1 for the ten pseudo data samples including 0.2 million events with $a_1/a_2 = -0.70$ and $a_1 = 1.0$. Each data point represents the fit result of a_1/a_2 and a_1 . The resulting statistical uncertainties are 0.0013 for a_1/a_2 and 0.0044 for a_1 , respectively. The averages of fit results were -0.7005 for a_1/a_2 and 0.9974 for a_1 .

Table 6.3 shows the results of the fittings. In this study, we also examined two different sets of parameters in fitted dataset. The difference between the true and reconstructed variables results was very small. Hence, we conclude that the smearing effect by the detector resolution is negligible. The errors from the smearing effect were determined to be 0.001 for a_1/a_2 and 0.002 for a_1 , around the region of $a_1/a_2 = -0.7$ and $a_1 = 1.0$.

6.4.3 Vertexing Quality

The understanding of the quality of vertex reconstruction was a critical issue to determine the kinematics in $K_L \rightarrow \pi^+\pi^-\pi^0$. As shown in Figure 6.9 for $K_L \rightarrow \pi^+\pi^-\pi^0$, the distributions of vertex χ^2 of the data and Monte Carlo simulation did not agree well. This difference could cause the ambiguity in the form factor measurement.

In order to estimate the uncertainty, we first compared the vertex χ^2 distributions between data and Monte Carlo simulation for $K_L \rightarrow \pi^+\pi^-\pi^0$ decays. We then took the ratio between data and the Monte Carlo in each vertex χ^2 bin, and modified the event weight of $K_L \rightarrow \pi^+\pi^-\pi^0$ Monte Carlo by the difference in the “averaged acceptance” calculation. The vertex χ^2 distribution after the modification is shown in Figure 6.10.

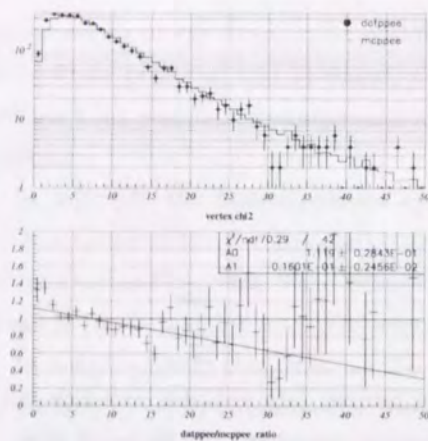


Figure 6.9: Data and Monte Carlo comparison in vertex χ^2 for $K_L \rightarrow \pi^+\pi^-\pi^0$. Top plot shows the overlay of data(dots) and Monte Carlo(histogram). Bottom shows the data to Monte Carlo ratio. The same effect was observed in the decay $K_L \rightarrow \pi^+\pi^-\pi^0$.

By using the modified weight, we obtained the fit result of $a_1/a_2 = -0.686 \pm 0.036$ and $a_1 = 1.04 \pm 0.14$. Therefore, we assigned systematic errors of 0.3 % for a_1/a_2 and 1.0 % for a_1 to the uncertainty in the understanding of vertex χ^2 distribution.

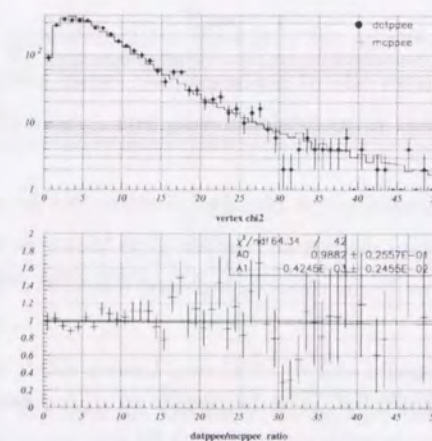


Figure 6.10: Data and the modified Monte Carlo comparison in vertex χ^2 for $K_L \rightarrow \pi^+\pi^-\pi^0$. The modification was performed with event weights evaluated from the comparison between data and the Monte Carlo of $K_L \rightarrow \pi^+\pi^-\pi^0$.

6.4.4 Drift Chamber Inefficiency

As shown in Figure 6.11, the M_{ee} distribution originated from a virtual photon was well simulated in $K_L \rightarrow \pi^+\pi^-\pi^0$. This is a supporting evidence that the chamber response for closed two electron tracks was well understood. However, although track illumination in the chamber matched between data and the Monte Carlo in most of the regions, there is a small discrepancy in the neutral beam regions of DC1 and DC2, as shown in Figure 6.12. This was caused by a surplus in higher side in the drift chamber SOD distribution in data, which lead to extra loss. The higher tail is thought to be caused by the radiation damage on the sense wires which lowered the gain.

In the form factor measurement, the inefficiency may cause the acceptance deficit in some charged track configurations and change the kinematic parameters. To estimate uncertainty from this source, the inefficiency for DC1 and DC2 was artificially added to the Monte Carlo simulation. Adding 5% inefficiency changed a_1/a_2 and a_1 by 0.3% and 0.6%, respectively. Hence, we determined them as a systematic uncertainty in the tracking.

6.4.5 Momentum Scale

Momentum scale in the spectrometer was a critical part in the form factor measurement, since the accurate momentum reconstruction of charged tracks directly changed the topology of $K_L \rightarrow \pi^+\pi^-\pi^0$. This uncertainty could be caused from uncertainty in the detector alignment and magnet field measurement.

In order to evaluate the momentum scale in the spectrometer, we looked at the difference in the distribution of $M_{\pi\pi ee}$ from $K_L \rightarrow \pi^+\pi^-\pi^0$ between data and Monte Carlo, since the error in the momentum measurement is proportional to the error in the measurement of $(M_{\pi\pi ee} - 2M_\pi - 2M_e)$.

Figure 6.13 shows the invariant mass distributions of the four tracks for data and Monte Carlo simulation. The difference between data and the MC was less than 0.01% in mean value of the distributions.

In addition, Figure 6.14 shows the averaged $M_{\pi\pi}$ as a function of $(E_{\pi 1} + E_{\pi 2})$ for $K_L \rightarrow \pi^+\pi^-\pi^0$ data and Monte Carlo simulation, in order to evaluate the momentum dependency. The error in the momentum measurement is also proportional to the error of $(M_{\pi\pi} - 2M_\pi)$. A drop in $M_{\pi\pi}$ lower energy region is caused by the detector acceptance. The ratio was perfectly flat in the whole region.

Therefore, we conclude that the fluctuation from the momentum scale was negligible.

6.4.6 Physics Input Parameter

In this study, the physics parameters in the matrix element calculation were taken from Ref. [9], which have their own errors. The deviations of such parameters may vary the fit results. In order to evaluate this effect, we produced “pseudo data” of 25000 events by independently varying the physics parameter, η_{+-} , Φ_{+-} , $gE1$ and gP , within a reasonable range, and fitted those datasets. For η_{+-} , Φ_{+-} , we independently varied the values within $\pm 1\sigma$, quoted in Ref. [9]. For $gE1$, there

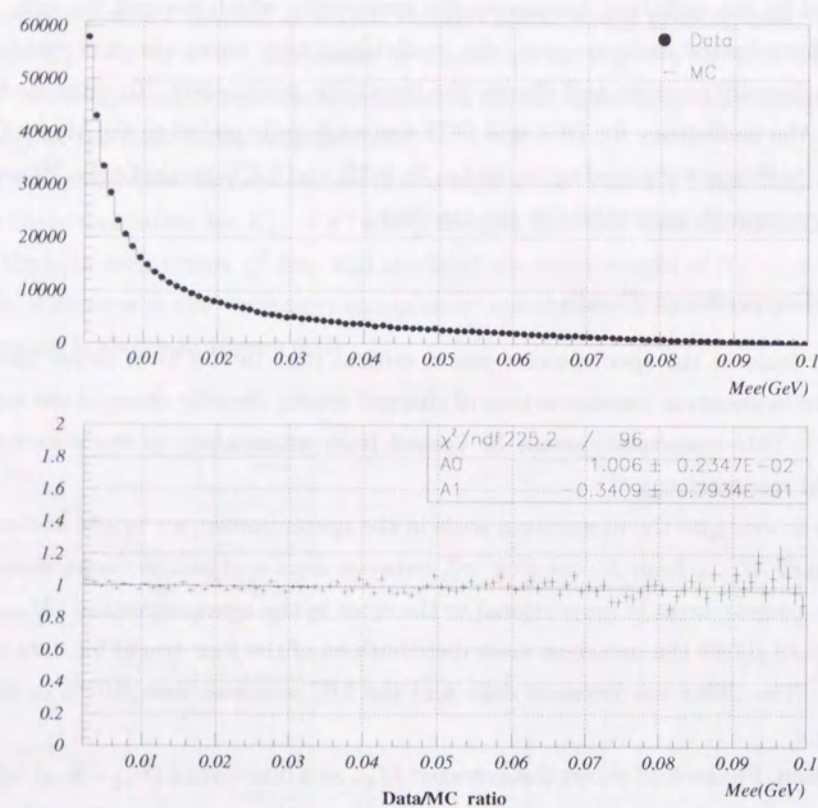


Figure 6.11: Data and Monte Carlo comparison for M_{ee} distributions in the decay $K_L \rightarrow \pi^+\pi^-\pi_D^0$. Upper plot shows the M_{ee} distributions of data(dots) and Monte Carlo(histogram) in the decay $K_L \rightarrow \pi^+\pi^-\pi_D^0$. Lower plot shows the data to Monte Carlo ratio. The distribution of the Monte Carlo agreed well with that of data in a whole distribution.

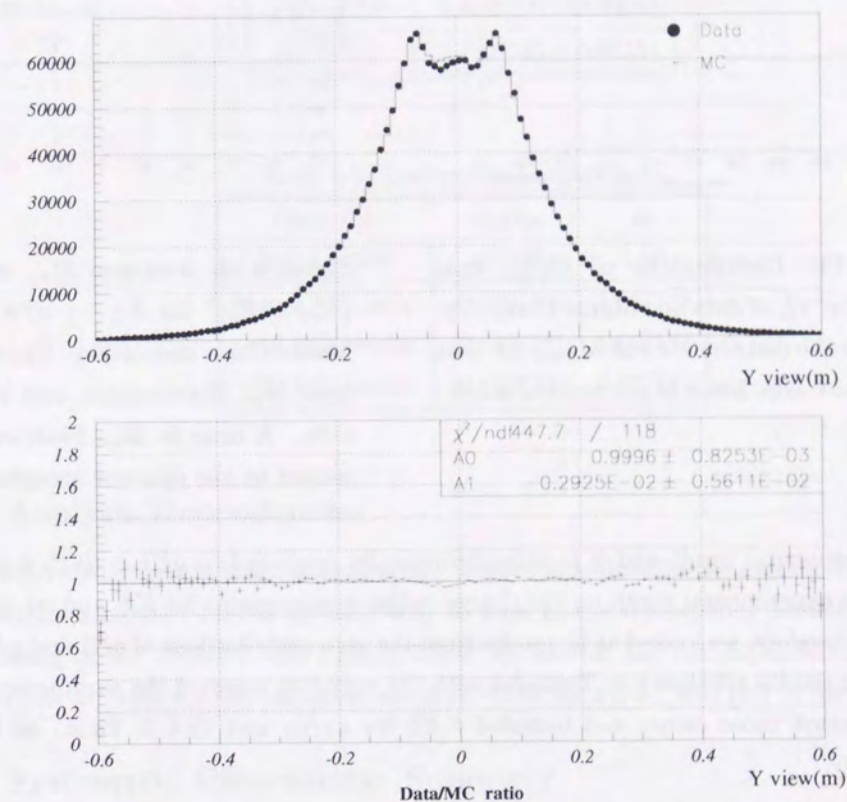


Figure 6.12: Data and Monte Carlo comparison of track illumination at DC1 in Y view. Upper plot shows the comparison between data(dots) and Monte Carlo(histogram) of the track illumination. Lower is the data to Monte Carlo ratio. There is small inefficiency in neutral beam region($|Y| < 0.05\text{m}$).

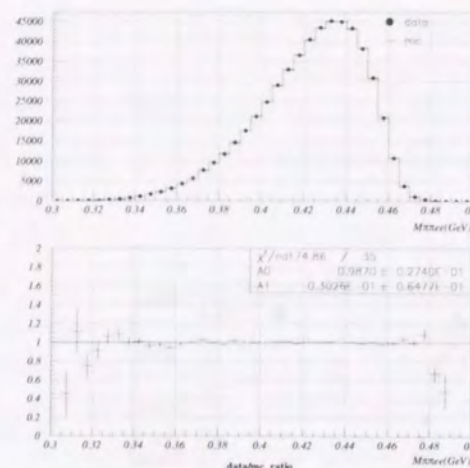


Figure 6.13: Distributions of $M_{\pi\pi ee}$ from $K_L \rightarrow \pi^+\pi^-\pi_D^0$ of data and Monte Carlo. Upper plot is the distributions of $M_{\pi\pi ee}$ for data and Monte Carlo, lower is the ratio of them.

is no experimental result and it is only theoretically predicted as $gE1 < (0.15 \times gM1)$. For gP , there is no experimental result on the charge radius measurement for K^0 , and no valid calculation on this. Therefore, we looked at fit results from the zero contributions of $gE1$ and gP , respectively.

Fitting results are shown in Table 6.4 with the variation range of the parameters. We quadratically summed those errors and included 6.4% for a_1/a_2 and 12.4 % for a_1 as the systematic uncertainty.

6.4.7 Background Uncertainty

In this study, we have assumed the background level is ignorable since the signal to background ratio is expected to be about 100. To confirm this, we also tested the contribution from background uncertainty. We made a dataset with 1173 Monte Carlo signal events, and added 0, 12, and 23 background events from $K_L \rightarrow \pi^+\pi^-\pi_D^0$ Monte Carlo events surviving all the analysis cuts. Table 6.5 shows the variation of the parameters obtained by the fit. The shift caused by the background is comparable to the statistical error from the additional 12 events, 0.006 for a_1/a_2 , and 0.05 for a_1 . Therefore, we include 0.006 for a_1/a_2 and 0.05 for a_1 as systematic uncertainties.

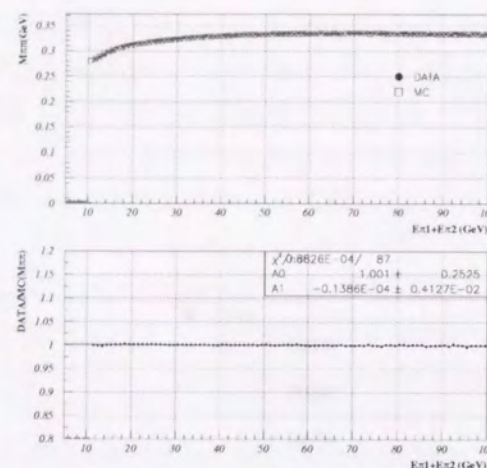


Figure 6.14: Averaged $M_{\pi\pi}$ as a function of $(E_{\pi 1} + E_{\pi 2})$ for $K_L \rightarrow \pi^+\pi^-\pi_D^0$ data and Monte Carlo simulation. Upper plot is averaged $M_{\pi\pi}$ distributions, and lower shows the ratio. A drop in $M_{\pi\pi}$ lower energy region is caused by the detector acceptance.

Table 6.4: Stability to parameter fluctuations.

Variation	a_1/a_2	a_1
Input value	-0.700	1.00
$\eta_{+-} + 1\sigma$	-0.714(17)	0.98(5)
$\eta_{+-} - 1\sigma$	-0.685(17)	1.03(5)
$\Phi_{+-} + 1\sigma$	-0.705(17)	1.08(5)
$\Phi_{+-} - 1\sigma$	-0.709(17)	0.98(5)
$gE1 = 0.0$	-0.692(17)	0.94(5)
$gP = 0.0$	-0.744(22)	0.87(5)

Table 6.5: Background uncertainty

Data set	a_1/a_2	a_1
Input value	-0.700	1.00
Signal MC only	-0.694(39)	1.05(14)
+12 BG events	-0.688(38)	1.00(14)
+23 BG events	-0.690(38)	0.97(14)

6.4.8 Analysis Dependencies

The cut dependency in any kinematic variables is often examined in the systematic study of high-energy physics analysis. This is an easy way to look at the discrepancy between data and our understanding of the detector and signal. Here, we exhibit the cut dependencies for the form factor analysis in Table 6.6. We assigned errors of 4.2 % for a_1/a_2 , and 11.7 % for a_1 , respectively.

6.4.9 Systematic Uncertainty: Summary

So far, we evaluated the systematic uncertainties from various sources. We summarize the systematic uncertainties in Table 6.7.

6.5 Form Factor Measurement: Summary

We conclude that the form factors for $K_L \rightarrow \pi^+\pi^-e^+e^-$ are

$$\begin{aligned} a_1/a_2 &= -0.684^{+0.031}_{-0.043}(\text{stat.}) \pm 0.053(\text{syst.}) \\ a_1 &= 1.05 \pm 0.14(\text{stat.}) \pm 0.18(\text{syst.}). \end{aligned}$$

Table 6.6: Deviations of analysis cut dependencies.

Cut	a_1/a_2	a_1	Variation
Z vertex	0.6%	1.2%	$110m < Z < 154m$
Cluster Threshold	0.3%	2.4%	Shift HCC threshold
M_{ee} cut	3.8%	8.5%	$M_{ee} > 2.0 - 4.0 \text{ MeV}/c^2$
$M_{\pi\pi ee}$ cut	1.2%	4.7%	$\pm 6.0 - \pm 14.0 \text{ MeV}/c^2$
Pp0kine cut	0.3%	3.8%	$-0.0025 - -0.075 \text{ MeV}^2/c^2$
E/p cut	0.3%	0.9%	$\pm 0.06 - \pm 0.10$
p_t^2 cut	0.9%	4.5%	$p_t^2 < 30 - 60 \text{ MeV}^2/c^2$
Total	4.2 %	11.7%	

Table 6.7: Systematic uncertainties.

Sources	a_1/a_2	a_1
Fit procedure	0.35%	1.0 %
Detector smearing	0.1%	0.2 %
Vertex quality	0.3%	1.0 %
DC ineff.	0.3%	0.6 %
Input Param.	6.4%	12.4 %
BG subtraction	1.5%	4.8 %
Analysis dep.	4.2%	11.7 %
Total	7.8%	17.8 %

Chapter 7

Asymmetry Measurement

As described in Chapter 1, CP violation in $K_L \rightarrow \pi^+\pi^-e^+e^-$ arises from the interference of the CP conserving direct emission(DE) and CP violating inner bremsstrahlung(IB) of $K_L \rightarrow \pi^+\pi^-\gamma^*$, resulting in the angular asymmetry between normals to $\pi^+\pi^-$ and e^+e^- decay planes.

An asymmetry between the number of events observed in particular angle regions may differ from the theoretically predicted asymmetry, because the measured asymmetry depends on the detector, trigger and analysis acceptances. Therefore, the asymmetry should be corrected for the acceptance. We will work on different levels of asymmetries in this thesis, so we clarify a terminology of these asymmetries here.

- *Intrinsic Asymmetry*: True asymmetry defined by the nature. This is what we have pursued to measure from data and compare to the theoretical prediction. The *intrinsic asymmetry* is given *a priori*.
- *Input Asymmetry*: Input value of the asymmetry into the Monte Carlo event generator. In principle, the *input asymmetry* is equivalent to the *intrinsic asymmetry* but it was given by us.
- *Raw Asymmetry*: Measured asymmetry with the KTeV detector and certain analysis cuts. The *raw asymmetry* is not equal to the *intrinsic* and *input asymmetry* since the detector and analysis acceptance affect on the distributions of kinematic variables related to the asymmetry. Therefore, the *raw asymmetry* is a KTeV- and analysis-specific variable.
- *Acceptance Corrected Asymmetry*: Asymmetry of reconstructed events after correcting for the acceptance. The acceptance correction was done by the Monte Carlo simulation. The *acceptance corrected asymmetry* is directly comparable to the *intrinsic* and *input asymmetries*.

In this chapter, we first explain the *raw asymmetry* measurement, and clarify its origin. Next, we show how the acceptance correction was done to estimate the *acceptance corrected asymmetry*. Finally, we summarize the systematic uncertainties in this study.

7.1 Raw Asymmetry

7.1.1 Raw Asymmetry Calculation

First we start by the definition of *raw asymmetry* in this asymmetry study. The *raw asymmetry* was defined as a simple counting asymmetry of ϕ distribution. Figure 7.1 is ϕ distribution of data and Monte Carlo, after applying all the cuts as explained in Chapter 5. Dots are from data while a solid histogram is from $K_L \rightarrow \pi^+\pi^-e^+e^-$, with *input asymmetry* of 0.14. The *raw asymmetry* is calculated by

$$Asym. = \frac{N_{I,III} - N_{II,IV}}{N_{I,III} + N_{II,IV}}, \quad (7.1)$$

where N_i corresponds the number of events in I, II, III , and IV angular quadrants in the plot. The asymmetry becomes more apparent when they are shown in $2 \cos \phi \sin \phi$ instead of ϕ , as shown in Figure 7.2. Regions of I and III in Figure 7.1 correspond to $\sin \phi \cos \phi > 0$ region, while II and IV correspond to $\sin \phi \cos \phi < 0$ region. Therefore, the raw asymmetry was evaluated from the positive-negative asymmetry in $\sin \phi \cos \phi$ distribution:

$$Asym. = \frac{N_{\sin \phi \cos \phi > 0} - N_{\sin \phi \cos \phi < 0}}{N_{\sin \phi \cos \phi > 0} + N_{\sin \phi \cos \phi < 0}}. \quad (7.2)$$

The asymmetries defined here are clearly observed in Figure 7.1 and 7.2.

Of the 1173 events observed in our analysis(Chapter 5), 719 events were observed in $\sin \phi \cos \phi > 0$ region, and 454 events were observed in $\sin \phi \cos \phi < 0$ region. The resulting *raw asymmetry* calculated with Equation 7.2 was:

$$Asym. = 0.237 \pm 0.029(stat.), \quad (7.3)$$

with statistical error only. Note that this asymmetry is not directly comparable to the theoretical prediction, as mentioned before. For example, $K_L \rightarrow \pi^+\pi^-e^+e^-$ Monte Carlo events generated with the *input asymmetry* of 0.147 gave the *raw asymmetry* of 0.258. This implies that there is a mechanism to enhance the asymmetry, or some systematic bias in the asymmetry measurement. Hence, the origin of this discrepancy will be examined in the following sections. After this issue is cleared, we will move on to the acceptance correction on this *raw asymmetry* to obtain the *acceptance corrected asymmetry*.

7.1.2 Bias from Detector and Event Selection

Before proceeding to the acceptance correction for the *raw asymmetry*, we verify that the *raw asymmetry* actually came from the *intrinsic asymmetry* in $K_L \rightarrow \pi^+\pi^-e^+e^-$ kinematics, and not from the detector alignment or analysis cuts. If the asymmetry is caused by detector misalignment or analysis cuts, the asymmetry will also be possibly introduced to other decay modes with similar decay topology.

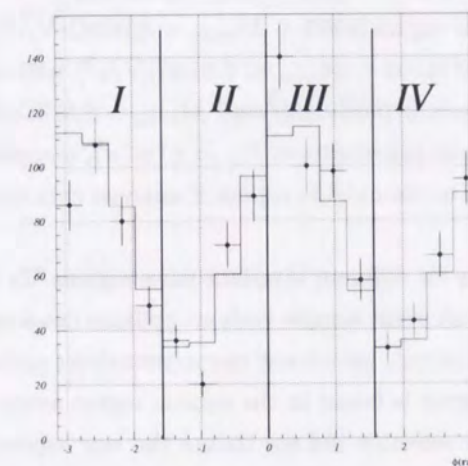


Figure 7.1: ϕ distribution of data, overlaid with the Monte Carlo. Dots are from data while a histogram is from $K_L \rightarrow \pi^+\pi^-e^+e^-$ Monte Carlo with the *input asymmetry* of 0.14. Cuts were applied to data and Monte Carlo, as explained in Chapter 5. The *raw asymmetry* was calculated from $(N_{I,III} - N_{II,IV})/(N_{I,III} + N_{II,IV})$, where N_i corresponds the number of events in quadrants I, II, III , and IV .

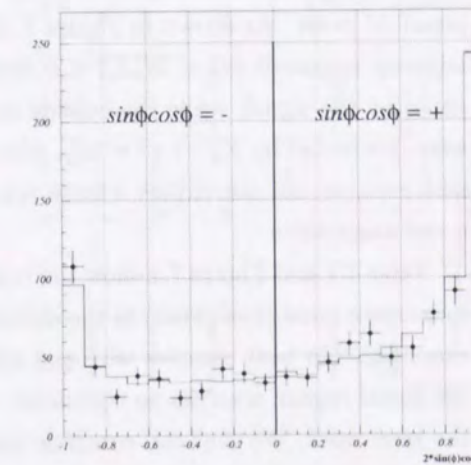


Figure 7.2: Distribution of $(2 \cos \phi \sin \phi)$ from data, overlaid with the Monte Carlo. Dots are from data while a histogram is from $K_L \rightarrow \pi^+\pi^-e^+e^-$ Monte Carlo. The quadrants I and III in Figure 7.1 correspond to $2 \sin \phi \cos \phi > 0$, while the quadrants II and IV in Figure 7.1 correspond to $2 \sin \phi \cos \phi < 0$. The asymmetry is more apparent in this plot.

First, we examine the *raw asymmetry* in the decay $K_L \rightarrow \pi^+\pi^-\pi_D^0$, since its decay topology is similar to the signal mode, and there is no correlation between decay planes of $\pi^+\pi^-$ and e^+e^- from π_D^0 decay. Moreover, this mode had enough events to detect a small amount of the asymmetry in the measurement. Figure 7.3 shows the ϕ distribution in the $\pi^+\pi^-e^+e^-$ center-of-mass frame from data sample of 1 million events, positively identified as $K_L \rightarrow \pi^+\pi^-\pi_D^0$. The *raw asymmetry* of this mode was calculated to be -0.00018 ± 0.00051 . It is consistent with zero *raw asymmetry* with a very good precision. This means that any *raw asymmetry* induced by the detector or event selection is negligible.

We also looked at the asymmetry for events inside or outside of the signal region in $\pi^+\pi^-e^+e^-$ invariant mass. As shown in Figure 5.12, the signal region ($0.493 < M_{\pi\pi ee} < 0.503 \text{ GeV}/c^2$) and adjacent regions ($0.483 < M_{\pi\pi ee} < 0.493 \text{ GeV}/c^2$ and $0.503 < M_{\pi\pi ee} < 0.513 \text{ GeV}/c^2$) were dominated by the signal, while the outside regions ($M_{\pi\pi ee} < 0.483 \text{ GeV}/c^2$ and $M_{\pi\pi ee} > 0.513 \text{ GeV}/c^2$) were dominated by $K_L \rightarrow \pi^+\pi^-\pi_D^0$. Since the *intrinsic asymmetry* of $K_L \rightarrow \pi^+\pi^-\pi_D^0$ is consistent with zero, we can also expect a finite *raw asymmetry* in the outside regions if analysis cuts induced a *raw asymmetry*.

Table 7.1 and Figure 7.4 show the *raw asymmetry* for different invariant mass regions. In order to increase number of events in the sideband region, an event sample without pp0kine cut was also examined. For both samples with and without pp0kine cut, prominent *raw asymmetries* appear in the signal region, whereas no significant raw asymmetry is found in the outside region away from the kaon mass. We thus can conclude that the event selection did not induce the *raw asymmetry*.

From above studies, we conclude that both detector and event selection do not spontaneously cause a finite *raw asymmetry* from samples with zero *intrinsic asymmetry*. In the next section, we will support this argument by a Monte Carlo study.

Table 7.1: *Raw asymmetries* at different mass regions. In our study, signal region was defined as $0.493 < M_{\pi\pi ee} < 0.503 \text{ GeV}/c^2$. To increase number of events in the sideband region, a event sample without pp0kine cut was also examined. No significant asymmetry appeared in the outside region, in contrast to the signal region and its adjacent region.

Invariant Mass Region(GeV/c^2)	Raw Asym.	Raw Asym.(without pp0kine cut)	Description
< 0.473	0.0066 ± 0.048	0.0027 ± 0.0051	outside
$0.473 - 0.483$	0.25 ± 0.15	0.0027 ± 0.031	outside
$0.483 - 0.493$	0.35 ± 0.11	0.077 ± 0.034	adjacent
$0.493 - 0.503$	0.237 ± 0.029	0.185 ± 0.025	signal
$0.503 - 0.513$	0.0 ± 0.21	0.15 ± 0.19	adjacent
> 0.513	-0.063 ± 0.18	0.0 ± 0.16	outside

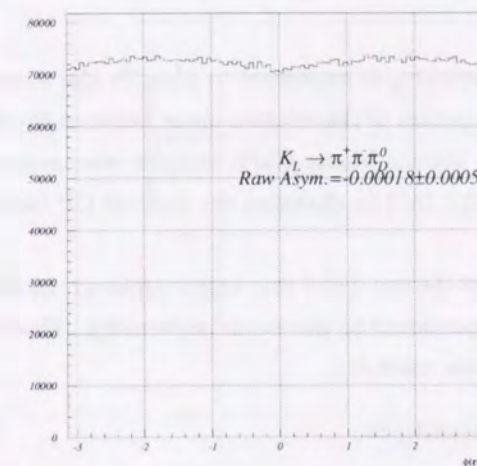


Figure 7.3: ϕ distribution of identified $K_L \rightarrow \pi^+\pi^-\pi_D^0$. The cuts for the normalization was applied to collect events. The ϕ asymmetry is equal to zero with a very good precision, so that the detector-induced asymmetry was negligible.

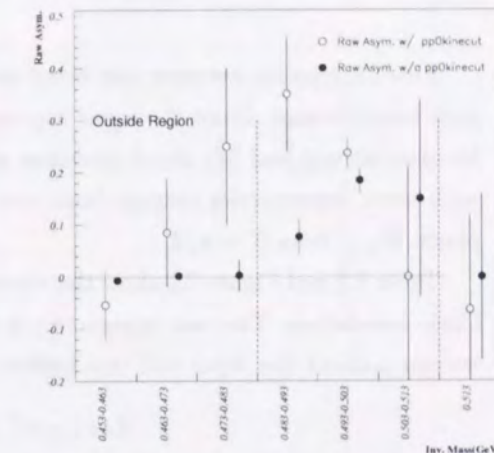


Figure 7.4: *Raw asymmetries* at different mass regions. In our study, the signal region was defined within $0.493 < M_{\pi\pi ee} < 0.503 \text{ GeV}/c^2$ while the outside regions were defined as $M_{\pi\pi ee} < 0.483 \text{ GeV}/c^2$ and $M_{\pi\pi ee} > 0.513 \text{ GeV}/c^2$. To increase number of events in the sideband regions, a event sample without pp0kine cut was also examined. No significant asymmetry was found in the outside region, in contrast to the signal region. In signal region, because of background contamination, the *raw asymmetry* is diluted for the event set without Pp0kine cut.

7.1.3 Origin of Raw Asymmetry

So far, we have considered a source of the *raw asymmetry* other than the *intrinsic asymmetry*, and concluded that the *raw asymmetry* is not caused by systematic uncertainties such as the detector misplacement or event selection. Here, we turn to look at the behavior of the *raw asymmetry* and the reason why the asymmetry is enhanced by the measurement. We will use the Monte Carlo simulation of $K_L \rightarrow \pi^+ \pi^- e^+ e^-$, since it can reveal the relation between the *input* and *raw asymmetry*, and it allows us to do a detailed study on the kinematical acceptance.

First, a relation between the *input* and *raw asymmetry* is examined to identify the source of such enhancement. Since the *input asymmetry* is a function of the relative phase between the inner bremsstrahlung and M1 direct emission amplitudes, various Monte Carlo samples were generated with *input asymmetries* ranging from zero to nominal(0.147) by changing the indirect CP violating phase, Φ_{+-} , from 0 to $\pi/4$.

Table 7.2 and Figure 7.5 show the relation between the *input* and *raw asymmetries* in the Monte Carlo simulation. The *raw asymmetry* is nearly proportional to the *input asymmetry*. Therefore, we can connect the *input* and *raw asymmetry* with one constant;

$$\text{RawAsym.} = 1.75 \times \text{InputAsym.} \quad (7.4)$$

The coefficient greater than 1 indicates the *raw asymmetry* is enhanced than the *input asymmetry*. Also, since there is no offset to this linear relationship, it supports that the *raw asymmetry* is produced by the *input asymmetry*.

Table 7.2: Comparison between the *input* and *raw asymmetry*. The all analysis cuts were applied to Monte Carlo data samples. Errors are statistical only. The result means that the *raw asymmetry* is an enhancement of the *input asymmetry*.

Input Asymmetry	Raw Asymmetry
-0.048	-0.085 ± 0.0060
-0.00215	-0.00933 ± 0.0060
0.022	0.051 ± 0.0060
0.047	0.077 ± 0.0059
0.070	0.128 ± 0.0059
0.090	0.146 ± 0.0068
0.124	0.212 ± 0.0068
0.146	0.245 ± 0.0067
0.147	0.258 ± 0.0067
0.153	0.260 ± 0.0066

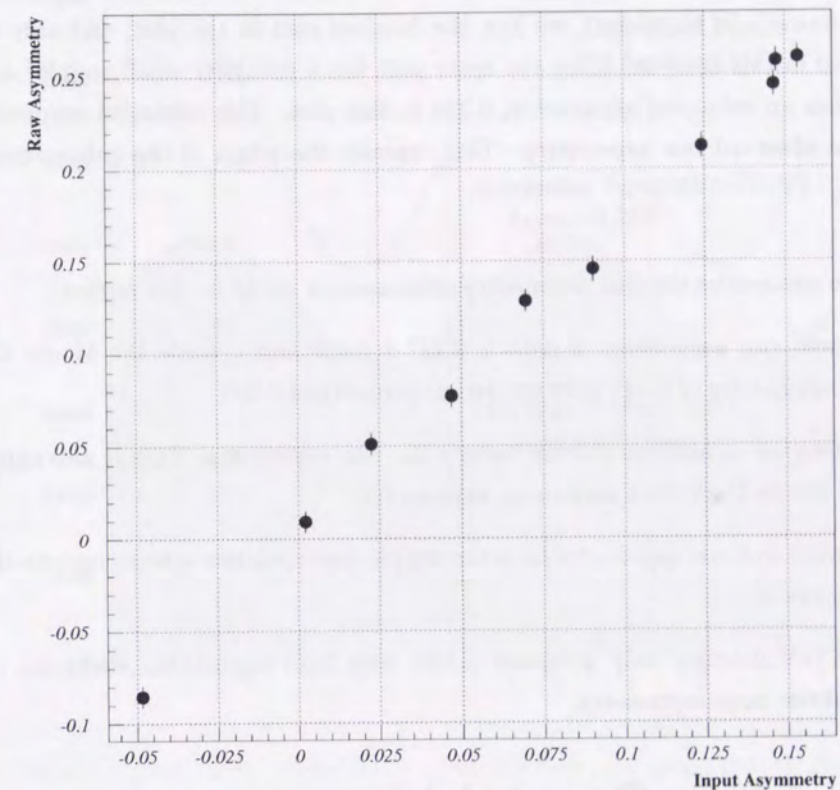


Figure 7.5: Relation between the *input* and *raw asymmetry*. The *raw asymmetry* is almost proportional to the *input asymmetry*.

Next, we explore why the *raw asymmetry* is enhanced than the *input asymmetry*.

The KTeV detector was not sensitive to low momentum charged particles, especially the momentum less than 2 GeV/c in the lab frame. This was because the analysis magnet in the spectrometer kicked out those low momentum charged particles. Such particles were mostly electrons since electrons had relatively small momenta. In this analysis, we lost approximately 70% of signal events by this reason.

Figure 7.6 shows the situation. The open histogram is a ϕ distribution of $K_L \rightarrow \pi^+\pi^-e^+e^-$ Monte Carlo, before any detector, trigger, or analysis cuts. The hatched histogram is the distribution of Monte Carlo events which has at least one low momentum electron with less than 2 GeV/c in the lab frame. As mentioned, we lost the hatched part in the plot, and only the remainder was accepted in this analysis. Since the lower part has a relatively small angular asymmetry, the remaining has an enhanced asymmetry, 0.229 in this plot. This enhanced asymmetry is comparable to the observed *raw asymmetry*. This explains the origin of the enhancement in the *raw asymmetry*.

Here, we summarize the *raw asymmetry* enhancement study in this section:

- Measured *raw asymmetry* of data is $0.237 \pm 0.029(stat.)$, while the Monte Carlo with the *input asymmetry* of 0.147 gave the *raw asymmetry* of 0.258.
- The detector or analysis did not induce the *raw asymmetry*. This is also supported by the signal Monte Carlo with zero input asymmetry.
- The *input* and *raw asymmetry* have the simple linear relation which suggests the asymmetry enhancement.
- The KTeV detector only accepted events with high momentum electrons. Those events showed the large asymmetry.

7.2 Acceptance Corrected Asymmetry

In this section, we describe the measurement of the *acceptance corrected asymmetry*. Since the *acceptance corrected asymmetry* is evaluated by converting the *raw asymmetry* as described before, we discuss the acceptance correction first. Then, the *acceptance corrected asymmetry* is examined.

In Section 7.1, we showed that the *raw asymmetry* is enhanced because the events with low momenta which have a smaller asymmetry are lost by the detector acceptance. In actual measurement of the data, we have to make the acceptance correction with a proper Monte Carlo simulation to evaluate the *acceptance corrected asymmetry*. The acceptance correction was done in the following steps:

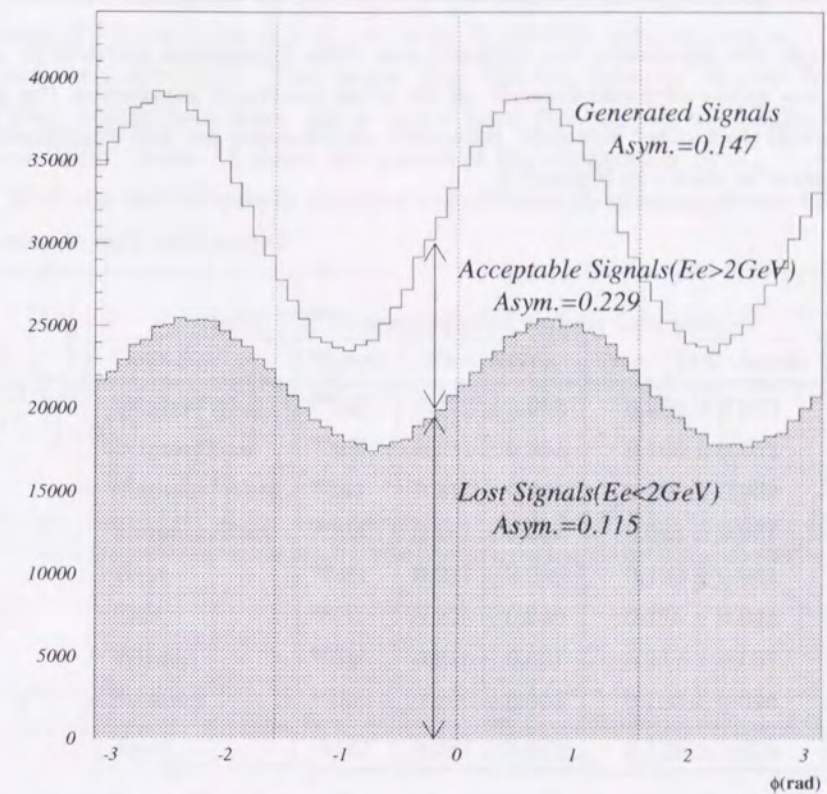


Figure 7.6: Distributions of $K_L \rightarrow \pi^+\pi^-e^+e^-$ with respect to ϕ . The open histogram shows generated signals with *input asymmetry* of 0.147, before any detector, trigger or analysis cuts. The hatched histogram is the generated events which has at least one electron with momentum less than 2 GeV/c in the lab frame. In our analysis, we lost all of the hatched region, and we only accept the remainder, which have the *raw asymmetry* of 0.229. This is considered to be the origin of the enhancement in the *raw asymmetry*.

1. Make ϕ distribution of the signal, and divide it into 32 bins.
2. Evaluate acceptances for each bin, by comparing the number of generated events and accepted events after all the analysis cuts using the Monte Carlo simulation.
3. Make an acceptance correction to the ϕ distribution from data bin by bin by using the acceptances calculated in 2.
4. Calculate the *acceptance corrected asymmetry* from the acceptance corrected ϕ distribution.

In this method, the acceptance was averaged over other kinematical variables in each ϕ bin. Although the *raw asymmetry* also depends on the other kinematic parameters, the averaged acceptance works well since other kinematic parameter distributions are well reproduced by the Monte Carlo simulation as shown in Figure 6.5.

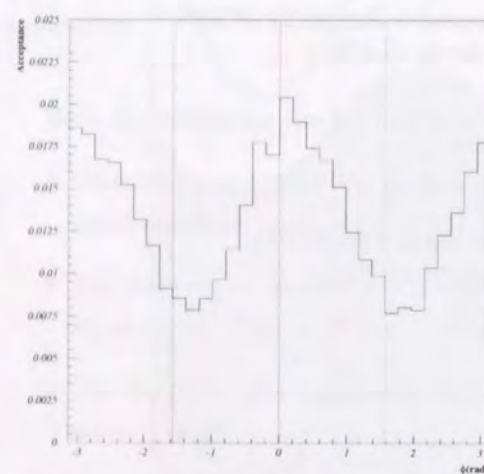


Figure 7.7: Signal acceptance as a function of ϕ . In this plot, we can observe a small shift of peaks and valleys from the origin. This is originated from the inefficiency in the low momentum electron, as described in Section 7.1.3.

Figure 7.7 shows the acceptance as a function of ϕ in the Monte Carlo simulation. In the plot, we can observe a small shift in peaks and valleys from $\pi/2 \times n$. This originated from the inefficiency in the low momentum electron, as described in Section 7.1.3. With this set of acceptances, we applied the acceptance correction to the ϕ distribution of the signal events. The result of this acceptance correction is shown in Figure 7.8. Dots show the number of events after the acceptance correction, while the histogram shows the Monte Carlo distribution with the input asymmetry of 0.147. The ϕ distribution from the Monte Carlo agree well with that of data. We obtained the *acceptance corrected asymmetry* of 0.127 ± 0.029 .

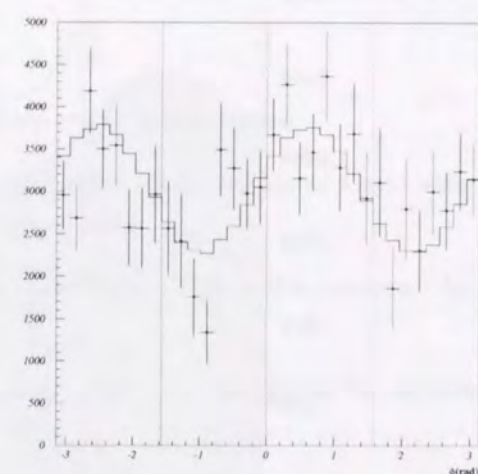


Figure 7.8: The ϕ distribution of acceptance corrected data. Dots represent the *acceptance corrected asymmetry* from data, while the histogram shows the the Monte Carlo events with *input asymmetry* of 0.147.

We can cross check this value by using the linear relation between *input asymmetry* and *raw asymmetry* in Section 7.1.3. By dividing the *raw asymmetry* by the linear slope of 1.75, we obtained 0.135 ± 0.029 . Since these two estimations are consistent to each other, we certify that the acceptance correction is a proper procedure to extract the *acceptance corrected asymmetry*.

Therefore, we conclude that the *acceptance corrected asymmetry* is measured to be 0.127 ± 0.029 .

As a consistency check, we divide the signal into several event sets. In this study, we used two neutral beams of +X(west) side and -X(east) side. In addition, we took data in '97 winter(Jan.~Mar.) and '97 Summer(July~Aug.). This makes four different datasets, Winter/West, Winter/East, Summer/West, and Summer/East. We looked at these data samples to examine the beam and run period dependency. Table 7.3 shows the results of the asymmetries in $K_L \rightarrow \pi^+\pi^-e^+e^-$ of four datasets. Both *raw* and *acceptance corrected asymmetries* show no significant divergence from the nominal value in each data sample.

Table 7.3: Asymmetries of various data sets

Data Set	Signal	Raw Asym.	Acc. Corr. Asym.
Winter/West	348	0.172 ± 0.053	0.069 ± 0.053
Winter/East	360	0.261 ± 0.051	0.165 ± 0.052
Summer/West	241	0.311 ± 0.061	0.200 ± 0.063
Summer/East	224	0.161 ± 0.066	0.062 ± 0.067
West	589	0.227 ± 0.040	0.123 ± 0.041
East	584	0.223 ± 0.040	0.125 ± 0.041
Winter	708	0.216 ± 0.037	0.117 ± 0.037
Summer	465	0.239 ± 0.045	0.135 ± 0.046
Total	1173	0.237 ± 0.029	0.127 ± 0.029

7.3 Systematic Uncertainty

Generally, the source of the systematic uncertainty in the asymmetry measurement is common to the form factor measurement. We will follow the evaluation of systematic uncertainty in the form factor measurement here. As we saw in Section 6.4, the acceptance correction could be affected from the imperfectness of the Monte Carlo simulation. Therefore, we will discuss the evaluation of the uncertainty for both *raw* and *acceptance corrected asymmetry* here.

7.3.1 Smearing by Detector Resolution

The smearing by the detector resolution was critical for the asymmetry measurement. The asymmetry can be diluted by the following mechanisms.

The first mechanism is a resolution effect at the $\sin\phi\cos\phi \sim 0$. Around such a critical region, the ambiguity from a finite detector resolution easily gives the event transition from the positive to negative $\sin\phi\cos\phi$, or vice versa. This kind of event swap possibly dilutes the *raw asymmetry*. This situation is shown in Figure 7.9. The plot shows the $\sin\phi\cos\phi$ distribution from the Monte Carlo simulation of $K_L \rightarrow \pi^+\pi^-\pi^+e^-$. The hatched region around the origin shows the wrong sign events; the reconstructed $\sin\phi\cos\phi$ had a different sign of real $\sin\phi\cos\phi$. Figure 7.10 shows the distribution of $\Delta\phi$ between real ϕ and reconstructed ϕ for wrong sign events. The $\Delta\phi$ plot shows a sharp peak at origin and suggests that the dilution is caused by the resolution effect.

Second mechanism is X track swapping at the track reconstruction. As shown in Figure 7.11, two close X tracks can be swapped when connecting upstream and downstream tracks at the analysis magnet. This track swapping kept the momenta and flight directions of the charged particles in the X view, while the reconstructed charges were exchanged. This also causes wrong sign events. This wrong reconstruction gives a striking effect for events with a close electron-positron pair of $M_{ee} < 2\text{MeV}/c^2$, as shown in Figure 7.12. The hatched histogram in Figure 7.12 shows the distribution of wrong sign events in the $K_L \rightarrow \pi^+\pi^-\pi^+e^-$ Monte Carlo events with $M_{ee} < 2\text{MeV}/c^2$. Since the wrong sign events are caused by the X track swapping, the wrong sign events distributed uniformly. We also plot the $\Delta\phi$ between the real and reconstructed ϕ , in Figure 7.13. The wide distribution, in good contrast to the distribution in Figure 7.10, suggests a poor event reconstruction accuracy for events with $M_{ee} < 2\text{MeV}/c^2$. The X track swapping also appeared as a small uniform distribution of wrong sign events in the dataset with nominal cuts of $M_{ee} > 2\text{MeV}/c^2$, as shown in Figure 7.9.

These effects described above are mostly taken care of by using the detector simulation with a proper resolution effect in the acceptance correction. The only issue about the smearing is if the drift chamber resolution was well-understood or not. We used two configurations of the Monte Carlo simulation for the acceptance correction to evaluate these uncertainties: the Monte Carlo events were generated with the perfect resolution and 1.5 times worse resolutions for the drift chambers. The acceptance correction with the perfect chamber resolution gave a relative difference of 8.5% to the *acceptance corrected asymmetry*, and a difference of 2.3% for the worse case. Therefore, we included 8.7% for the systematic uncertainty to be conservative.

7.3.2 $gM1$ Form Factor

The uncertainty from the form factor of M1 direct emission was also considered. The ambiguity from this source could affect the acceptance correction by changing the distributions of kinematic variables.

This form factor has been measured in Chapter 6 to be $a_1/a_2 = -0.684_{-0.043}^{+0.031}(\text{stat.}) \pm 0.053(\text{syst.})$, and $a_1 = 1.05 \pm 0.14(\text{stat.}) \pm 0.18(\text{syst.})$. Recently, the measurement of this form factor has been improved by $K \rightarrow \pi^+\pi^-\gamma$ analysis at KTeV, which obtained $a_1/a_2 = -0.729 \pm 0.026(\text{stat.}) \pm 0.015(\text{syst.})$ (preliminary) [50]. Although the obtained values from both $K \rightarrow \pi^+\pi^-\gamma$ and $K \rightarrow \pi^+\pi^-\pi^+e^-$ analyses are consistent, we took the difference between those center values as the

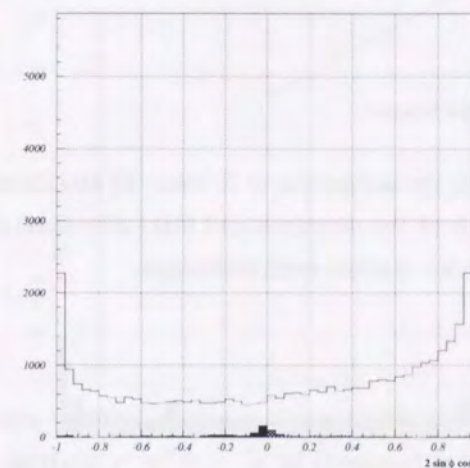


Figure 7.9: The resolution effect causing wrong sign events. The plot shows the $\sin\phi\cos\phi$ distribution from the Monte Carlo simulation of $K_L \rightarrow \pi^+\pi^-\pi^+e^-$. The hatched and solid region around origin shows the wrong sign events; the reconstructed $\sin\phi\cos\phi$ had a different sign from the real $\sin\phi\cos\phi$.

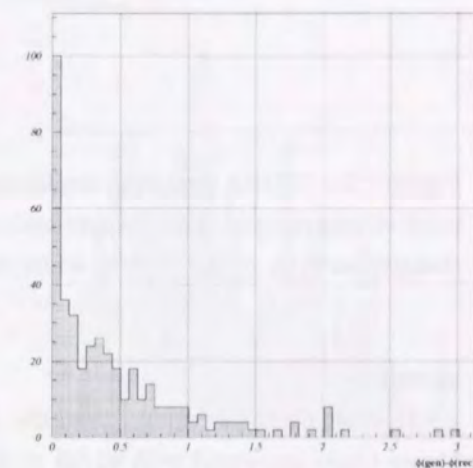


Figure 7.10: The $\Delta\phi$ (difference between real ϕ and reconstructed ϕ) distribution. The $\Delta\phi$ distribution shows a sharp peak at origin and suggests that the dilution is caused by the resolution effect.

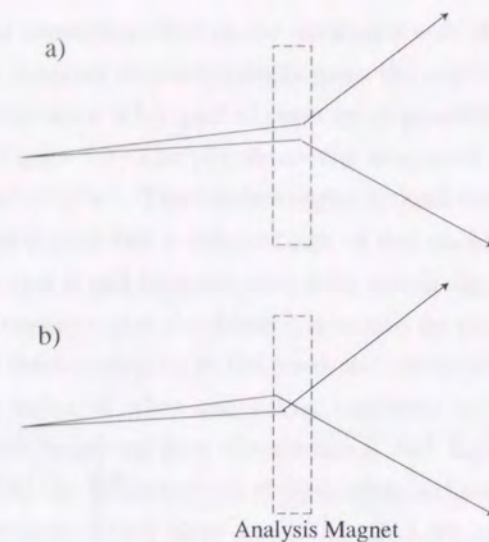


Figure 7.11: X track swapping mechanism. a) a track reconstruction in X view. b) an alternative track reconstruction. The reconstructions a) and b) kept the momenta and flight directions of the charged particles in the X view, while the reconstructed charges were exchanged.

uncertainty.

To evaluate the deviation from the uncertainty, the acceptance correction was done with the Monte Carlo generated with $a_1/a_2 = -0.73$, which was measured by $K \rightarrow \pi^+\pi^-\gamma$ analysis. The asymmetry was changed from 0.127 to 0.124, so the relative difference of 2.4%, was included as the systematic uncertainty.

7.3.3 Vertexing Quality

The understanding of vertexing quality can be important for the asymmetry measurement, since the acceptance of a certain decay topology might be changed by the vertexing.

In order to evaluate the uncertainty, we also used the event weighting method with $K_L \rightarrow \pi^+\pi^-\pi_D^0$ events, introduced at Section 6.4.3. This changed the reconstructed asymmetry of the 25000 signal Monte Carlo by 0.8 %. Therefore, we assigned 0.8% as the systematic uncertainty from this source.

7.3.4 Drift Chamber Inefficiency

As mentioned in Section 6.4.4, there was an inefficiency in the drift chambers around the neutral beam region. This partly changed the acceptance of detector-dependent event topology. We added an artificial inefficiency for DC1 and DC2 to be 5% total and obtained 25000 Monte Carlo signal events. The impact on the reconstructed asymmetry was less than 0.1%, so we concluded that the chamber inefficiency did not affect the asymmetry.



Figure 7.12: The resolution effect causing wrong sign events with $M_{ee} < 2 \text{ MeV}/c^2$. The open histogram shows the $\sin \phi \cos \phi$ distribution from the signal Monte Carlo. The hatched and solid histogram indicates the distribution of wrong sign events. The wrong sign events distribute uniformly and it was caused by the X track swapping.

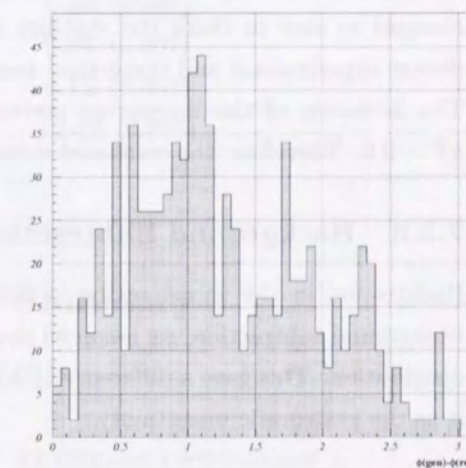


Figure 7.13: The difference between real ϕ and reconstructed ϕ for events with $M_{ee} < 2 \text{ MeV}/c^2$. The wide distribution suggests that it was not caused by the simple detector smearing but the track swapping effect.

7.3.5 Other Physics Parameters

Table 7.4: Experimental Input Parameter.

Parameter	Experimental Input	Description
$gE1$	0.038	E1 Coupling constant
gP	0.15	Charge Radius effect

Experimental input parameters other than the $gM1$ form factor are listed in Table 7.4. In the generation of the Monte Carlo events for the acceptance correction, these parameters were changed to zero to check the stability of reconstructed asymmetry. This is because there is no decent experimental and theoretical measurements of gP and $gE1$, as described in Section 6.4.6. The deviation of the *acceptance corrected asymmetry* was 6.1% for $gE1 = 0.0$ and 3.2 % for $gP = 0.0$. Therefore, the combined error of 6.9% was included in the systematic uncertainty.

7.3.6 Background Subtraction

Background in the signal region is estimated to be 11.3 ± 3.5 events. Instead of considering background subtraction, we assumed that all 11 events were in the positive region of the $\sin \phi \cos \phi$ distribution. This gave a difference of 0.9 % of the *acceptance corrected asymmetry*. We considered it as the systematic uncertainty.

7.3.7 Analysis Dependency

We examined cut dependencies of the asymmetry just as in the form factor measurement. The reconstructed asymmetry was very stable against the cut position so that the deviations was relatively small compared with the statistical uncertainty. We included the deviation of 4.7% as the systematic uncertainty.

Table 7.5: Deviations of analysis cut dependencies in the *acceptance corrected asymmetry*.

Cut	Variation	Description
Z vertex	1.6%	$110m < Z < 154m$
Cluster Threshold	0.8%	Shift HCC threshold by 5 - 10%
M_{ee} cut	0.8%	$M_{ee} > 2.0 - 4.0 \text{ MeV}/c^2$
$M_{\pi\pi ee}$ cut	0.8%	$\pm 6.0 - \pm 14.0 \text{ MeV}/c^2$
Pp0kine cut	1.6%	$-0.0025 - -0.075 \text{ MeV}^2/c^2$
E/p cut	2.3%	$\pm 0.06 - \pm 0.10$
p_t^2 cut	3.1%	$p_t^2 < 30 - 60 \text{ MeV}^2/c^2$
Total	4.7%	

7.3.8 Systematic Uncertainty: Summary

The systematic uncertainties in the asymmetry measurement is summarized in Table 7.6.

Table 7.6: Summary of systematic uncertainties.

Source	Uncertainty(Absolute uncertainty)
Detector resolution	8.7%(0.011)
M1 form factor	2.4%(0.003)
Vertex quality	0.8% (0.001)
DC ineff.	<0.1%(0.000)
Input parameter	6.9% (0.007)
Background subtraction	0.9% (0.001)
Analysis dependency	4.7% (0.005)
Total	12.4% (0.016)

7.4 Asymmetry Measurement: Summary

The angular asymmetry measured in $K_L \rightarrow \pi^+ \pi^- e^+ e^-$ is

$$Asym. = \frac{\int_0^{\pi/2} \frac{d\Gamma}{d\phi} d\phi - \int_{\pi/2}^{\pi} \frac{d\Gamma}{d\phi} d\phi}{\int_0^{\pi/2} \frac{d\Gamma}{d\phi} d\phi + \int_{\pi/2}^{\pi} \frac{d\Gamma}{d\phi} d\phi} = 0.127 \pm 0.029(stat.) \pm 0.016(syst.), \quad (7.5)$$

good agreement with the theoretical prediction

$$Asym. \approx 0.14 \quad (7.6)$$

in Ref. [22, 23]. An alternative way to calculate the reconstructed asymmetry which utilizes the linearity between *raw asymmetry* and *input asymmetry* gave $0.135 \pm 0.029(stat.)$. This is also consistent with the experimental result and the theoretical prediction.

Chapter 8

Branching Ratio Measurement

In this chapter, we describe how we measured the branching ratio of $K_L \rightarrow \pi^+\pi^-e^+e^-$. Unlike the form factor and asymmetry measurements, background contribution to the branching ratio can be easily understood since we only have to know the number of background events in the signal region. Therefore, we here try to relax cuts and enhance the number of signal events in order to make the statistical error lower, although it will increase the number of background events.

First, we briefly describe the event selection along with above strategy and background estimation. Next, studies of systematic uncertainty will be explained. Finally, we summarize this branching ratio measurement.

8.1 Event Selection and Background Estimation

In order to increase the number of signal events, we chose a set of constraints of $p_t^2 < 0.0001 \text{ GeV}^2/c^2$ and no pp0kine cut, from the signal to background ratio matrix table (Table 5.1). The other constraints, such as M_{ee} cut, were kept the same as the asymmetry study. This was actually looser than the original cuts used in the form factor and asymmetry measurements which were $p_t^2 < 0.00004 \text{ GeV}^2/c^2$ and pp0kine $< -0.0025 \text{ GeV}^2/c^2$. With this configuration, we obtained 1731 ± 41.6 events in the signal region of $0.493 < M_{\pi\pi ee} < 0.503 \text{ GeV}/c^2$, including about 170 background events expected from $K_L \rightarrow \pi^+\pi^-\pi_D^0$.

Figure 8.1 shows the invariant mass distribution of the data and expected background with the Monte Carlo simulations in the vicinity of the signal region. The background Monte Carlo simulations were normalized by the K_L flux calculated in the Section 5.6 and generated three times more statistics than the K_L flux. We can see that the background is well-understood in both lower and higher mass regions of the distribution. Dominant background was from the decay $K_L \rightarrow \pi^+\pi^-\pi_D^0$, and there was some contamination from other sources. Number of expected background event is 255.4 ± 13.7 , as shown in Table 8.1. As a consistency check, we looked at the p_t^2 sideband, $0.0001 < p_t^2 < 0.0002 \text{ GeV}^2/c^2$, instead of applying the nominal cut, $p_t^2 < 0.0001 \text{ GeV}^2/c^2$,

as shown in Figure 8.2. The Monte Carlo expectation also agrees well with data.

Thus, the number of signal events above background was $1475.6 \pm 46.1 (\text{stat.})$, where the statistical errors were summed quadratically. We show the data plot after the background subtraction in Figure 8.3. A clear peak indicates the signal. The Monte Carlo simulation agrees well with data in the whole region.

The signal acceptance was also calculated with the Monte Carlo simulation, as shown in Table 8.2. The acceptance increased from 1.392% (Table 5.2) to 1.775 % by relaxing the p_t^2 and Pp0kine cuts.

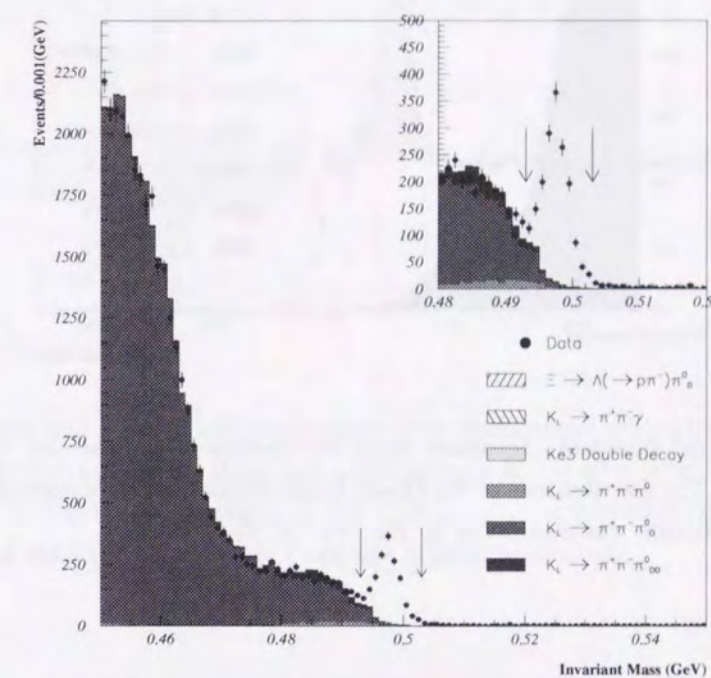


Figure 8.1: Invariant mass distribution after final cuts. The upper-right plot is an enlargement of the signal region. The backgrounds estimated with the Monte Carlo simulations were normalized to the K_L flux. The residual background in the signal region was mostly from $K_L \rightarrow \pi^+\pi^-\pi_D^0$. In this plot, number of events in the signal region was 1731, while the number of estimated background events were approximately 255. Thus, the number of expected signal events after background subtraction was 1475.6.

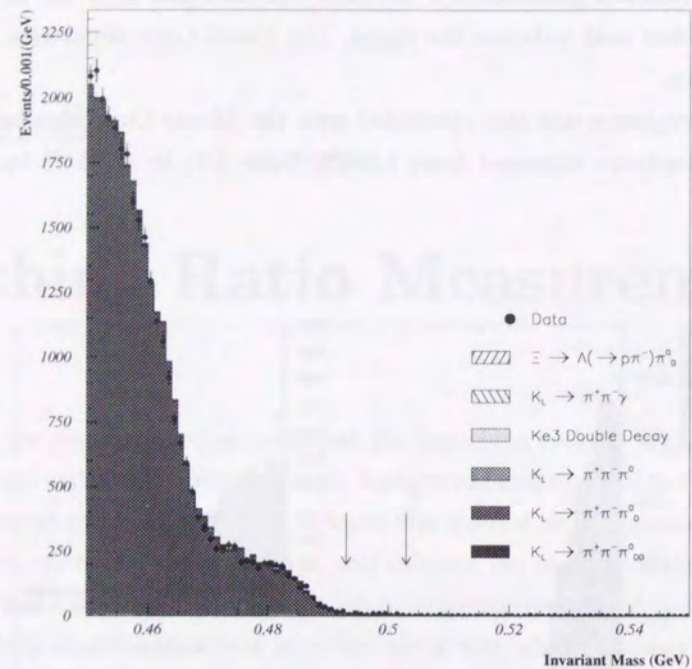


Figure 8.2: The p_t^2 sideband. Invariant mass distribution after final cuts with $0.0001 < p_t < 0.0002 \text{ GeV}^2/c^2$. The distributions of the Monte Carlo simulations were normalized to the K_L flux. The whole distribution was dominated by $K_L \rightarrow \pi^+ \pi^- \pi_D^0$.

Table 8.1: The number of background events from each background source, estimated with the Monte Carlo after final cut. The number of estimated background events were normalized to the K_L flux, so the sum of them gives the number of final background events in the signal region.

Background source	# Background events
$K_L \rightarrow \pi^+ \pi^- \pi_D^0$	169.2 ± 13.0 events
$K_L \rightarrow \pi^+ \pi^- \pi^0$	46.7 ± 2.0
$K_L \rightarrow \pi^+ \pi^- \pi_{DD}^0$	32.2 ± 3.2
$K_L \rightarrow \pi^+ \pi^- \gamma$	3.3 ± 0.6
K_{e3} double decay	3.0 ± 1.7
$\Xi \rightarrow \Lambda \pi_D^0$	0.99 ± 0.14
Total	255.4 ± 13.7

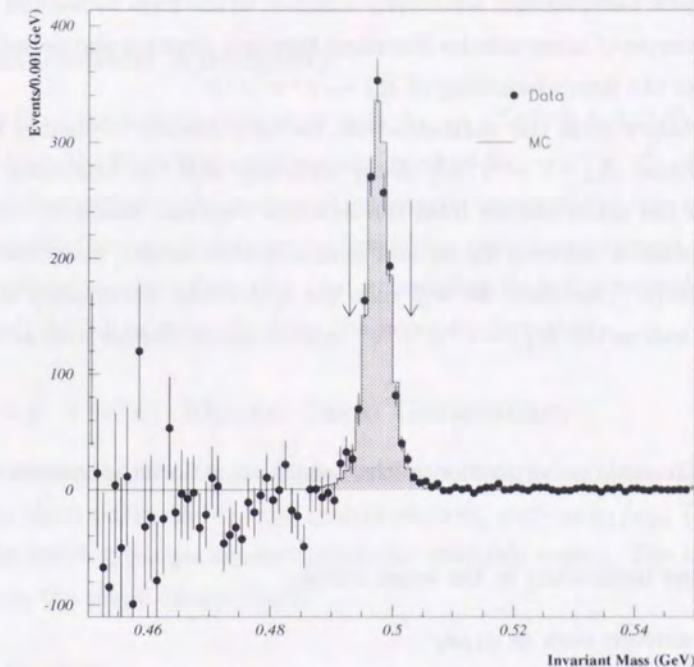


Figure 8.3: Data and Monte Carlo comparison after background subtraction, estimated with Table 8.1 and Figure 8.1. Dots are data, and a histogram is $K_L \rightarrow \pi^+ \pi^- e^+ e^-$ Monte Carlo with area normalization within the signal region, $0.493 < M_{\pi^+ \pi^- e^+ e^-} < 0.503 \text{ GeV}/c^2$. In the whole region, distributions of both data and Monte Carlo are in good agreement.

Table 8.2: The estimated signal acceptance at each analysis phase. The estimation was done by $K_L \rightarrow \pi^+ \pi^- e^+ e^-$ Monte Carlo.

Analysis phase	Efficiency
Level 1 trigger	12.8%
Level 2 trigger	9.08%
Level 3 trigger	8.40%
Basic Cuts	2.18%
$0.493 < M_K < 0.503 \text{ GeV}/c^2$	2.07%
$P_{\pi\pi ee} < 200 \text{ GeV}/c$	2.06%
Vertex $\chi^2 < 50$	2.05%
$M_{ee} > 0.002 \text{ GeV}/c^2$	1.78%
$p_t^2 < 0.00010 \text{ (GeV}^2/c^2)$	1.775%

8.2 Systematic Uncertainty

Sources of systematic uncertainties are mostly common to the form factor and asymmetry measurements. Possible sources of uncertainties described here are, detector simulation, analysis constraint, normalization, and the decay modeling of $K_L \rightarrow \pi^+\pi^-\pi^0$.

For the uncertainty from the normalization, we have already estimated it from the source of the detector response, $K_L \rightarrow \pi^+\pi^-\pi^0$ decay modeling and the branching ratio in Section 5.6. However, most of the uncertainties from the detector response would be canceled out by taking the ratio of acceptances between signal and normalization modes, since the uncertainty affected both modes similarly. Therefore, we will redo the systematic uncertainty study for the detector response here, as well as the $K_L \rightarrow \pi^+\pi^-\pi^0$ specific uncertainties such as the a_1/a_2 form factor uncertainty.

The major systematic uncertainties on the branching ratio measurement discussed here are as follows.

- Drift chamber inefficiency in the beam region.
- Physics parameters such as a_1/a_2 .
- Normalization ambiguity.
- Monte Carlo statistics.
- Background subtraction.

After the explanation of each issue, we will summarize the uncertainty study.

8.2.1 Drift Chamber Inefficiency

The drift chamber inefficiency in the beam region was a major systematic uncertainty in the normalization. However, since the inefficiency was also applied on the signal mode in the branching ratio measurement, this effect almost canceled out. In fact, although adding the inefficiency of 5 % in the beam region in DC1 and DC2 changed the K_L flux measured with $K_L \rightarrow \pi^+\pi^-\pi^0$ by 1.9%, it changed the branching ratio of $K_L \rightarrow \pi^+\pi^-\pi^0$ only by 0.17%. Therefore, we determined the uncertainty from drift chamber inefficiency to be 0.17%.

8.2.2 Vertexing Quality

As shown in Figure 6.10, the understanding of vertex χ^2 distribution might affect the branching ratio measurement. However, this effect is also canceled when taking the acceptance ratio of $K_L \rightarrow \pi^+\pi^-\pi^0$ to $K_L \rightarrow \pi^+\pi^-\pi^0$. The uncertainty from this source was extracted with weighting the Monte Carlo events, same as the other measurements. The modified Monte Carlo gave the

difference of 0.87% on the branching ratio. Therefore, we assigned 0.87 % as the uncertainty from the understanding of vertex quality.

8.2.3 Normalization Ambiguity

The uncertainty from the flux normalization with $K_L \rightarrow \pi^+\pi^-\pi^0$ is 3.15 %, which is dominated by the uncertainty from the branching ratio measurement of $K_L \rightarrow \pi^+\pi^-\pi^0$ of 3.14 %, as explained in Section 5.6. In order to classify the sources of systematic uncertainties into inside and outside of the analysis, we separate the uncertainty in the branching ratio measurement of $K_L \rightarrow \pi^+\pi^-\pi^0$ and other small contributions. therefore, the total uncertainty from the normalization was determined as $[3.14(\text{external}) \oplus 0.33(\text{internal})]\%$ from the normalization study.

8.2.4 $K_L \rightarrow \pi^+\pi^-\pi^0$ Monte Carlo Generation

The uncertainties related to the Monte Carlo simulation is explained here. One possible uncertainty source is physics input parameters in the matrix element, such as a_1/a_2 . This kind of uncertainty was evaluated by varying the parameter within the probable region. The other uncertainty is the statistical error in the signal Monte Carlo.

Monte Carlo Statistics

In order to evaluate the acceptance, we generated 9.0 millions $K_L \rightarrow \pi^+\pi^-\pi^0$ Monte Carlo events and we accepted 0.16 million events after all detector simulation and the analysis cuts. This caused the systematic uncertainty of 0.25%.

Parameters in the Matrix Element

We also introduced the form factor for the acceptance calculation. Since fitted form factors a_1/a_2 and a_1 show a strong correlation between them, as shown in Figure 6.4, we checked variations of the signal acceptance along the one standard deviation contour of these values. The largest difference was 1.06%, so we included it as the uncertainty due to a_1/a_2 and a_1 .

Since the other physical input parameters in the matrix element are also defined with some uncertainties, we have to take these uncertainties into account. The variations of physics parameters and the uncertainties are shown in Table 8.3. We quadratically summed these errors and obtained an error of 2.60%. Therefore, we assigned 2.6% as a systematic uncertainty due to the physics parameters.

8.2.5 Background Subtraction

Here, we examine the background-related uncertainties.

Table 8.3: Stability to parameter fluctuations. Expected error from the Monte Carlo statistics was 0.28%.

Parameter variation	Acceptance Uncertainty
$a_1/a_2, a_1$ 1 σ contour	1.06%
$\eta_{+-} + 1\sigma$	-0.29%
$\eta_{+-} - 1\sigma$	+0.63%
$\Phi_{+-} + 1\sigma$	-0.24%
$\Phi_{+-} - 1\sigma$	-0.79%
$gE1 = 0.0$	-0.39%
$gP = 0.0$	-2.11%
Total	2.60%

Statistical error

Major background sources and expected contaminations are listed in Table 8.1. The background was mostly from $K_L \rightarrow \pi^+\pi^-\pi_D^0$, and there was a small contribution of conversion backgrounds from $K_L \rightarrow \pi^+\pi^-\pi^0$. The uncertainty from statistic fluctuation of the background is estimated as 13.7 events, corresponding to 0.93% of uncertainty in the signal.

Sideband comparison

In order to confirm the expected number of background events, we compared the Monte Carlo expectations with the data in the sideband of the signal. As shown in Figure 8.4, the estimated background level agreed with the data. The uncertainty was taken from the largest discrepancy, 7.37%, between data and the Monte Carlo estimation.

We determined that the uncertainty in the number of background events was 18.8, which is 7.37% of 255.4 background events. This corresponds to 1.27 % of uncertainty in the branching ratio measurement. Thus, we included 1.27 % as the systematic uncertainty.

Miscellaneous Sources

The branching ratio measurements in other background events are also related to the uncertainty. The errors were taken from PDG [9]. This gives total 0.43% of the uncertainty in the branching ratio measurement.

Summary

The uncertainty from the background estimation is, thus, 1.6 % in the branching ratio measurement.

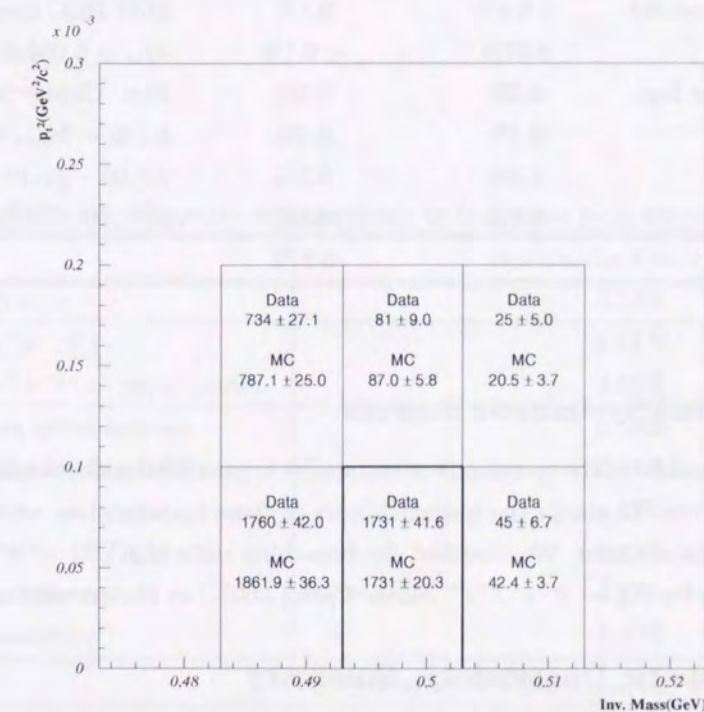


Figure 8.4: Comparison between data and the Monte Carlo estimation in the sideband. The Monte Carlo was normalized to the K_L flux and included the signal Monte Carlo. The largest discrepancy was 7.37% in this plot.

8.2.6 Analysis Dependency

As in the form factor and asymmetry analysis, consistency check in the analysis dependency with various cuts was examined here. The results are shown in Table 8.4. The total uncertainty, 0.7% was assigned to the systematic uncertainty.

Table 8.4: Summary of analysis dependency.

Cut	Normalization	BR measurement	Estimation Method
Z vertex	0.09%	0.2%	$110m < Z < 154m$
Cluster Threshold	< 0.1%	0.1%	Shift HCC threshold
M_{ee} cut	0.07%	< 0.1%	$M_{ee} > 0.004, 0.008\text{GeV}/c^2$
Min. Cluster Sep.	0.3%	0.3%	Min. Cluster Sep. > 20 cm
$M_{ee\gamma}$ cut	0.4%	0.4%	$0.130 < M_{ee\gamma} < 0.136\text{GeV}/c^2$
E/p cut	1.8%	0.3%	$\pm 0.06 - \pm 0.10$
p_t^2 cut	0.6%	0.4%	$p_t^2 < 60 - 100\text{MeV}^2/c^2$
Total		0.7 %	

8.2.7 External Systematic Sources

So far, we have considered the systematic uncertainties originated from both analysis-induced(internal) and external sources. To clarify the responsibilities of those uncertainties, we split off the external systematic uncertainty here. We classified the branching ratio of $K_L \rightarrow \pi^+\pi^-\pi_D^0$ (3.14%) and the input parameters for $K_L \rightarrow \pi^+\pi^-e^+e^-$ Monte Carlo(2.60%) as the external uncertainties.

8.2.8 Systematic Uncertainty: Summary

We summarize the systematic uncertainty in the branching ratio calculation in Table 8.5. The largest uncertainty was the error in the branching ratio of $K_L \rightarrow \pi^+\pi^-\pi_D^0$. The external systematic uncertainty is split off here.

8.3 Branching Ratio Measurement: Summary

We determined the branching ratio for the decay $K_L \rightarrow \pi^+\pi^-e^+e^-$, based on 1475.6 signal events as:

$$BR(K_L \rightarrow \pi^+\pi^-e^+e^-) = (3.55 \pm 0.11(stat.) \pm 0.07(syst.internal) \pm 0.14(syst.external)) \times 10^{-7}.$$

The ratio between the signal and the normalization modes, which is not affected by the error on the branching ratio measurement of $K_L \rightarrow \pi^+\pi^-\pi_D^0$, is:

$$\frac{BR(K_L \rightarrow \pi^+\pi^-e^+e^-)}{BR(K_L \rightarrow \pi^+\pi^-\pi_D^0)} = (2.36 \pm 0.07(stat.) \pm 0.05(syst.internal) \pm 0.06(syst.external)) \times 10^{-4}.$$

Table 8.5: Summary of uncertainty in branching ratio measurement.

Source	Acceptance Uncertainty
Statistical error	3.13%
$BR(K_L \rightarrow \pi^+\pi^-\pi_D^0)$	3.14 %
MC $K_L \rightarrow \pi^+\pi^-e^+e^-$ input param.	2.60%
Normalization; other sources	0.33%
Detector(Drift chamber Ineff.)	0.17%
Vertex Quality	0.87%
$K_L \rightarrow \pi^+\pi^-e^+e^-$ MC stat.	0.25%
Background-originated	1.6 %
Analysis dependency	0.7 %
Total	$(3.13(stat.) \oplus 2.00(syst.internal) \oplus 4.08(syst.external))\%$

Chapter 9

Discussion

So far, we derived physics parameters from $K_L \rightarrow \pi^+\pi^-e^+e^-$ data sample. In this chapter, using the results, we discuss the implications of the results.

9.1 Form Factor Measurement

The M1 direct emission(DE) form factor was determined as

$$a_1/a_2 = -0.684_{-0.043}^{+0.031}(\text{stat.}) \pm 0.053(\text{syst.}) \quad (9.1)$$

$$a_1 = 1.05 \pm 0.14(\text{stat.}) \pm 0.18(\text{syst.}). \quad (9.2)$$

This result compares well with a preliminary result of $K_L \rightarrow \pi^+\pi^-\gamma$ performed by the KTeV collaboration [31],

$$a_1/a_2 = -0.729 \pm 0.026(\text{stat.}) \pm 0.015(\text{syst.}). \quad (9.3)$$

From the theoretical point of view, a_1 and a_2 depend on the mixing angle, $\theta_{\eta-\eta'}$, between the SU(3) nonet members η and η' , and the flavor SU(3) breaking parameter, ξ .

Figure 9.1 shows our result and results on a_1/a_2 direct measurements from the KTeV and previous(Fermilab E731)^{*1} experiment in the $K_L \rightarrow \pi^+\pi^-\gamma$ [31, 32]. The direct measurements with $K_L \rightarrow \pi^+\pi^-\gamma$ were made by directly fitting the E_γ spectrum in the center-of-mass frame. We obtained consistent results of $a_1/a_2 \sim -0.7$.

Moreover, the form factor a_1/a_2 can be also extracted from the DE branching ratio measurement through $\theta_{\eta-\eta'}$ determination in the chiral Lagrangian framework by Lin and Valencia [29, 30]. Their model predicts the mixing angle to be $\theta_{\eta-\eta'} = -20^\circ$ from the experimental DE branching ratio, $BR(K_L \rightarrow \pi^+\pi^-\gamma)_{DE} \sim 3 \times 10^{-5}$, and the SU(3) breaking parameter, $\xi = 0.17$, as shown in

^{*1}The E_γ spectrum from E731 data was reanalyzed and directly fitted [32], and the fit result is different from the published result of $a_1/a_2 = -1.8 \pm 0.2$ [37]. This is because the published result assumed the Lin and Valencia model to calculate the form factor with the DE branching ratio.

Figure 9.2 [37, 38]. The form factor can then be evaluated with the obtained mixing angle and the SU(3) breaking parameter from a relation shown in Figure 9.1. This gives the form factor of $a_1/a_2 = -1.8 \pm 0.2$.

The predicted value, $a_1/a_2 = -1.8 \pm 0.2$, does not agree well with the direct measurement results, $a_1/a_2 \sim -0.7$. Conversely, this means that in our configuration of $a_1/a_2 \sim -0.7$, the Lin and Valencia model predicts the DE branching ratio of $BR(K_L \rightarrow \pi^+\pi^-\gamma) < 1.0 \times 10^{-5}$, in contradiction to the recent experimental result, $BR(K_L \rightarrow \pi^+\pi^-\gamma) = (3.19 \pm 0.09) \times 10^{-5}$ [31].

Therefore, our results related to the $\theta_{\eta-\eta'}$ mixing angle and the SU(3) breaking parameter does not support the Lin and Valencia model.

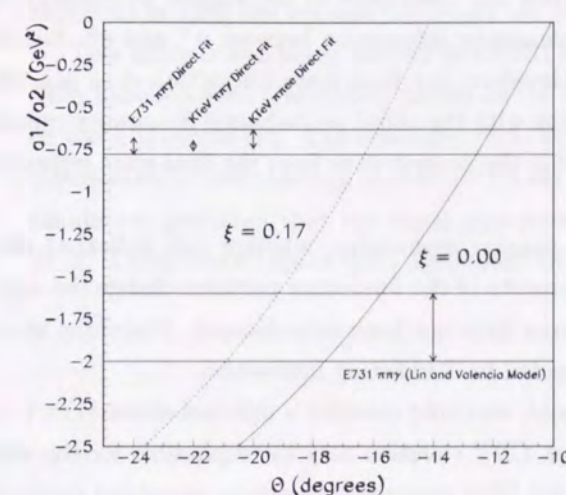


Figure 9.1: Results on the DE form factor, a_1/a_2 . The horizontal axis means $\theta_{\eta-\eta'}$, and the vertical axis means the direct a_1/a_2 measurement results from KTeV [31] and E731 ($a_1/a_2 \sim -0.7$) [32], and the model-dependent result from E731. The model-dependent result ($a_1/a_2 = -1.8 \pm 0.2$) was extracted from the SU(3) breaking parameter, $\xi = 0.17$, and $\theta_{\eta-\eta'} = -20^\circ \pm 1^\circ$, which was calculated with the DE branching ratio (3×10^{-5}) by using the Lin and Valencia model [29] shown in Figure 9.2.

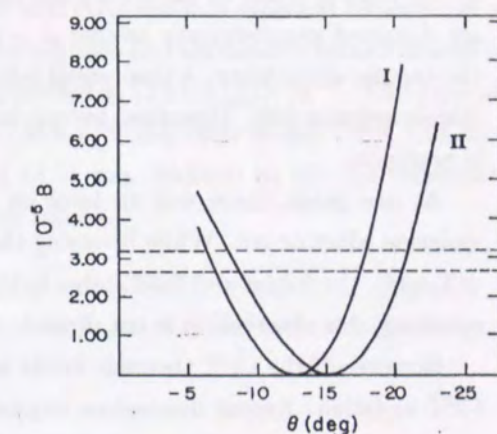


Figure 9.2: Relation between $\theta_{\eta-\eta'}$ and the DE branching ratio. The mixing parameter $\theta_{\eta-\eta'}$ is related to the DE branching ratio in the Lin and Valencia model [29], which predicts $\theta \sim -20^\circ \pm 1^\circ$ from E731 result, $BR(K_L \rightarrow \pi^+\pi^-\gamma)_{DE} = (3.19 \pm 0.16) \times 10^{-5}$ [37]. I is for $\xi = 0.00$ (non-breaking limit), and II is for $\xi = 0.17$, the reasonable value referred in Ref. [30]. In the Lin and Valencia model, the a_1/a_2 was extracted from $\theta \sim -20^\circ \pm 1^\circ$ and $\xi = 0.17$ as compared with Figure 9.1.

9.2 Asymmetry Measurement

We have measured the angular asymmetry in $K_L \rightarrow \pi^+\pi^-e^+e^-$ with a good precision:

$$Asym. = \frac{\int_0^{\pi/2} \frac{d\Gamma}{d\phi} d\phi - \int_{\pi/2}^{\pi} \frac{d\Gamma}{d\phi} d\phi}{\int_0^{\pi/2} \frac{d\Gamma}{d\phi} d\phi + \int_{\pi/2}^{\pi} \frac{d\Gamma}{d\phi} d\phi} = 0.127 \pm 0.029(stat.) \pm 0.016(syst.).$$

We here discuss any possible contributions to the angular asymmetry.

One possible contribution to the angular asymmetry is the final state interaction. However, this contribution cancels within the highest order of the electromagnetic interaction, since a) an interaction between π^+ and π^- (e^+ and e^-) does not contribute to the angular asymmetry, and b) the angle ϕ could be shifted by the electromagnetic interaction between π^+ and e^+ , but they are distorted symmetrically around $\phi = 0$. Therefore, the final state interaction does not affect the angular asymmetry. A theoretical calculation with the chiral perturbation framework supports this description [26]. Therefore, we conclude that the contribution from the final state interaction is negligible.

At one point, there was an issue on the angular asymmetry, whether this indicated the T violation effect or not. While reversing the momenta of the final state particles change the sign of ϕ (T-odd), the initial and final states in the decay have not been interchanged. Therefore, strictly speaking, this observation is not directly connected to T violating interaction.

However, if the CPT theorem would not hold, we could consider a different scenario in T and CPT violation. Recent discussions suggest that CPT violation may be responsible for the whole angular asymmetry in $K_L \rightarrow \pi^+\pi^-e^+e^-$ [41, 42]. This assumption needs an unnatural parameter configuration, but we cannot reject this possibility at this time.

The orthodox interpretation of the asymmetry in $K_L \rightarrow \pi^+\pi^-e^+e^-$ is that CPT invariance holds, but the CP violating effect is responsible for the whole angular asymmetry. In this context, the theoretical prediction agrees well with the experimental result. In addition, the asymmetry is extracted only with natural and well-known CP violating parameters. This is the most preferable interpretation which is consistent with the current knowledge of CP violation.

9.3 Branching Ratio Measurement

The branching ratio measured in this analysis is

$$Br(K_L \rightarrow \pi^+\pi^-e^+e^-) = (3.55 \pm 0.11(stat.) \pm 0.07(syst.\textit{internal}) \pm 0.14(syst.\textit{external})) \times 10^{-7}, (9.4)$$

which agrees with the previous publication [40],

$$Br(K_L \rightarrow \pi^+\pi^-e^+e^-) = (3.2 \pm 0.6(stat.) \pm 0.4(syst.)) \times 10^{-7}. (9.5)$$

In this analysis, we improved the precision of the branching ratio by four times than of the previous measurement. The largest systematic uncertainty in the previous analysis was due to the lack of

knowledge of $gM1$ form factor. In our analysis, we have reduced the uncertainty with a better understanding of the form factor.

9.4 Remarks and Future Prospects

These measurements represent the first step in our understanding of the decay $K_L \rightarrow \pi^+\pi^-e^+e^-$.

The operation of fixed-target experiment E799-II continues for 1999 and we plan to collect two to four times the statistics used in this thesis. In branching ratio measurement using the technique described here, we have already achieved the systematic limit by the uncertainty in the π^0 Dalitz decay branching ratio. The accuracy of the angular asymmetry and the $gM1$ form factor can be improved in 1999 run because our errors are still dominated by statistics.

This mode is also being studied at CERN NA48 and their result is expected to come out soon. They have reported preliminary results on the branching ratio and asymmetry measurements based on 458 ± 22 events [54]. The branching ratio were presented as $(2.9 \pm 0.15) \times 10^{-7}$. The experiment-dependent(i.e., the *raw asymmetry* for NA48) was $(20 \pm 5)\%$ and their Monte Carlo and detector simulation predicted that the *input asymmetry* of 14 % was modified to the *raw asymmetry* of 22 %. Those results are in good agreement with our results.

Chapter 10

Conclusion

We measured the CP violating effect in the decay $K_L \rightarrow \pi^+\pi^-e^+e^-$ with 1162 signal events. The acceptance corrected asymmetry is

$$Asym. = \frac{\int_0^{\pi/2} \frac{d\Gamma}{d\phi} d\phi - \int_{\pi/2}^{\pi} \frac{d\Gamma}{d\phi} d\phi}{\int_0^{\pi/2} \frac{d\Gamma}{d\phi} d\phi + \int_{\pi/2}^{\pi} \frac{d\Gamma}{d\phi} d\phi} = 0.127 \pm 0.029(stat.) \pm 0.016(syst.).$$

This represents a first CP violation appearance in a kinematic parameter and the largest CP violating effect observed in the world, as well as the fourth appearance of the indirect CP violating effect.

The branching ratio of $K_L \rightarrow \pi^+\pi^-e^+e^-$ was also measured with 1475.6 signal events. The result is

$$Br(K_L \rightarrow \pi^+\pi^-e^+e^-) = (3.55 \pm 0.11(stat.) \pm 0.07(syst.internal) \pm 0.14(syst.external)) \times 10^{-7},$$

which agrees with the previous publication,

$$Br(K_L \rightarrow \pi^+\pi^-e^+e^-) = (3.2 \pm 0.6(stat.) \pm 0.4(syst.)) \times 10^{-7}.$$

If we split off the uncertainty from the branching ratio measurement in the $K_L \rightarrow \pi^+\pi^-\pi_D^0$, the ratio of the branching ratios becomes

$$\frac{Br(K_L \rightarrow \pi^+\pi^-e^+e^-)}{Br(K_L \rightarrow \pi^+\pi^-\pi_D^0)} = (2.36 \pm 0.07(stat.) \pm 0.05(syst.internal) \pm 0.06(syst.external)) \times 10^{-4}.$$

The $gM1$ direct emission form factor was determined as

$$\begin{aligned} a_1/a_2 &= -0.684^{+0.031}_{-0.043}(stat.) \pm 0.053(syst.) \\ a_1 &= 1.05 \pm 0.14(stat.) \pm 0.18(syst.). \end{aligned}$$

This result compares well with a preliminary result of $K_L \rightarrow \pi^+\pi^-\gamma$ measured by KTeV collaboration [31],

$$a_1/a_2 = -0.729 \pm 0.026(stat.) \pm 0.015(syst.).$$

Our results on the $gM1$ form factor measurements in $K_L \rightarrow \pi^+\pi^-e^+e^-$ and $K_L \rightarrow \pi^+\pi^-\pi_D^0$, do not support the Lin and Valencia model.

In conclusion, this experiment found the largest indirect CP violation effect in a kinematic variable. This result is consistent with any other related measurement and the theoretical prediction.

Appendix A

Maximum Likelihood Method

This describes how the form factor of $gM1$ direct emission was determined with the maximum likelihood method. This is the explanation to the application for the form factor measurement, and does not intend to show a general formalism of the maximum likelihood method.

A.1 Definition

Let us consider to determine a set of physics parameters a from measurements of a set of certain observables x . Assume that we have a collection of N signal events corresponding to the independent measurement of variable sets x_i , where i runs 1 to N . We wish to obtain the parameter set a of a fitting function $y(x_i) = y(x_i; a)$ from these data. For each event, we convert $y(x_i)$ to a normalized probability density function

$$P_i = P(x_i; a) \quad (\text{A.1})$$

evaluated at the observables x_i . The likelihood function is simply multiplying P_i event by event:

$$\mathcal{L}(a) = \prod_{i=1}^N P_i. \quad (\text{A.2})$$

Equation A.2 shows a probability to realize the sets of observables x_i with a configuration of parameters a . We can consider that these observables would be given with the most possible values of parameters a . Therefore, the maximum-likelihood value of parameters is obtained by maximizing $\mathcal{L}(a)$ with respect to the parameter a . To maximize Equation A.2, we sometimes take a logarithm for both sides of the equation, in order to maximize it easy,

$$\log \mathcal{L}(a) = \sum_{i=1}^N \log P_i. \quad (\text{A.3})$$

In addition, a detection efficiency of the signal is crucial to the solution of the problem. This is both detector- and observables-dependent. The detection efficiency would give a certain weight

to the probability density function P_i . So the probability to observe a single event with a certain observed variables x_i is obtained as

$$P_i = \text{Norm} \cdot A_i \cdot \mathcal{P}(x_i; a) \quad (\text{A.4})$$

where the factor A_i is the detection efficiency and the factor $\mathcal{P}(x_i; a)$ is a probability to decay a particle with the variables $x = x_i$. In our case, $\mathcal{P}(x_i; a)$ corresponds to $K_L \rightarrow \pi^+ \pi^- e^+ e^-$ differential cross section with related to x_i . Norm is the normalization factor calculated later.

For the decay of $K_L \rightarrow \pi^+ \pi^- e^+ e^-$ at the KTeV detector, the probability density function P_i with normalization becomes

$$P_i = \text{Norm} \cdot A_i \cdot \frac{d\Gamma(x_i; a)}{dx} \quad (\text{A.5-a})$$

$$a = (a_1/a_2, a_1, \eta_{+-}, \Phi_{+-}, gP, gE_1) \quad (\text{A.5-b})$$

$$x_i = (\phi_i, M_{\pi\pi i}, M_{ee i}, \cos \theta_{\pi^+ i}, \cos \theta_{e^+ i}) \quad (\text{A.5-c})$$

where $d\Gamma(x_i; a)/dx$ is a differential cross section of $K_L \rightarrow \pi^+ \pi^- e^+ e^-$ with respect to x .

To normalize P_i , we integrate P_i over physically possible value of x .

$$\text{Norm} \cdot \int dx (A(x) \cdot \frac{d\Gamma(x; a)}{dx}) = 1, \quad (\text{A.6})$$

so the normalization factor for P_i is obtained as

$$\text{Norm} = \frac{1}{\int dx (A(x) \cdot \frac{d\Gamma(x; a)}{dx})}. \quad (\text{A.7})$$

Finally, the probability density function P_i , and the likelihood function \mathcal{L} becomes

$$P_i = \frac{A_i \cdot \frac{d\Gamma(x_i; a)}{dx}}{\int dx (A(x) \cdot \frac{d\Gamma(x; a)}{dx})}, \quad (\text{A.8})$$

$$\ln \mathcal{L} = \sum_i \ln P_i = \sum_i \ln \frac{A_i \cdot \frac{d\Gamma(x_i; a)}{dx}}{\int dx (A(x) \cdot \frac{d\Gamma(x; a)}{dx})}. \quad (\text{A.9})$$

In following sections, we can assume that the detection efficiency A_i is independent of parameter a so that A_i can be written as $A_i = A(x_i)$.

A.2 Use of Monte Carlo

Since it is impossible to give an exact analytic form of the detection efficiency and the normalization factor, we here use the Monte Carlo simulation to determine them. In this section, the parameter a is fixed as $a = a_0$, to make the problem easier.

First, we consider the simplest case, the detection efficiency is unity over any x , i.e. $A(x) = 1$. When the Monte Carlo simulation is performed according to the differential cross section $d\Gamma(x; a_0)/dx$, a relation to a variable $n(x; a_0)$, which is the number of events in an infinitesimal phase space dx , becomes

$$\frac{d\Gamma(x; a_0)}{dx} dx \propto \frac{n(x; a_0)}{N} dx \quad (\text{A.10})$$

if the number of generated events, N , goes to infinity.

We have to consider the normalization to derive the equation. Integrating both sides of Equation A.10, we obtain

$$\int dx \frac{d\Gamma(x; a_0)}{dx} = \Gamma(a_0) \quad (\text{A.11})$$

for the left side and

$$\int dx \frac{n(x; a_0)}{N} = 1 \quad (\text{A.12})$$

for the right side. Therefore, Equation A.10 becomes

$$\frac{d\Gamma(x; a_0)}{dx} dx = \frac{n(x; a_0)}{N} \Gamma(a_0) dx \quad (\text{A.13})$$

Next, we take the detection efficiency into account. The detection efficiency in dx is defined by the ratio of the number of survivals through all detector simulation and cut to that of generated events in dx .

$$A(x) \cdot \frac{d\Gamma(x; a_0)}{dx} dx = \frac{n'(x; a_0)}{n(x; a_0)} \frac{n(x; a_0)}{N} \Gamma(a_0) dx \quad (\text{A.14-a})$$

$$= \frac{n'(x; a_0)}{N} \Gamma(a_0) dx \quad (\text{A.14-b})$$

where $n'(x; a_0)$ is the number of events in dx after all cut. After integration, we obtain

$$\int dx A(x) \cdot \frac{d\Gamma(x; a_0)}{dx} = \int dx \frac{n'(x; a_0)}{N} \Gamma(a_0) \quad (\text{A.15-a})$$

$$= (\text{Overall Acceptance})(a_0) \cdot \Gamma(a_0) \quad (\text{A.15-b})$$

$$(\text{Overall Acceptance})(a_0) = \frac{N'(a_0)}{N} \quad (\text{A.15-c})$$

where $N'(a_0)$ is the number of events after all cut.

Finally, we calculate $A(x_i)$ for the numerator. Assuming that the acceptance is constant to the detector resolution,

$$A(x_i) = m'(x_i)/m(x_i) \quad (\text{A.16})$$

where $m(x_i)$ is the total number of events of Monte Carlo generation with x_i and $m'(x_i)$ is surviving events after all the detector simulation and analysis cuts with x_i .

We can write the equation A.9 as

$$\ln \mathcal{L} = \sum_i \ln \frac{m'(x_i)/m(x_i) \cdot \frac{d\Gamma(x_i; a_0)}{dx}}{\frac{N'(a_0)}{N} \cdot \Gamma(a_0)} \quad (\text{A.17})$$

A.3 Reduction of Monte Carlo Generation

We consider here to reduce the Monte Carlo generation against arbitrary a for the economy of time and processing power. We just want a general form of

$$\frac{d\Gamma(x; a)}{dx} dx = \frac{n(x; a)}{N} \Gamma(a) dx. \quad (\text{A.18})$$

First, we can write the left side of above equation with the factor $A(x)$

$$A(x) \frac{d\Gamma(x; a)}{dx} dx = \frac{d\Gamma(x; a)/dx}{d\Gamma(x; a_0)/dx} \cdot A(x) \cdot \frac{d\Gamma(x; a_0)}{dx} dx \quad (\text{A.19})$$

This lead to

$$A(x) \frac{d\Gamma(x; a)}{dx} dx = \frac{d\Gamma(x; a)/dx}{d\Gamma(x; a_0)/dx} \cdot \frac{n'(x; a_0)}{N} \Gamma(a_0) dx \quad (\text{A.20})$$

This means that the number of event from general form is given as a weighted number of events generated with a parameter a_0 and weight $\frac{d\Gamma(x; a)/dx}{d\Gamma(x; a_0)/dx}$.

$$\int dx A(x) \cdot \frac{d\Gamma(x; a)}{dx} = \sum_j \left(\frac{n'(x_j; a_0)}{N} \cdot \frac{d\Gamma(x_j; a)/dx}{d\Gamma(x_j; a_0)/dx} \right) \cdot \Gamma(a_0) \quad (\text{A.21})$$

Finally, we can give the general form of the likelihood function as

$$\ln L(a) = \sum_i \ln \frac{m'(x_i)/m(x_i) \cdot \frac{d\Gamma(x_i; a)}{dx}}{\sum_j \left(\frac{n'(x_j; a_0)}{N} \cdot \frac{d\Gamma(x_j; a_0)/dx}{d\Gamma(x_j; a_0)/dx} \right) \cdot \Gamma(a_0)} \quad (\text{A.22})$$

In our study, we do not have to calculate $m'(x_i)/m(x_i)$ and $\Gamma(a_0)$ since their contributions are only constants. So we maximized this $\ln L(a)$;

$$\ln L(a) = \sum_i \ln \frac{\frac{d\Gamma(x_i; a)}{dx}}{\sum_j \left(\frac{n'(x_j; a_0)}{N} \cdot \frac{d\Gamma(x_j; a_0)/dx}{d\Gamma(x_j; a_0)/dx} \right)} + \text{Const.} \quad (\text{A.23})$$

A.4 Fit Example

In this thesis, we generated 30 million Monte Carlo events of $K_L \rightarrow \pi^+ \pi^- e^+ e^-$ with the parameters of $a_1/a_2 = -0.70$ and $a_1 = 1.0$ for the acceptance calculation in the denominator of Equation A.23. After all cut, we obtained about 0.5 million events of the signal and utilized in the study. The maximization was done with MIGRAD and MINOS in MINUIT since we obtained analytic form of the likelihood function. Figure 6.4 shows a result of maximum likelihood fit. The fit results based on 1173 events of the signal are

$$a_1/a_2 = -0.684^{+0.031}_{-0.043} \quad (\text{A.24})$$

$$a_1 = 1.05 \pm 0.14 \quad (\text{A.25})$$

Appendix B

Pp0kine: Kinematics with a Missing Particle

Sometimes one particle in the final state of a decay was either missing or ignored in this experiment. In $K_L \rightarrow \pi^+\pi^-\pi^0$ analysis, the $K_L \rightarrow \pi^+\pi^-\pi^0$ with the γ missing is the largest background. Here, we extract the useful kinematical relation to handle the event with a missing or ignored particle [51, 52, 53].

In general, assuming that a particle of mass M and four momentum $\mathcal{P} = (E, \vec{P})$ will decay into a set of particles which can be observed and reconstructed and one particle which cannot. For a missing particle, we define the mass and momentum as m_{mis} and $p_{mis} = (E_{mis}, \vec{p}_{mis})$. For reconstructed particles, we treat them as a single system with a mass m_{obs} and a momentum $p_{obs} = (E_{obs}, \vec{p}_{obs})$. In this chapter, all of the quantities with an asterisk(*) refers to quantities in the center-of mass-system of the decay particle.

From the invariant mass squared

$$\mathcal{P} \cdot \mathcal{P} = M^2 = m_{obs}^2 + m_{mis}^2 + 2(E_{obs}E_{mis} - \vec{p}_{obs} \cdot \vec{p}_{mis}) \quad (\text{B.1})$$

and

$$\mathcal{P} \cdot p_{mis} = ME_{mis}^* = m_{mis}^2 + E_{obs}E_{mis} - \vec{p}_{obs} \cdot \vec{p}_{mis}, \quad (\text{B.2})$$

we obtain

$$\begin{aligned} E_{mis}^* &= \frac{M^2 - m_{obs}^2 + m_{mis}^2}{2M} \\ p_{mis}^{*2} &= \frac{(M^2 - m_{obs}^2 + m_{mis}^2)^2 - 4m_{obs}^2 m_{mis}^2}{4M^2}. \end{aligned} \quad (\text{B.3})$$

In a fixed target experiment, the decay particles are boosted along the line spanned between the target and decay vertex point. In this context, the transverse momentum p_t of the observed particle(s) can determine the magnitude of longitudinal momentum of the observed particle system.

This, thus, is equivalent to measure the longitudinal momentum of the unobserved particle in the decay rest frame.

$$\begin{aligned} p_{obs\parallel}^{*2} = p_{mis\parallel}^{*2} &= p_{obs}^{*2} - p_t^2 \\ &= \frac{(M^2 - m_{obs}^2 + m_{mis}^2)^2 - 4m_{obs}^2 m_{mis}^2}{4M^2} - p_t^2 \\ &= \frac{(M^2 - m_{obs}^2 + m_{mis}^2)^2 - 4m_{obs}^2 m_{mis}^2 - 4M^2 p_t^2}{4M^2}. \end{aligned} \quad (\text{B.4})$$

We have obtained the magnitude of the longitudinal component of the momentum in the decay's center-of-mass frame.

Historically, a quantity "Pp0kine" has been often used for the analyses with a missing particle instead of $p_{obs\parallel}^{*2}$. To examine this, consider the product $\mathcal{P}p_{obs}$

$$\begin{aligned} \mathcal{P}p_{obs} = ME_{obs}^* &= EE_{obs} - \vec{P} \cdot \vec{p}_{obs} \\ &= EE_{obs} - \vec{P} \cdot \vec{p}_{obs\parallel}. \end{aligned} \quad (\text{B.5})$$

Regrouping and squaring, we have

$$(E_{obs}^2 - |\vec{p}_{obs\parallel}|^2)|\vec{P}|^2 - 2ME_{obs}^*(\vec{p}_{obs\parallel} \cdot \vec{P}) + M^2(E_{obs}^2 - E_{obs}^{*2}) = 0. \quad (\text{B.6})$$

Solving for P , and substituting $m_{obs}^2 + p_t^2$ for $E_{obs}^2 - |\vec{p}_{obs\parallel}|^2$, we obtain

$$\begin{aligned} |\vec{P}| &= \gamma\beta M \\ &= \frac{(E_{obs}^*|\vec{p}_{obs\parallel}| \pm E_{obs}|\vec{p}_{obs\parallel}^*|)M}{m_{obs}^2 + p_t^2} \\ &= \frac{|\vec{p}_{obs\parallel}|(M^2 - m_{obs}^2 + m_{mis}^2) \pm (|\vec{p}_{obs\parallel}|^2 + m_{obs}^2)^{1/2}[(M^2 - m_{obs}^2 + m_{mis}^2)^2 - 4m_{obs}^2 m_{mis}^2 - 4M^2 p_t^2]^{1/2}}{2(m_{obs}^2 + p_t^2)} \end{aligned} \quad (\text{B.7})$$

When we assume $|\vec{p}_{obs\parallel}| = 0$ in Equation B.7, we obtain a variable called "Pp0kine":

$$\text{Pp0kine} = \frac{(M^2 - m_{obs}^2 + m_{mis}^2)^2 - 4m_{obs}^2 m_{mis}^2 - 4M^2 p_t^2}{4(m_{obs}^2 + p_t^2)}. \quad (\text{B.8})$$

The quantity "Pp0kine" is connected with a square of a longitudinal momentum shown in Equation B.4 as follows:

$$\text{Pp0kine} = p_{obs\parallel}^{*2} \cdot \frac{M^2}{m_{obs}^2 + p_t^2}. \quad (\text{B.9})$$

Pp0kine is equivalent to $p_{obs\parallel}^{*2}$ with a rescaling factor, $M^2/(m_{obs}^2 + p_t^2)$, which boosts to the frame of $|\vec{p}_{obs\parallel}| = 0$. This is invariant in the sense that the distribution in Pp0kine is independent of the decay particle's momentum.

In this thesis, we refer Pp0kine as the relation in $K_L \rightarrow \pi^+\pi^-\pi^0$ and a missing particle assigned to the π^0 .

Bibliography

- [1] G. Lüders, Kong. Dansk Vid. Selskab, Mat. Fys. Medd. **28**, 5(1954); Ann. Phys. **2**, 1(1957).
- [2] W. Pauli, Nuovo. Cimento **6**, 204(1957).
- [3] T.D. Lee and C.N. Yang, Phys. Rev. **104**, 254(1956).
- [4] C.S. Wu *et al.*, Phys. Rev. **105**, 1413(1957).
- [5] J.H. Christenson, J.W. Cronin, V.L. Fitch, and R. Turlay, Phys. Rev. Lett.**13**, 138(1964).
- [6] E.P. Wigner and V.F. Weisskopf, Z Phys. **64**(1930);**65** 18 (1930);
- [7] A. Malensek, FNAL Preprint **FN-341** and **FN-341a**(errata)(1981).
- [8] K. Arisaka *et al.*, KTeV Design Report, **FN-580**(1992).
- [9] Particle Data Group, The European Physical Journal **3** (1998).
- [10] A. Angelopoulos *et al.*, Phys. Lett. **B444**, 38(1998); Phys. Lett. **B444**, 43(1998).
- [11] J. Bijnens, G. Ecker and J. Gasser, in The DAΦNE Physics Handbook(1992).
- [12] J. Adams *et al.*, Phys. Rev. Lett. **80**, 4123(1998).
- [13] E. D. Zimmerman, Nucl. Inst. Meth. **A426**, 229(1999).
- [14] P. Shanahan, Proceedings of ICHEP, Frascati, Italy(1996).
- [15] R. Kessler, "KTeV Trigger Control Logic", KTeV Internal Note 361(1996).
- [16] C. Bown *et al.*, Nucl. Inst. Meth. **A369**, 248(1996).
- [17] A. R. Barker, "Trigger TDC/Hit-Counting Design Report", KTeV Internal Note 204(1994).
- [18] V. O'Dell and T. Yamanaka, "The KTeV Data Acquisition System V1.0", KTeV Internal Note 184(1994).
- [19] T. Nakaya and V. O'Dell and T. Yamanaka and M. Hazumi, Proceedings of CHEP95(1995).
- [20] H. Chew, Phys. Rev. **123**, 377(1961).

